2007

# First-principles studies of boron nanostructures

Kah Chun Lau
*Michigan Technological University*

### Recommended Citation

# *FIRST-PRINCIPLES* STUDIES OF BORON NANOSTRUCTURES

By

KAH CHUN LAU

A DISSERTATION

Submitted in partial fulfillment of the requirements

for the degree of

DOCTOR OF PHILOSOPHY

(Physics)

MICHIGAN TECHNOLOGICAL UNIVERSITY

2007

This dissertation, "*First-Principles* Studies of Boron Nanostructures", is hereby approved in partial fulfillment of the requirements for the degree of DOCTOR OF PHILOSOPHY in the field of Physics.

DEPARTMENT or PROGRAM:
Physics

Signatures:

Dissertation Advisor    _____

Dr. R. Pandey

Committee    _____

Dr. D. Beck

_____

Dr. Y.K. Yap

_____

Dr. R. Brown

Department Chair    _____

Dr. R. Pandey

Date    _____

# Acknowledgments

In my opinion, my PhD life consists of two parts. The first part is about science, and it will be covered by the most of the writings in this dissertation. The second part is about part of my life in Michigan Tech, which I will touch a little bit via acknowledgements in this dissertation.

This thesis would not have been possible without the help and support of numerous people. First, I would like to express my sincere thanks to Prof. Ravindra Pandey, my thesis advisor. Thank you for your great patience, support and inspiring guidance on both, work and life. Thank you for the freedom, opportunities and help given to me in the last few years to explore on the thesis problem. I believe we both did a pretty good job on these problems in the last three years, although we stumbled into this field (i.e. boron nanostructures) a little bit too late!

Similarly I should thank Prof. Donald R. Beck, Prof. Yoke Khin Yap and Prof. Richard E. Brown as my advisory committee members. Thank you for the time and effort for being considerate on this dissertation, and the valuable comments and suggestions to make this dissertation better.

I am grateful and indebted to Prof. Roberto Orlando for being a very wonderful collaborator, and a good teacher at the same time to assist me in exploring some related problems beyond this dissertation. A special note of thanks to Prof. Ranjit Pati for introducing us on electron transport in nanostructures. Besides, I should also thank Prof. Dilip Kanhere, Prof. Miguel Blanco, Dr. Mrinalini Despande, Dr.

Aurora Costales, Dr. Anil Kandalam and Dr. Huitian Jiang, who have been working with me, and taught me during the early phases of my PhD. study. Thanks for giving me much help since then.

I would also like to thank my colleagues in our current research group members: Dr. Ralph Scheicher, S. Gowtham and Haiying He for always working with me. Thank you Gowtham for always helping me, and being a good 'guru' in computers. Thank you, Ralph and Haiying for being always quick responsive, whenever I need your help and for the valuable suggestion. Besides, a special thanks to Lin Pan, for providing help on the calculations on Dirac-Fock and RCI on boron atom, and being a good office-mate, as well as coursemate during our graduate course study. Then, I would like to thank all the professors, staff and my friends from physics and other departments at Michigan Tech in the last four years.

On the personal front, I specifically dedicate this work to my beloved grandma, who passed away during the second year of my PhD study. You taught me that always be humble, optimistic, patient and persistent during up and down in my life. On the other hand, without the love and unconditional support of my family, this long journey through the graduate school would never have begun, much less completed. Therefore, I am really indebted to my dearest Mom, Dad, and my sisters, for being always with me and provided me a warm home when I just wanted to get away. Last, but certainly not the least, Xiaoqi. She has always been there for me: listening to my frustrations during the days when preparing the dissertition, putting up with me when I worked till midnight during weekends, and not complaining. Therefore, I

would not be where I am, nor who I am, without them.

# Dedication

To My Beloved Grandma

# Contents

# List of Figures

# List of Tables

# Abstract

Boron is an 'electron deficient' element which has a rather fascinating chemical versatility. In the solid state, the elemental boron has neither a pure covalent nor a pure metallic character. As a result, its vast structural dimensionality and peculiar bonding features hold a unique place among other elements in the periodic table. In order to understand and properly describe these unusual bonding features, a detailed and systematic theoretical study is needed. In this work, I will show that some of the qualitative features of boron nanostructures, including clusters, sheets and nanotubes can easily be extracted from the results of *first principles* calculations based on density functional theory. Specifically, the size-dependent evolution of topological structures and bonding characteristics of boron clusters, $B_n$ will be discussed. Based on the scenario observed in the boron clusters, the unique properties of boron sheets and boron nanotubes will be described. Moreover, the ballistic electron transport in single-walled boron nanotube relative to that of single-walled carbon nanotubes will be considered. It is expected that the theoretical results obtained in the present thesis will initiate further studies on boron nanostructures, which will be helpful in understanding, designing and realizing boron-based nanoscale devices.

# Chapter 1

# Introduction

## 1.1 Nanostructures: Fundamental Perspectives

From my personal perspectives, there is one thing we can say about the $N$-body problem in the nanoscopic world:

*"More is Different, and Small is Weird"*!

The *first term* refers to particle correlation, the *second term* refers to the intrinsic scale of the physical size of the system.

Nanotechnology allows scientists to manipulate individual atoms, molecules and nanostructures, making it possible to build machines smaller than the size of human cells with dimensions of the order of a few nanometers. It is a field that holds much promise for treating disease, building smaller electronic devices, and creating efficient alterna-

tive energy devices, among other things[1]. Nanosystems are functional systems that make atomically precise structures, components, and devices under a programmable control. At present, there is, however, a huge gap between the basic nanostructured materials being manufactured and the potential of productive nanosystem as we envisioned. As a result, manufacturing of nanosystem poses great challenges, the biggest being size of the system. Objects this small don't always behave the way the standard macroscopic laws of physics predict. Therefore, the quest to discover, understand and control how materials behave properly on the nanoscale is currently a challenge to scientists.

Within this context, nanostructured materials are usually defined as a system made out of atoms in their common forms, with the atoms are arranged in nanometer or sub-nanometer size units. These units can be consisted of a few to thousands of atoms, and may extend to the larger microscopic size before approaching the bulk matter[2]. These tiny grains, atomic aggregates or clusters, in which the surface plays a paramount role, respond to external stimuli such as light, mechanical stress, and electromagnetic fields quite differently from the bulk matter. In many instances, at sufficiently small sizes (usually in nanoscopic regime), dependence of the material property on the system size becomes non-scalable. Thus, small is different in an essential way, that is, the exhibited behavior is characteristic of the assembly of particles rather than being a property of the individual constituents[2, 3]. Hence, identification and understanding of these series of microscopic origins and phenomena associated with nanostructures, are of fundamentally importance.

We now would like to highlight some recent developments in the areas pertaining to physical and chemical properties of a system, namely boron nanostructures. This thesis is not intended as a general review. Instead, it is more like a 'brief' summary based on my experience on the subject which I gained at Michigan Technological University[4, 5, 6, 7, 8, 9, 10, 11, 12, 13]. Thus, I will use some examples based on some of my work as illustrations. In summary, the properties of the boron nanostructures considered are predicted by the computational model. Of course, the ultimate confirmation of these theoretical syudies is still to be determined by future empirical evidences.

## 1.2   Overview

" There is plenty of room at the bottom in *boron research*. "

Boron nanostructures have attracted the attention due to the remarkable properties of the elemental boron which is defined as 'electron-deficient' [14, 15] (i.e. the number of available valence electrons, $2s^2 2p^1$ is less than the available orbitals in the electronic configuration of atomic valence shell). The consequences for the nature of the chemical bonds of electron-deficient materials are well-known, and they may be summarized as follows[16]. First, the ligancy of electron-deficient materials is higher than the number of valence atoms, and even higher than the number of stable valence orbitals. Second, electron-deficient materials cause adjacent atoms to increase their ligancy to the values larger than the orbital numbers[16, 17]. In general, the 'electron deficient'

nature does not suggest that it is inferior in bonding, but simply that novel structures based on the elemental boron are expected to be adopted in nature. With insufficient electrons to support a structure by conventional '2-electron two-center' bonds, the boron-based compounds generally tend to adopt a novel mechanism to resolve its 'electron-deficiency' through '2-electron multi-center' bonds topologically connected in a complex networks [14, 15].

On the other hand, boron and carbon differ dramatically in many aspects, though they are neighbors in the periodic table. Studies about the analogies between boron and carbon can be very interesting. Nevertheless, many similarities exist between the chemistry of boron and carbon, and this account adds novel relationships among these neighboring elements[18, 19, 20, 21, 22, 23, 24]. In this aspect, carbon is a key player in much of the current novel materials research, namely fullerenes[25], and nanotubes[26]. Yet the bonding in carbon is elegantly simple. In contrast, the structure and bonding of boron alltropes present extreme complexity. The electronic structure and relative stability that stems from it remain to be fully understood.

There are reports of numerous alltropes of boron, only few of them are comparatively well-characterized[14, 15, 27]. Under ambient pressure, solid boron exists in various complex crystalline structures, which utilize the icosahedral $B_{12}$ cluster as a common structural component. The $B_{12}$ icosahedrons can be interlinked by strong covelent bonds in variety ways to form several well-known polymorphs such as: $\alpha$-rhombohedral $B_{12}$ ($\alpha$-$B_{12}$)[28, 29, 30, 31, 32, 33, 34, 35, 36], $\alpha$-tetragonal $B_{50}$ ($T$-$B_{50}$)[30], or $\beta$-rhombohedral $B_{105}$ ($\beta$-$B_{105}$)[28, 33, 35, 36, 37, 38]. Moreover, the

striking findings on nonmetal-metal[33, 34] and nonmetal-superconductor[39, 40, 41] transition were made and proposed. Within this context, the ground state modification in high-pressure phase of boron is yet unknown. On the other hand, so far there is no definite experimental evidence for the phase transition between the $\alpha$ and $\beta$ phases. In contrast to carbon alltropes, the phase diagram of boron alltropes so far is not well-established.

Similar to its complex bulk polymorphs, a large diversity of studies on the topological configurations of boron nanostructures, especially boranes[18, 19, 22, 23, 24], the hydrocarbon equivalents, continue to emerge. Consequently together with the discovery of 'magic numbers' in metallic clusters[42, 43], carbon fullerenes and nanotubes[25, 26, 44], a series of synthesis and characterization studies of boron clusters[45, 46, 47, 48, 49, 50, 51, 52, 53], nanowires, nanoribbons, nanowhiskers, and nanotubes[54, 55, 56] have been performed. However relative to carbon nanostructures, studies in the boron nanostructures are few and lag far behind. Furthermore, the reported studies in boron nanostructures are mostly related to small sized boron clusters, while the studies in other nanostructures, nanowires, nanoribbons, nanowhiskers, and nanotubes, remain at the infant stage. The growth mechanism and actual structural morphology of boron nanotubes are still unknown[56]. Overall, both experimental and theoretical works suggest that the existence of boron nanotubes and clusters are closely related[5, 6, 53, 57], and can be categorized as a new class of topological structure in boron[10], in contrast to boron nanowires and nanoribbons which are more closely related to the boron bulk solids[6, 10, 17]. In summary,

many subtle unsolved questions and problems remain to be addressed regarding the physics and chemistry of the boron nanostructures. Therefore, we believe, that there is an acute need for a more systematic studies on various possible phases of elemental boron within a different structural motif, based on the state-of-the-art computational tool, e.g. simulations based on *first principles* method.

# Chapter 2

# Methodology

## 2.1 Theoretical Foundation

"Quantum mechanics is a set of laws of physics which, to the best of our knowledge, provides a '*complete*' account of the microworld from the available physical theories todates. However, solving a quantum mechanical many-body problem is *never* an easy task ! "

Quantum mechanics is at the core of our present understanding of the laws of physics, besides the theory of relativity. It is the most fundamental physical theory, and it is inherently probabilistic. This means that all predictions derived from quantum mechanics are of a probabilistic character and that there is, as far as we know, no underlying classical deterministic theory from which the quantum probabilisties could be deduced. Thus, the statistical interpretation of quantum mechanics ultimately

implies that predictions are being made about the behavior of ensembles, i.e. about collections of a large number of independent, individual systems, and that the statements of quantum theory are tested by carrying out measurements on large samples of such systems. Therefore, quantum mechanical systems must be regarded as open systems[58]. On the one hand, any realistic system, like in classical physics is subjected to a coupling to an uncontrollable environment which influences it in a non-negligible way. In order to effect the occurence of chance events a quantum system must be subjected to interactions with its surroundings. Any empirical test of the statistical predictions on a quantum system requires one to couple it to a measuring apparatus which generally leads to non-negligible influences on the quantum objects being mesured. Thus quantum mechanics in itself involves an intimate relationship to the notion of an open system through the action of the measurement process.

As a consequence of this inherent probabilistic nature, the limits of applicability and even the interpretation of the predictions of modern quantum theory are lively areas of debate amongst phyicists and philosophers[59]. Questions such as "How do we interpret the probabilistic nature of wave functions?", "What constitutes a measurement?", "How much can we ever know about the state of a system?", and "Can quantum mechanics describe consciousness?" are fundamentally important for our understanding of the physical laws of nature. Despite the fact that these problems are still controversial, it is clear that whether or not a more complete description of the world is possible, the accuracy of the predictions made based on modern quantum theory is incredible. So far, in every instance of its application to date, the equations

of quantum mechanics have yet to be shown to fail. Therefore, we have every reason to assume that an understanding of all physical phenomenon in nature can be achieved by continuing to solve these equations.

As far as we know, nearly all physical properties of a physical system are related to the total energies or to the differences between total energies. With this regard, the quantum mechanical rules, or Hamiltonians, for calculating the total energy of a 'simple' one-atom systems have provided some of the most precise tests of the theory. It is therefore eminently reasonable to assume quantum mechanics to predict accurately the total energies of aggregates of atoms as well. So far, this assumption has been confirmed many time by experiments. To put this argument in a historical perspective, let us recall here a famous statement made by P.M. Dirac in 1929 shortly after the introduction of the Schrödinger equation and it's successful validation for simple systems like $H_2$ and $He$: "*The fundamental laws necessary for the mathematical treatment of a large part of physics and the whole of chemistry are thus completely known, and the difficulty lies only in the fact that application of these laws leads to equations that are too complex to be solved*". This was a cry both of triumph and of despair. It marked the end of the process of fundamental discovery in quantum chemistry, but left a collossal mathematical task of implementation. In retrospect, the implied finality of the claim seems excessively bold[60]. There is no doubt, the main expectation made by this famous statement is still valid today. Though the grand vision is already been there since decades ago, but the similar grand challenges remain to date. However, the good news is that the ultimate search and confirmation

for this elegant expectation is no longer a mere idle philosophical musing, but rather a practical methodology in symbiosis with the rapid advances in computers.

One of the accurate yet practical methodology we mentioned here, is usually referred to as *first principles* study (or an *ab initio* study). The term *ab initio* (Latin for "from the begining") means from first principles, in which all the physical properties we studied on a system can be calculated using nothing but the nonrelativistic Schrödinger equation (Eq. 2.1) , the values of the fundamental constants and the specification of atomic numbers of the atoms present in the system[61].

$$\hat{H}\Psi \ = \ i\hbar\frac{\partial\Psi}{\partial t} \tag{2.1}$$

However, this does not mean that we are solving the Schrödinger equation exactly, where the $\Psi$ is the many-body wave function (or state function). Instead, it simply means that we are selecting this as a method that in principle can lead to a reasonable approximation to the solution of the Schrödinger equation with appropriate approximations implemented within this method.

## 2.2 Approximations

Before continuing into the details from different well-established methodologies, a little more must be said about Eq. 2.1 and the relation of its solutions (Eq. 2.1 and 2.2) to the *experimentally observed* physical properties. First, any experimental

observation is performed not on a single molecule but on a macroscopic aggregate of molecules (i.e. a nanoscopic system). Second, any observation involves some kind of interaction with the system. Very often it can be assumed that the environment of an aggregate of molecules has little effect on some given physical property of interest. In the conventional spectroscopy, the radiation field merely provides a weak perturbation, inducing transitions from one state to another, and properties of the individual molecular states usually can be accurately inferred from the available stationary states of a system.

$$\hat{H}\Psi \;=\; E\Psi \tag{2.2}$$

Therefore, we usually take no account of these facts when setting up the Schrödinger equation or its corresponding hamiltonian as shown in Eq. 2.1. Instead, commonly a time-independent Schrödinger equation (Eq. 2.2) will be used as a basis for the study of physical properties of a system in stationary states, with the corresponding Hamiltonian, $\hat{H}$ (Eq. 2.3) given below.

$$\hat{H} \;=\; \sum_{i=1}^{N}\left(\frac{-\nabla_i^2}{2}\right) + \sum_{\alpha=1}^{M}\left(\frac{-\nabla_\alpha^2}{2M_\alpha}\right) - \sum_{i=1}^{N}\sum_{\alpha=1}^{M}\left(\frac{Z_\alpha}{r_{i\alpha}}\right) + \frac{1}{2}\sum_{i\neq j}^{N}\frac{1}{r_{ij}} + \sum_{\alpha<\beta}^{M}\frac{Z_\alpha Z_\beta}{R_{\alpha\beta}} \tag{2.3}$$

where $M_\alpha$ is the ratio of the mass of nucleus $\alpha$ to the mass of an electron, and $\hat{H} = \hat{H}_e$ + $\hat{H}_n$ + $\hat{H}_{en}$ is the sum of the electronic, nuclear, and interaction (electron-nuclear)

term respectively. To make all the equations look simpler, atomic units (in which all electromagnetic equations are written in cgs form, and the fundamental constants $\bar{h}$, $e^2$, $4\pi\varepsilon_0$ and $m_e$ are set to unity) have been used throughout this thesis.

We shall now deal almost exclusively with stationary states, without considering the effects of time-dependent perturbations in a system. Whereas in conventional chemical reactions, however, more drastic changes occur as a result of ionization, collision and scattering processes within particular physical phases (i.e. gas, liquid, solid or mixed phases) is involved. Therefore even at the molecular level, such processes are time-dependent, and their analysis requires solving the time-dependent Schrödinger equation (Eq. 2.1).

Returning to the time-independent Schrödinger equation (Eq. 2.2), it must be stressed that the Hamiltonian in Eq. 2.3 is still somewhat idealized, even for an isolated system. In this case, we have assumed that the interactions among the nuclei and electrons as regular classical electrostatic Coulombic interactions. Therefore the more general electromagnetic interactions and spin-orbit couplings are ignored in this case study as an approximation[62].

## 2.2.1 Born-Oppenheimer Approximation

Strictly speaking, a complete description of a system requires solving the full time-independent Schrödinger equation (Eq. 2.2 and 2.3) including both electronic and nuclear degrees of freedom, is a formidable computational task which is in fact al-

together unfeasible at present, especially for systems consisting of an aggregates of atoms and more than one electronic state[63]. In fact, there are several features that contribute to this difficulty. First, this is a multicomponent many-body system, where each component (i.e. each nuclear species and electrons) obey a particular statistics. Moreover, the complete wave function cannot be easily factorized because of Coulombic correlations. In other words, the full Schrödinger equation cannot be easily decoupled into a set of equations such that, in general, we have to deal with $(3M+3N)$ coupled degrees of freedom. Therefore in order to study the dynamics and ground state of the vast majority of chemical systems, several further approximations, have to be imposed.

Due to the large differences in mass between the electrons and nuclei, and the fact that the forces on the interacting particles are the same, the electron cloud can be assumed to respond essentially instantaneously to the motion of the nuclei or the changes in the nuclear configuration. This approximation ignores the possibility of having non-radiative transitions between different electronic eigenstates. Hence within this approximation, the nuclear dynamics has no means to cause electronic transitions, and electrons remain always in the same adiabatic state (i.e. ground or excited state). In this case, we define the dynamics to be '*adiabatic*'. Therefore by assuming the electron-nuclei coupling to be purely classical electrostatic in origin and their motion can be treated independently, which will eventually lead to a separation of electronic and nuclear coordinates (i.e. decoupling of the nuclear and electronic degrees of freedom) in the many-body wave function, within the so-called *Born-Oppenheimer*

*Approximation or adiabatic approximation* (Eq. 2.4).

$$\Psi(r, R) = \Psi^{ele}(r, R)\Phi(R) \tag{2.4}$$

where the function $\Psi^{ele}$(r,R) is the electronic wave-function, and the function $\Phi$(R) is the nuclear wave-function. Based on this approximation, we can assume that the term $\frac{-\nabla_\alpha^2}{2M_\alpha}\Psi^{ele}(r, R)$ from Eq. 2.3 is negligible. As a result, the main task of the electronic structure calculations is now reduced to solving the electronic Schrödinger equation, with electrons under the external electrostatic field of fixed nuclei written as:

$$H^{ele}\Psi(r, R) = E^{ele}\Psi^{ele}(r, R) \tag{2.5}$$

where $H^{ele} = \sum_{i=1}^{N}\left(\frac{-\nabla_i^2}{2}\right) - \sum_{i=1}^{N}\sum_{\alpha=1}^{M}\left(\frac{Z_\alpha}{r_{i\alpha}}\right) + \frac{1}{2}\sum_{i\neq j}^{N}\frac{1}{r_{ij}}$. Furthermore, by excluding the consideration of simulating the quantum molecular-dynamics[61] of this system by assuming a strict zero temperature treatment, i.e. no zero-point motion of the nuclei is included, the remaining kinetic energy of nuclei: $\frac{-\nabla_\alpha^2}{2M_\alpha}$ appearing in Eq. 2.3 can be completely omitted.

As a result, this "adiabatic principle" reduces the many-body problem to the solution of the dynamics the electrons in the frozen-in configuration of the nuclei (as a collection of classical particles[64]) with the total energy of the system finally simplified as

follows:

$$E = E^{ele} + \sum_{\alpha < \beta}^{M} \frac{Z_\alpha Z_\beta}{R_{\alpha\beta}} \qquad (2.6)$$

The *Born-Oppenheimer Approximation* is used to vary adiabatically the positions of the nuclei, letting the electrons adjust their motion at any time to the instantaneous external field of the nuclei, until the total static energy is minimized. As a consequence, nuclear motion evolves on a *single* potential energy surface (PES), associated with a *single* electronic quantum state, which is obtained by solving the time-independent Schrödinger equation for a series of fixed nuclear geometries.

As a result, a ground state configuration with lowest total energy of one system can be obtained through structural optimization when the forces on the $\alpha$-th nucleus from the $k$-component:

$$\vec{F}_{\alpha,k} = -\vec{\nabla}_{\alpha,R_k} E \qquad (2.7)$$

(i.e. with $E$ defined as Eq. 2.6) vanish, with the aid of *Hellmann-Feynman Theorem*[61, 65, 66]. However, even with this important simplication, the many-body problem of interacting electrons within one system remains formidable. Further appropriate simplications are necessary in order to allow full quantum mechanical total energy calculations to be preformed accurately and efficiently.

## 2.2.2 Many Electron Systems

In short, the essence and the greatest challenge of many-body problem of interacting electrons within one system is presented by the underlying electron correlation[61, 62, 65, 67]. Due to this main challenge, tremendous progress has been made in condensed matter physics and quantum chemistry, especially in the field of electronic structure studies. The underlying theoretical approximations are solely determined by the degree of electronic correlation (i.e. weakly correlated *Vs.* strongly correlated electrons) within a system. For the electrons in the weak coupling regime, the kinetic energy rules the physics and the system remains qualitatively similar to a noninteracting electron gas. For the strong coupling regime, the potential energy dominates, and the electrons display the collective behavior characteristic in the system[67, 68, 69].

As a critical step towards the understanding of weakly correlated electrons in a system, the realization of the nature of 'independent' non-interacting electrons in solids within the band theory, is a hallmark scientific achievement. Within this regime, electrons can be described as correlated with one another through the *Pauli Exclusion Principle*, and interacting only via the effects of some average potential. However, for quantitatively more accurate descriptions, one must go beyond the simple effective independent-electron approximations due to substantial correlations in localized systems and characteristic chemical bonds[67, 69].

Compared to weak coupling regime dominant in chemistry, the studies in condensed matter physics are more frequently associated with strong correlated system, such as

Mott metal-insulator transitions[70, 71, 72], superconductivity[73], Wigner crystals[74], quantum Hall liquid[68], etc. In general, these physical pheneomena are distinct from the Pauli repulsion which dominates ordinary matter within an independent-electron picture, but rather manifested as a collective behavior that emerges in long-range order, as the consequences of many-body electron-electron interactions[75].

However in this thesis, most of the systems and their physical properties fall into the weakly correlated system. Therefore the remainder of this chapter is devoted to the theoretical basis and its formalism on ground state studies on electronic structure of boron nanostructures. Therefore, the major portion of the discussion will be based on independent-particle approaches that are largely based upon the current well-established *first-principles* study, which is the theoretical basis for approximate inclusion of many-body effects in the mean-field independent-particle methods.

### 2.2.2.1 The Independent-Electron Approximation

Currently, the field of electronic structure is at a momentous stage, with rapid advances in basic theory, new algorithms, and computational methods. Therefore, an exhaustive overview which incorporates detailed discussion of all the theoretical methods available in current scientific community is never an easy task. In a broad definition, there are two basic independent-particle approaches that may be classified as "non-interacting" and "Hartree-Fock". They are similar in that each assumes the electrons are uncorrelated except that they must obey the *Pauli exclusion principle*. However, they are different in that Hartree-Fock includes the electron-electron

Coulomb interaction in the energy, while neglecting the correlation that is introduced in the true wave-function due to those interactions. This approach is often referred to as "Hartree" or "Hartree-like", after D.R. Hartree[76] who included an average Coulomb interaction in a rather heuristic way. In general, "non-interacting" theories have some effective potential that incorporates some effect of the real interaction, but there is no interaction term explicitly included in the Hamiltonian. More to the point of modern electronic structure calculations, all calculations following the Kohn-Sham method (DFT) involve a non-interacting hamiltonian with an effective potential chosen to incorporate exchange and correlation effects approximately.

### 2.2.2.2   Hartree-Fock Theory

In the preceding section, it was mentioned that under the weakly coupling regime in electron correlation of a system, the observables of the many-body (i.e. many-electron) problem can be mapped into equivalent observables in a single-particle (i.e. one-electron picture) problem under an effective 'mean-field' theory. Among the mean-field theories which are used to solve the many-electron system, the most popular initial attempts to solve Eq. 2.5 is based on *Hartree-Fock Theory* within the independent electron approximation within a self-consistent field[76, 77, 78]. As a result, the assumption of independently moving electrons implies that the total wave-function of the $N$-electron system, $\Psi(r, R) \rightarrow \Psi(r)$ (i.e. we will omit explicitly writing the parametric dependence of wave-function on the nuclei coordinates for simplicity) can be approximated as an antisymmetrized product of $N$ orthonormal

single-electron wave-function, $\psi_i(x_i)$ in a single Slater determinant:

$$\Psi_{HF}(x_i) = \frac{1}{\sqrt{N!}} \begin{vmatrix} \psi_1(x_1) & \psi_2(x_1) & ... & \psi_N(x_1) \\ \psi_1(x_2) & \psi_2(x_2) & ... & \psi_N(x_2) \\ ... & ... & ... \\ \psi_1(x_N) & \psi_2(x_N) & ... & \psi_N(x_N) \end{vmatrix} \qquad (2.8)$$

where each $\psi_i(x_i)$ is a product of a spatial orbital $\phi_k(r)$ and a spin function $\sigma(s) = \alpha(s)$ or $\beta(s)$.

In brief, the *Hartree-Fock (HF) approximation*[79] is the method whereby the orthonormal orbitals $\psi_i$ are found that minimize $E^{ele}[\Psi]$ for this determinantal form of $\Psi$.[65] The energy of a state of many electrons in the Hartree-Fock approximation,

$$< \Psi_{HF}|\hat{H}|\Psi_{HF} > = \sum_{i=1}^{N} < \psi_i|\hat{h_1}|\psi_i > + \frac{1}{2} \sum_{i,j=1}^{N} [< \psi_i\psi_j|\hat{h_2}|\psi_i\psi_j > - < \psi_j\psi_i|\hat{h_2}|\psi_i\psi_j >]$$

$$(2.9)$$

with $\hat{h_1} = -\frac{1}{2}\nabla^2 + V_{ext}(r)$ and $\hat{h_2} = \frac{1}{|r-r'|}$, is the best possible wavefunction made from a single determinant (or a sum of a few determinants in a multi-reference Hartree-Fock function needed for degenerate cases)[80].

Improvement of the wavefunction to include electron correlation introduces extra degrees of freedom in the wavefunction and therefore always lowers the energy for any state, ground or excited, by a theorem attributed to MacDonald[81]. The low-

ering of the energy is termed the "correlation energy", $E_c$. However, this is definitely not the only possible definition of $E_c$. Indeed, it could also be defined as the difference between the exact energy from some other reference calculation which is beyond Hartree-Fock[80]. But in general, the Hartree-Fock method always leads to the smallest possible value of $E_c$, among the others. As a matter of fact, the HF approximation doesn't take into account the short-range (dynamical) correlation between the electrons. This is due to the fact that by assuming each electron moves in each orbital independently, the wave-function $\Psi$ is represented by a single Slater determinant, in which the electrons only interact with an average effective potential due to the existence of other electrons, instead of the actual pairwise interactions. So in order to include the dynamical correlation term beyond Hartree-Fock, the many-body wave-function can be represented by a linear combination of Slater determinants[62, 67, 80]. Here, the Configuration Interaction (CI) method, the multi-configuration SCF method (MC-SCF), and the Coupled-cluster method[66, 80] are well-known by including these multi-determinantal wave-functions. However, due to the large number of the configurations, it becomes computationally very expensive to employ this post-Hartree-Fock method to large many electron systems. Thus in order to overcome this difficulty, with the balance of computational cost and accuracy, several promising approximations have been developed, and one of them is *Density Functional Theory* (DFT), the main theoretical formalism used in this thesis.

### 2.2.2.3 Density Functional Theory

**Thomas-Fermi Model**

As we know, the many-electron wavefunction $\Psi$ contains a great deal of information: all we could ever have, but more than we usually want. For the practical point of views, often what we want is no more than the total energy, $E$ (and its changes), or perhaps also electron density distribution for the ground state of a system. However, in the view of the difficulties in solving quantum many-body problems as mentioned in the previous section, the notion that ground state properties of quantum many-particle systems can solely be characterized in terms of the '*simple*' one-particle density, $\rho(r)$ is not so obvious.

Instead of thinking of the solution of the complicated $N$-electron wave-function, $\Psi(r_1, r_2, ..., r_n)$, a drastically simpler idea based on statistical considerations to approximate the distribution of electrons in a system, can help us to derive the equivalent solution of Eq. 2.4 in a remarkable way. The underlying ingenious idea and assumption can be traced back to 1927 from Thomas and Fermi (i.e. the *Thomas-Fermi model*), soon after the birth of modern quantum theory[82, 83, 84, 85]. Therefore, this begins to expound a series of related theoretical models that allows one to replace the complicated $N$-electron wave function: $\Psi(r_1, r_2, ...., r_N)$ and the associated Schrödinger equation by the much simpler electron density, $\rho(r)$ and its calculation scheme[85, 86].

Assuming that for the ground state of the system of interest, the electron density

$\rho(r)$ is a solution of the stationary (i.e. variational) principle by minimizing the energy functional $E_{TF}[\rho(r)]$: $\delta\{E_{TF}[\rho] - \mu_{TF}(\int \rho(r)dr - N)\} = 0$, where $\mu_{TF}$ is a Lagrange multiplier under the constraint $N = N[\rho(r)] = \int \rho(r)dr$, where $N$ is the total number of electrons in the system. By taking into consideration the pure electrostatic interaction of electron-nucleus attraction, and electron-electron repulsion, an energy functional for a system in terms of electron density alone can be defined as:

$$E_{TF}[\rho(r)] \;=\; T[\rho(r)] + \int \rho(r)\nu(r)dr + V_{ee}[\rho(r)] \qquad (2.10)$$

where $T[\rho(r)]$ is the kinetic energy, $\nu(r)$ is electron-nucleus interaction energy, and $V_{ee}[\rho(r)] = J[\rho]$ - $K[\rho]$ is the electron-electron interaction energy which includes the exchange-energy formula, $K[\rho]$ first proposed by Dirac[85]. Based on the homogeneous free electron gas[87, 88], the kinetic energy term of these non-correlated electrons can be derived as: $T_{TF}[\rho] = C_F \int \rho^{\frac{5}{3}}(r)dr$, with $C_F = \frac{3}{10}(3\pi^2)^{\frac{2}{3}} = 2.8712$, which is known as *Thomas-Fermi kinetic energy formula*. Consequently, the exchange energy can be obtained similarly, as: $K_D[\rho] = $ -$C_X \int \rho^{\frac{4}{3}}(r)dr$, with $C_X = \frac{3}{4}(\frac{3}{\pi})^{\frac{1}{3}} = 0.7386$, which known as *Dirac exchange-energy formula*. By inserting the term: $T_{TF}[\rho]$ and $K_D[\rho]$ into Eq. 2.9, we obtain the *Thomas-Fermi-Dirac energy functional*, $E_{TFD}[\rho]$ accordingly defined as follows:

$$E_{TFD}[\rho(r)] \;=\; C_F \int \rho^{\frac{5}{3}}(r)dr + \int \rho(r)\nu(r)dr + J[\rho(r)] - C_X \int \rho^{\frac{4}{3}}(r)dr \qquad (2.11)$$

Based on this approach, several modifications and improvements of the Thomas-Fermi theory have been made over the years. Unfortunately, this elegant yet primitive model is not accurate in making much significant quantitative predictions and improvements in atomic, molecular or solid state physics calculations[86, 89, 90]. However, this situation changed with the publiction of the landmark paper on *Density Functional Theory (DFT)* by Hohenberg and Kohn[91] in 1964, which provides the fundamental theorems showing that for ground states the Thomas-Fermi model may be regarded as an approximation to an exact theory. As a matter of fact, DFT constitutes a method in which, without loss of rigor, one works with the electron density, $\rho(r)$ as the basic variable, instead of the wave function $\Psi$. Thus, the simplification is immense. The restriction to ground states is what makes density functional theory possible, with the minimum energy principle for ground states playing a vital role. This is reminiscent of thermodynamics, which is largely a theory of equilirium states. The Hohenberg-Kohn theorems provide a formalistic proof for the correctness of Thomas-Fermi model, but do not provide any practical schemes for calculating ground state properties from the electron density. This was on the other hand, provided by the approach later proposed by Kohn and Sham[92] (1965). Henceforth, DFT offers a practical computational scheme: the Kohn-Sham equations, which are similar to Hartree-Fock equations, yet they include both exchange and correlation effects in principle.

**Theorems**

In brief, there are two essential statements on which DFT is based:

† Every observable in a quantum system can be calculated from the electron density of the system alone.

† The density of the interacting system can be approximated by the density of an auxiliary system of noninteracting particles which do not interact with each other, and just move in an effective external field.

These two statements are known as *Hohenberg-Kohn* and *Kohn-Sham* theorems.

**Hohenberg-Kohn Theorem**

As a matter of fact, the original proof and derivation of Hohenberg-Kohn theorem was based upon "reductio as absurdum"[65, 91], and later refined and extended for degenerate ground states under the "constrained search" formulation under the Levy-Lieb formulation[93, 94, 95, 96]. To be more specific, the theorem can be divided into two parts:

† $1^{st}$ Theorem: The external potential is uniquely determined by the electronic density, except for a trivial additive constant.

Corollary: Since $\rho(r)$ uniquely determines $V(r)$, then it also determines the ground state wave function, $\Psi_{GS}$.

† $2^{nd}$ Theorem: For any trial density, $\rho'(r)$, such that $\rho'(r) \geq 0$ and $\int \rho'(r)dr = N$

(i.e. $\rho'(r)$ be a non-negative density normalized to $N$). Then with the variational

principle, $E_{ground} \leq E_V[\rho'(r)]$, for

$$E_V[\rho'] = T[\rho'] + U[\rho'] + \int \rho'(r)V(r)dr \qquad (2.12)$$

with $U[\rho'] = \frac{1}{2} \int \int \frac{\rho'(r)\rho'(r')}{|r-r'|} dr dr' + E_x[\rho'] + E_c[\rho']$.

Here, the implications of the Hohenberg-Kohn theorem can be summarized in the

following three points:

† There is a one-to-one correspondence between the external one-particle potential

$V(r)$ and the ground state density of the system, $\rho(r)$:

$$V(r) \longleftrightarrow \rho(r) \qquad (2.13)$$

This tells us that if we know $\rho(r)$ we can determine uniquely the potential $V(r)$

which can be viewed as a functional of density $V = V[\rho(r)]$. Then, we can solve

the Schrödinger equation (Eq. 2.2) with this effective potential. Therefore, all

the eigenstates, and the corresponding energies (eignevalues) of the system are

then determined by this ground state density, $\rho(r)$ of the system.

† There is a variational principle $E_{ground} \leq E_V[\rho'(r)]$ that requires that the ground

state density satisfy the stationary principle:

$\frac{\delta E_{HK}}{\delta \rho(r)} = 0$ for $\rho(r) = \rho_{exact}(r)$ such that:

$$\delta\{E_V[\rho] - \mu[\int \rho(r)dr - N]\} = 0 \qquad (2.14)$$

which gives the Euler-Lagrange equation:

$$\mu = \frac{\delta E_V[\rho]}{\delta \rho(r)} = V_{ext}(r) + \frac{\delta F_{HK}[\rho]}{\delta \rho(r)} \qquad (2.15)$$

with the quantity $\mu$ is the chemical potential of the system[65]. It states that

the total energy, $E_{HK}$ as a functional of the electron density, $E_V[\rho]$, and it has

its minimum at the exact ground state density $\rho_{exact}(r)$.

† The last point of the *Hohenberg-Kohn* theorem provides a way to express this

functional. It can be written as:

$$E_{HK}[\rho] = F_{HK}[\rho] + \int \rho(r)V_{ext}(r)dr \qquad (2.16)$$

which the $F_{HK}[\rho]$ is a universal functional of $\rho(r)$, independent of the external

potential $V_{ext}(r)$. Once we have an explicit form (approximate or accurate) for $F_{HK}[\rho]$, we can apply this method to any system, with the Eq. 2.14 as the basic working equation of DFT.

## 2.3 A Generic Kohn-Sham Approach

One particular way of exploiting the *Hohenberg-Kohn* theorem is the well-known *Kohn-Sham* scheme[92], which expresses the ground state density of the interacting particles of a material in terms of the orbitals of auxiliary non-interacting particles moving in an effective external local potential, $V_{ext}$. Here, the outline of this section is to give a brief technical overview on how to solve the Kohn-Sham equations (i.e. the main theoretical scheme used in this thesis) as mentioned in the previous section. In spite of their differences among the conventional DFT codes available, all codes are designed to try to solve the Kohn-Sham equations:

$$-\frac{\nabla^2}{2} + \nu_{KS}[\rho(r)]\varphi_i(r) = \varepsilon_i\varphi_i(r), \tag{2.17}$$

as shown in the simple flow-chart of Fig. 2.1 which this notation, $\nu_{KS}[n(r)]$ is the Kohn-Sham potential with a functional dependence on $\rho$, the electronic density. Here, the corresponding electronic density, $\rho$ is defined in terms of the Kohn-Sham wave-

function by:

$$\rho(r) \; = \; \sum_i^{occ} |\varphi_i(r)|^2 \tag{2.18}$$

The potential $\nu_{KS}[\rho(r)]$ is defined as the sum of the external potential (here normally referred to as the electrostatic potential generated by the nuclei), the Hartree potential and the exchange-correlation ($xc$) potential:

$$\nu_{KS}[\rho(r)] \; = \; \nu_{ext}[\rho(r)] + \nu_{Hartree}[\rho(r)] + \nu_{xc}[\rho(r)] \tag{2.19}$$

Due to the functional dependence on the density, these equations normally form a set of nonlinear coupled equations, and the standard procedure to solve it is through iterating until self-consistency is achieved[61] (Fig. 2.1).

In principle, any positive function normalized to the total number of electrons would work, but using an appropriate guess for $\rho_0(r)$, to start the iterative procedure can speed up convergence dramatically. For example, for a molecule or a solid-state system, one could construct $\rho_0$ from a sum of superposition of atomic charge densities:

$$\rho_0(r) \; = \; \sum_\alpha \rho_\alpha(r - R_\alpha) \tag{2.20}$$

where $R_\alpha$ and $\rho_\alpha$ represent the position and atomic charge charge density of the nucleus $\alpha$. While for an atom, a favorable choice will be the Thomas-Fermi density. We then evaluate the Kohn-Sham potential, $\nu_{KS}$ with this density, and each of the
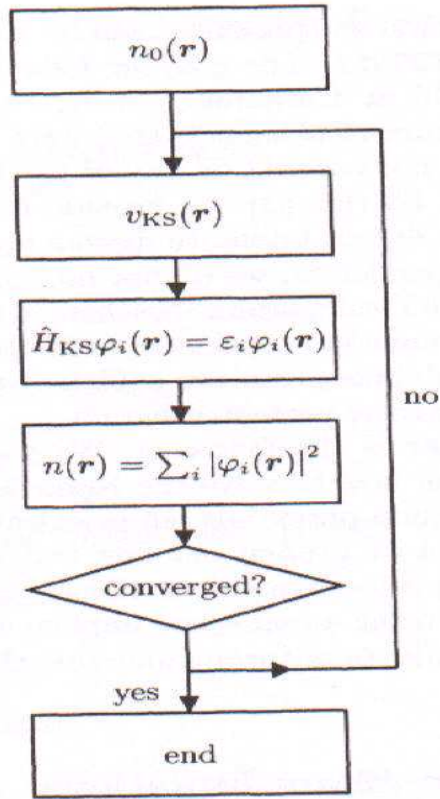
**Figure 2.1:** A flow-chart depicting a generic Kohn-Sham calculation through a self-consistency process.[97]

components of $\nu_{KS}$ is calculated separately. Here, the first component of the Kohn-Sham potential, $\nu_{ext}$ is typically a sum of nuclear potentials centered at the atomic positions, $\nu_{ext}(r) = \sum_\alpha \nu_\alpha(r - R_\alpha)$, with $\nu_\alpha$ typically is a Coulombic attraction among the electrons and nucleus. The next term, $\nu_{Hartree}$ (i.e. Hartree potential) is then is defined as: $\nu_{Hartree} = \int d^3r' \frac{\rho(r')}{|r - r'|}$, with several techniques can be used to evaluate this integral, either by direct integration or solving the equivalent differential Poisson's equation[61, 65, 98]. Finally, the exchange-correlation ($xc$) potential which formally

defined as:

$$\nu_{xc}(r) \;=\; \frac{\delta E_{xc}}{\delta \rho(r)} \tag{2.21}$$

is perhaps the most subtle part for the numerical calculation.

Among the approximate $xc$ functionals which have appeared in the literature over the years, the first to be proposed and, in fact, the simplest of all, is the local-density approximation (LDA). Besides, other possible, yet suitable choices will be the generalized gradient approximations (GGA), which has a similar form, but not only depends on the density, $\rho$, but also on its gradient $\nabla\rho$[61, 65, 66, 97]. Then, as we obtained the Kohn-Sham potential, we can solve the Kohn-Sham equation, with the goal to obtain the $p$ lowest eigenstates of the Hamiltonian $H_{KS}$, where $p$ is half the number of electrons (for spin unpolarized calculation). Then as shown in the Fig. 2.1, the self-consistency cycle is stopped when some convergence criterion are reached: i.e. when $|E^{(i)} - E^{(i-1)}| < \eta_E$ or $\int d^3 r |\rho^{(i)} - \rho^{(i-1)}| < \eta_\rho$, where $E^{(i)}$ and $\rho^{(i)}$ are the total energy and density at iteration $i$, and $\eta_E$ and $\eta_\rho$ are user defined tolerance cut-off value. If, on the contrary, the criteria have not been fulfilled, then one needs to restart the self-consistency cycle with a new density.

## 2.4 Molecular Orbital Theory (Linear Combination of Atomic Orbitals (LCAO))

Based on the Kohn-Sham calculation scheme, an essential ingredient of many DFT calculations is the representation of basis functions of the wave-function (i.e. Kohn-Sham wave-function), $\varphi$. For dealing with the problems of molecular quantum mechanics as we stated in the previous section, two methods of approximation have been developed which are capable of handling many-electron system since the early days of developments in quantum chemistry, towards a qualitative and quantitative understanding of chemical bonding. The first approach: the *valence bond (VB)* method originally from a chemical point of view, was introduced and developed based on the concept of resonance and resonance structures. This method is essentially using the Heitler-London picture[16, 99, 100] in solving the $H_2$ molecule treating electrons as being strongly-correlated particles from the first. The second one, the *Molecular Orbital Theory* (also known as Linear Combination of Atomic Orbitals, i.e. the LCAO approach), was first developed by Hund, Mulliken, and then elaborated by Slater, Hückel, Roothaan and others[79, 101, 102, 103, 104, 105, 106], is an extension of the Bohr theory of electron configurations from atoms to molecules. Here, although both approaches described are equivalent, the *Molecular Orbital Theory* which is based on the idea of independent-electron approximation as mentioned in Sect. 2.2.3, has had great success over the years, since most chemical bonds of materials are relatively weakly correlated. Therefore in a common application, the LCAO approach proves

to be an appropriate starting point, and henceforth will be adopted in this thesis.

## 2.4.1  Basis Functions or Basis Sets

There is a huge amount of information contained in the typical ground state electronic structure calculations. An efficient computational scheme must be able to manipulate this information economically with regard to CPU time, storage requirements and the number of input/output (IO) operations. Hence, in deciding on a particular set of basis functions, a compromise will have to be made between high-accuracy results, which requires a large basis set, and computational costs, which favor small basis sets. Therefore, similar arguments hold with respect to the functional forms of $\varphi$. In general, besides considering the size of the system in this study, those functional forms are of particular of concern in terms of numerical accuracy, stability, and robustness from the computational points of view. Accordingly, linear representations of one-electron functions are usually adopted under the LCAO approach. Henceforth, different functional forms have been proposed over the years. Within the LCAO scheme, either the Hartree-Fock equation or the Kohn-Sham equation, the one-electron wave function, $\varphi$ can be expanded in terms of a certain set of basis functions as follows:

$$\varphi_i = \sum_{\mu=1}^{N} C_{\mu i} \chi_\mu \qquad (2.22)$$

with the orbitals $\varphi_i$ are represented as a linear combination of a finite set of predefined N one-electron functions, which are known as the basis functions, $\chi_\mu$ as first

suggested by Roothaan[79], while the $C_{\mu i}$ are the molecular orbital expansion coefficients. Under the LCAO approximation, atomic orbitals of constituent atoms are used as basis functions. However, any set of appropriately defined functions may be used for the basis set expansion. For the mathematical completeness of an exact wave function, it requires $N \to \infty$, while in practice, only a finite number of $N$ basis functions can be included in a calculation to approximate the 'completeness' with certain accuracy. Therefore, when using linear representations, the problem of the errors related to the use of an incomplete expansion set in basis functions (i.e. finite basis sets) arises. Thus, there is the need of making such errors as small as possible, while using manageable basis sets. Each application requires a careful analysis, i.e. the art of devising a 'good' basis sets is very important, and usually it is based on experience and competence. In this respect, depending on the different interests of studies, several alternatives for the representation of the basis functions are now available in todays electronic structure simulation codes. With their own advantages and disadvantages, these basis functions can be either analytic or numerical functions, with localized or delocalized in the basis expansion, given in Eq. 2.22.

### 2.4.1.1   Gaussian Types Orbitals

In general, two kinds of basis functions have been traditionally used in molecular quantum chemistry: *Slater Type Orbitals (STOs)* and *Gaussian Type Orbitals (GTOs)*, where both are the product of spherical harmonics $Y_{lm}(\theta, \phi)$ and a radial function. Based on the intuition of Hydrogen-like orbitals, the earliest attempt proposed by

Slater[103] used exponential functions of the form: $\chi(r, \theta, \phi) = Nr^{n-1}e^{-\zeta r}Y_{l,m}(\theta, \phi)$, and the (STO) is the commonly known as the earliest version of analytical localized basis functions of molecular orbitals. Here, the $Y_{l,m}(\theta, \phi)$ is the coneventional spherical harmonics, the $N_i$ is the normalization factors defined as $[(2n)!]^{-\frac{1}{2}}(2\zeta_i)^{n+\frac{1}{2}}$, where the value $\zeta$ can be determined from some empirical rules after considering the screening of the nucleus[103]. In spite of the fact that STOs are normalized and reproduce much better the cusps of the wave function in the proximity of the nuclei, its usage has been somewhat limited. The STOs do not possess nodes in the radial functions, however it can be included by linear combination of STOs. Besides less flexibility in the bonding descrption, their disadvantages is that the one and two-electron integrals are cumbersome to calculate, and can hardly be handled analytically with high accuracy at computation[107]. Hence, the appropriate solution will be using (GTOs) as suggested by Boys[108]. Here, the GTOs can be represented either in terms of polar or cartesian coordinates as:

$$\chi(r, \theta, \phi) = NY_{l,m}(\theta, \phi)r^{2n-2-l}e^{-\zeta r^2} \tag{2.23}$$

$$\chi(x, y, z) = Nx^{l_x}y^{l_y}z^{l_z}e^{-\zeta r^2} \tag{2.24}$$

where the sum of $l_x, l_y$ and $l_z$ determines the angular part of the orbital, $\zeta$ represents the radial extent of the function. With the introduction of GTOs, the evaluation

of the three- and four- center integrals of the two-electron integrals, is essentially much simpler as all gaussian integrals are analytic in nature[109] for both cartesian and polar gaussian basis. On the other hand, it should be noted that GTOs itself cannot describe the physics of orbitals correctly for both the tails of orbitals and in the vicinity of nucleus: i.e. the $e^{-r^2}$ dependence in GTO, results in a zero slope at nucleus, instead of cusp. Consequently, a single GTO cannot properly describe the behavior of an Atomic Orbital (AO). Thus, *Contracted Gaussian Functions (CGFs)*, $\chi_\mu^{CGF}$ which includes a fixed series of linear combinations of primitive Gaussian Functions, $\chi_i^{GF}$, characterized by the same center (usually coincide with a nucleus), with same angular numbers but different exponents. This basis functions (i.e. CGFs) is thus defined as:

$$\chi_\mu^{CGF} = \sum_{i=1}^{L} d_{i\mu} \chi_i^{GF}(\zeta_{i\mu}, r) \tag{2.25}$$

where $d_{i\mu}$ is a contraction coefficient, $L$ is the length of the contraction expansion. So now, the $\varphi$ defined before can be written as:

$$\varphi_i = \sum_{\mu=1}^{N} C_{\mu i} \chi_\mu^{CGF} \tag{2.26}$$

where usually only the coefficients to the contracted Gaussian functions, $C_{\mu i}$ are optimized in SCF (i.e. self-consistent iteration) calculations.

In practice, there are a wide range of basis sets available, with the basis functions made up either by STOs and GTOs to represent the physics and chemistry of electron orbitals. If only one basis function is used to represent an occupied AO, it

is called *minimal basis set* and usually they are applied to very large molecules, as the number of basis functions are small. With regarding to this, one of the popular minimal basis set widely used is STO-3G[110]. However, due to its limitations in flexibility in bonding features descriptions, the *split valence basis sets* is the better choice. In these basis sets, each valence AO is represented by two basis basis functions, typically the first one contracted, and the second uncontracted, common examples are the: 3-21G[111, 112, 113, 114, 115, 116], 4-31G[117, 118, 119, 120], and 6-31G[117, 118, 119, 120, 121, 122] basis set. Here it is noteworthy to point out that gaussian functions are generally derived from atomic calculations. On the molecular environments, the AOs involved can deform, due to asymmetric electronic charge distributions. Hence, the contracted Gaussian cannot fully describe the orbitals in molecular environments. So in order to accomodate this deformation effect and describe the molecular environments accurately, basis functions of higher angular momenta than the valence electrons are needed to be included in the basis sets, which called *polarization functions*. Here, one of the typical popular examples of the polarized basis sets are: 6-31G(d), 6-31G(d,p). Moreover, highly diffuse (small orbital exponent) basis functions can be included in the split-valence basis sets, to mimic the orbital character of molecules with lone pairs and anions. With this regard, the 6-31+G basis set (with diffuse functions $s, p$ are added to non-Hydrogen atoms in 6-31G), and the 6-31++G basis set (diffuse functions added to hydrogen atoms also) are introduced[123].

Here, the computation tool we utilize these basic features (i.e. STOs and GTOs)

in DFT calculations is the program package called Gaussian98/03, which adopt both LCAO-HF and LCAO-DFT schemes. All the technical details and simulation features can be obtained via the manual[123] and the official website: http://www.gaussian.com/. Mostly this quantum chemistry program package will be used in *first-principles* studies on boron clusters which will be discussed in more details in chapter 3.

### 2.4.1.2 Crystal Orbitals

In this section, it is noteworthy to point out that conventional quantum chemistry and quantum solid states physics should share the same 'language' : quantum mechanics in principle. Therefore theoretically their underlying formalism should be equivalent. However in real implementations and developments, 'they' (i.e. quantum chemistry and quantum solid state physics) tend to have different 'flavors'. As a result, quantum chemistry and quantum mechanical simulation of solids have followed substantially independent paths and strategies for many years, with almost no reciprocal influences. In the implementation of computational schemes and formalisms, they started from different elementary models, especially on the representations of the basis functions for many-electron wave-function, and the underlying parameterization of electron correlation functionals[67]. Compared to quantum chemistry which evolved for molecular studies, the approach to solve many-electron problems in the solid state was rather different. Instead of focusing on molecular orbitals and chemical bonds, conventional solid state computational codes are mostly focused on fundamental properties such as the band structure, effective mass, Fermi surface, defects, impurities, electrical and

magnetic and optical properties of a material. Henceforth, various computational schemes on quantum simulation are adopted, such as the $X$-$\alpha$ method[124], Slater-Koster tight-binding[125], planewave basis with pseudopotentials[126, 127], Korringa-Kohn-Rostoker (KKR)[128, 129], orthogonalized planewaves (OPW)[130], augmented planewaves (APW)[131, 132], linear augmented planewaves (LAPW) and linear muffin tin orbitals (LMTO)[133], etc.

In spite of the computational schemes mentioned above, a natural extension of molecular quantum chemistry into a periodic system with the local analytical basis sets (i.e. GTOs) through the generalization of the Hartree-Fock and Kohn-Sham equations for crystalline solids is not impossible[134] and unique among the planewave basis functions. Within this scheme, we can represent each Crystalline Orbital (CO), $\psi_i(r, k)$ as a linear combination of Bloch functions (BF), $\phi_\mu(r, k)$, defined in terms of local functions, $\varphi_{mu}(r)$ (here referred to as Atomic Orbitals, AOs):

$$\psi_i(r, k) = \sum_\mu a_{\mu,i}(k)\phi_\mu(r, k) \tag{2.27}$$

$$\phi_\mu(r, k) = \sum_G \varphi_\mu(r - A_\mu - G)e^{ik.G} \tag{2.28}$$

with $A_{mu}$ denotes the coordinate of the nucleus in the zero reference cell on which $\varphi_{mu}$ is centered, and the sum is extended to the set of all lattice vectors, $G$. Here, the local functions can be expressed as linear combinations of a certain number, $n_G$,

of individually normalized Gaussian type functions (GTO) characterized by the same center, with fixed coefficients, $d_j$ and exponents, $\alpha_j$, defined in the input,

$$\varphi_\mu(r - A_\mu - G) \; = \; \sum_j^{n_G} d_j G(\alpha_j; r - A_\mu - G) \qquad (2.29)$$

which is similar to what we defined in previous section on GTOs in the Gaussian98/03 program package. Here, it should be emphasized that in the actual application of solid state calculations, the standard molecular basis sets cannot be used unmodified, even if they both share the same GTOs in architecture. Except for some molecular crystals[135], a variational basis set usually consists of contractions of GTFs (linear combination of GTFs with constant coefficients) needed to be carried out, with the contraction coefficients for the inner shells being defined at the isolated atom level usually used as it is, however, for the valence electrons, the coefficients needed to be modified.

Accordingly for the typical periodic codes (i.e. solid states simulation codes) which are based on the same basic schemes as conventional molecular quantum chemistry package (i.e. Gaussian98/03), the proper use of periodicity and symmetry needed to be addressed. Here, the conventional solid state physics simulation is based upon a periodic procedure expression which is infinite and translation invariant, with the assumption of a *perfect crystal*. As a matter of fact, this translation invariance has a series of interesting properties with many important consequences for simplification of the problem, and the implementation of efficient algorithms. In this case, for all

direct space program, all the relevant quantities (i.e. the Fock and overlap matrices) are evaluated in direct space (i.e. in the AO basis). In this basis, the Fock (or Kohn-Sham or overlap) matrix which has the form:

$$F_{\mu\nu}(k) \; = \; \sum_G exp(ik.G) F_{\mu\nu}(G) \tag{2.30}$$

$$F_{\mu\nu}(G) \; = \; T_{\mu\nu}(G) + C_{\mu\nu}(G) + X_{\mu\nu}(G) \tag{2.31}$$

where $F_{\mu\nu}(G)$ is the matrix element corresponding to the interaction between the $\mu$-th AO located in the *zero* cell and the $\nu$-th AO located in the G cell. The row index can be limited to the zero cell for translational invariance, however the $G$ summation extends in principle to all direct lattice vectors. $T$, $C$, and $X$ are the kinetic, Coulomb, and exchange contributions to the Fock matrix in direct space. Here, Hartree-Fock and Kohn-Sham equations differ in the last term only, further technical details about treating the integrals of Coulomb, exchange series, and DFT grid can be obtained elsewhere within this calculation scheme[135, 136]. Matrices in $k$ space take a block diagonal form, as Bloch functions are bases for the irreducible representations of the translation group. Each block has the dimension of the AO basis in the unit cell. Fortunately, only a finite and usually small subset of these blocks, corresponding to a suitable sampling of $k$ points, needs to be diagonalized because interpolation techniques[137] can be used for eigenvalues and eigenvectors in

the first Brillouin zone. Thus, the eigenvectors of the $F(k)$ matrix are then combined and anti-Fourier transformed to give $P(G)$, the density matrix in direct space, that is used to build $F(G)$ at the next cycle in a self-consistent loop (Fig. 2.1) for iterative process.

With this respect, we apply the well-established *ab initio* program code: *CRYSTAL03/06* to simulate the periodic system of boron nanostructures: $2D$ boron sheets (Chapter 4), $1D$ boron nanotubes (Chapter 5), and $3D$ crystalline boron nanotube bundles (Chapter 6) and boron bulk solids (Chapter 7). Therefore, the corresponding computational details will be discussed separately in Chapters 5, 6 and 7.

### 2.4.1.3 Planewaves and Pseudopotentials

Besides representing the basis functions of a wave function in terms of localized basis sets (i.e. GTOs), the representation using planewaves basis sets is the other popular choice, due to *Bloch's theorem*[61], which states that in a periodic solid each electronic wave function, $\psi_i(r)$ can be written as the product of a cell-periodic part and a wavelike part[138].

$$\psi_i(r) = f_i(r)exp(ik.r) \qquad (2.32)$$

Here, the cell-periodic part of the wave function can be expanded using a basis set consisting of a discrete set of planewaves whose wave vectors are reciprocal lattice

vectors of the crystals,

$$f_i(r) = \sum_G c_{i,G} exp(iG.r) \tag{2.33}$$

where the reciprocal lattice vectors $G$ defined by $G.l = 2m\pi$ for all $l$ is a lattice vector of the crystal and $m$ is an integer. Whereas each electronic wave function can be wriiten as a sum of planewaves,

$$\psi_i(r) = \sum_G c_{i,k+G} exp[i(k+G).r] \tag{2.34}$$

In a perfect periodic crystalline system, the infinite number of electrons in the solid are encountered for by an infinite number of $k$ points, and usually only a finite number of electronic states are occupied at each $k$ point. The Bloch's theorem changes the problem of calculating an infinite number of electronic wave functions to one of calculating a finite number of electronic wave functions at an infinite number of $k$ points. Therefore, this means the *occupied* states at each $k$ point contribute to the electronic potential in solid, in principle, an infinite number of calculations are needed to compute this potential. However, usually the electronic wave function at $k$ points which are very close together will be almost identical. Therefore in this case, the electronic states at only a finite number of $k$ points are required to calculate the electronic potential, and hence determine the total energy of the solid. Consequently, there are methods that have been devised for obtaining very accurate approximations to these values (i.e. electronic potential and total energy) at special sets of $k$ points

in the Brillouin zone, which known as *k-point sampling* schemes[137, 139, 140, 141].
Hence based on these schemes, the magnitude of any error in the total energy which
due to 'inadequacy' of the $k$-point sampling can always be reduced by using a denser
set of $k$ points. In principle, a coverged electronic potential and the total energy can
always be obtained provided that the computational time is available at sufficiently
dense $k$ points.

As stated by Bloch's theorem, the electronic wave functions at each $k$-point can be
expanded in terms of a discrete planewave basis sets. When planewaves are used as
a basis set for the electronic wave function, $\psi_i(r)$, the Kohn-Sham equations assume
the following form[61]:

$$\sum_{G'} [\frac{\hbar^2}{2m}|k+G|^2\delta_{GG'} + V_{ion}(G-G') + V_H(G-G') + V_{XC}(G-G')]c_{i,k+G'} = \varepsilon_i c_{i,k+G}$$

$$(2.35)$$

In this secular equation, the kinetic energy is diagonal, and the various potentials can
be described in terms of their Fourier transforms. Then, the solution of this equa-
tion can be obtained by the diagonalization of a Hamiltonian matrix whose matrix
elements, $H_{k+G,k+G'}$ are defined by the terms in the brackets in the equation above.
Here, it is noteworthy to point out that, for a planewave basis set, the coefficients
$c_{i,k+G}$ with small kinetic energy $\frac{\hbar^2}{2m}|k+G|^2$ are typically more important than those
with large kinetic energy. Thus the planewave basis set can be truncated to include
only planewaves that have kinetic energies less than some particular cutoff energy.

Together with the introduction of an energy cutoff to the discrete planewaves basis set, it produces a finite basis set. As a result, this truncation of the planewave basis set will lead to an error in computed total energy. Although in principle, it is possible to reduce the magnitude of this error by increasing the value of cutoff energy, however, in real practice, this comes along with the expense of vast computational time in the diagonalization of a huge matrix, since the dimension of the matrix, $H_{k+G,k+G'}$ is determined by the choice of the cutoff energy $\frac{\hbar^2}{2m}|k+G|^2$.

On the other hand, it is important to note that the calculations including inner-shell electrons demands a significantly higher cutoff energy, which prevents us from implementing any practical simulations based on planewaves. Furthermore, a planewave basis set in general is very poorly suited to the electronic wave function expansion, because vast numbers of planewaves are needed to expand the tightly bound core orbitals, besides of the rapid oscillations of wave functions of valence electrons in the core region. As a matter of fact, from the physics points of view, it is well known that the behavior of inner-shell electrons in molecules and crystals is similar to that of core electrons in isolated atoms, wheareas the outer-shell valence electrons in atoms constituting a material determine mostly the physics and chemistry of the materials. Hence as a way out, this problem can be overcome by the use of the *pseudopotential approximation*[127, 142, 143, 144, 145, 146, 147, 148, 149, 150, 151, 152, 153, 154], through removing the core electrons and by replacing them and their corresponding strong-ionic potential with a weaker pseudopotential, that acts on a set of pseudo

wqve functions, rather than the true wave functions as shown in Fig. 2.2 *.
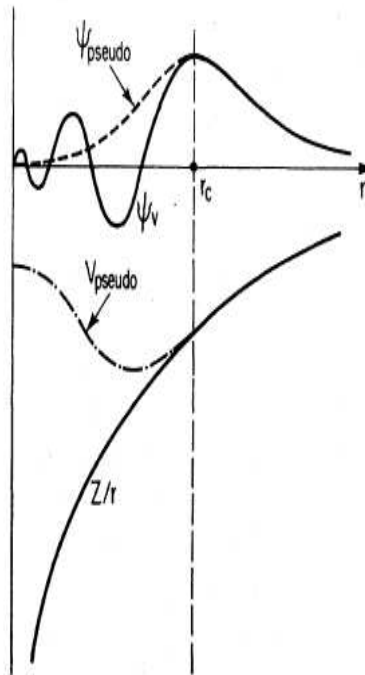


**Figure 2.2:** Schematic illustration of all-electron (solid lines) and pseudo-electron (dashed lines) potentials and their corresponding wave functions. The radius at which all-electron and pseudoelectron values match is designated $r_c$[61].

In this regard, in order to have both proper local[142, 144, 146] and nonlocal pseudopotential[127, 145, 147, 148, 149, 152] properties, capable of describing the scattering due to ions in a variety of atomic environments (i.e. transferability property), the most frequently used pseudopotential in the conventional *first-principles* calculations: the *norm-conserving* pseudopotential technique[127, 149, 154] has been proposed. Ac-

---

*Remark: The pseudopotential methods is not just applicable to planewave basis sets. In fact, it can also be found in localized basis sets, e.g. GTOs, STO, and projected augmented waves, PAW

cordingly, the pseudo wave-function which used these pseudopotentials in general must have the following characteristics:

† There are no nodes in the pseudo wave-function.

† The pseudo wave-function agrees with the all-electron wave function outside the inner-shell radius of $r_c$.

† The eigenvlues of the valence electron state using the pseudopotentials is in accordance with the eigenvalue calculated including the inner shell electrons.

† The norm $\int_0^{r_c} |u_l^{ps}(r)|^2 dr$ up to the inner shell radius of $r_c$ of the pseudo wave-function coincides with the norm of all-electron wave function up to $r_c$. Here, $u_l(r)$ is equal to $r\varphi_l(r)$, which the radial component $\varphi_l(r)$ is from the wave function $\psi_{lm}(r) = \varphi_l(r)Y_{lm}(\theta, \phi)$.

With respect to these features, the main advantages of using a truncated planewaves basis set as suggested above is rather significant. The terms which involve the Fourier transforms in the matrix elements, $H_{k+G,k+G'}$ of Kohn-Sham equation mentioned in previous, can be solved very efficiently using Fast Fourier Transform (FFT) techniques. Besides, the calculation of the energy, forces on the orbitals, forces on the

nuclei, and stress terms are simpler to solve using planewaves. There are no additional forces on the nuclei that arise from the derivative of the basis functions. This is a consequence of the fact that the *Hellmann-Feynman theorem* can be strictly applied only when the basis set is very well converged, or when the basis functions do not depend on the nuclei coordinates. Therefore, the correction for the finiteness of basis set which give rise to "Pulay forces" as found in localized basis sets will not exist[61].

With this respect, we test this powerful scheme and its underlying algoritms implemented within a popular simulation package called VASP (i.e. Vienna *ab initio* simulation package)[155, 156, 157] on the periodic and semi-periodic system of particular boron nanostructures: 2D boron sheets (Chapter 4), 1D boron nanotubes (Chapter 5), and 3D boron bulk solids. In particular, the reliability of these numerical results is compared with those obtained using localized basis sets based on CRYSTAL03/06. Furthermore, the accuracies of the numerical parameters chosen are compared to each other among the LDA and GGA, based on both ultrasoft pseudopotentials[153] and projected augmented waves (PAW)[158].

# Chapter 3

# Boron Nanoclusters: Embryo of Boron Nanotubes

## 3.1 Introduction

### 3.1.1 What are nanoclusters ?

Clusters are a finite system with a collection of atoms. Due to its 'finiteness', it is unique from its bulk constituents. In terms of the system size, clusters are intermediates between molecules and solids. Usually, they consist of only one or several types of atoms, with more than a few atoms so that that they cannot be considered as 'normal' molecules, but still small if compared to 'normal' solids[66]. Thus, as a natural extension, nanoclusters should definitely defined within a nanoscopic regime.

We now discuss a meaningful and distinct classification of nanoclusters given by Huberland[159]. This classification was based on the unique property of the clusters, namely the size- and shape-dependent variations in the properties of clusters. In small clusters, though the properties vary with the size, no smooth variations with size and shapes can be found, whereas in the medium-sized clusters the properties vary smoothly with the size. In large clusters, however, the properties are more similar to that of the bulk and are more or less independent of the size. Experimentally, it is also possible to determine the relative abundance of the clusters as a function of $N$ (i.e. number of atoms). This means that one measures the number of clusters that have a specific size. One might initially expect that this leads to a rather smooth function, but it turns out that there exist the so-called *magic number*, i.e. values of $N$ for which particularly many cluster configurations are found to be stable[66]. Hence, due to its loosely defined 'size' and topological structure, a lot of wonders can be found in such finite systems.

The study of clusters can also be based on the composition and the type of chemical bonding between the atoms forming the cluster. A cluster of a given composition may have a large number of stable structures, referred to as local minima. Likewise, there are homogeneous and heterogeneous clusters, based on the kind of atoms forming the clusters. Heterogeneous clusters can exist in two forms, namely, stoichiometric non-stoichiometric clusters. The stoichiometric clusters have the same composition as that of the corresponding bulk but exhibit properties which may be different from that of the crystal. The nature of bonding in these clusters is quite different in each

case and can vary from ionic $(NaCl)_n$, to covalent $(C_{60})$, to Van Der Waals (rare gas clusters) bonding, and to hydrogen bonding ($H_2O$ clusters). Moreover, for a given cluster, the nature of bonding can vary with the cluster size. For example, the nature of the chemical bonds in small $Hg_n$ clusters is Van der Waals, whereas for larger $Hg_n$ clusters, it is dominated by metallic-bonding[159].

Hence, there is a lot of challenges ahead in this finite size nanoscopic system for both experimentalists and theorists to outline and fill out all the possible gaps in the new 'phase-diagram' of these nanoscopic objects in varied aspects.

## 3.1.2 Why Boron Nanoclusters ?

Experimental studies on elemental boron clusters received relatively little attention in the early 1990s, though the earlier experimental observation of a prominent $B_{13}^+$ cluster has stimulated a number of theoretical investigations on the structures of small boron clusters[45, 46, 47, 48, 49, 50, 51]. In the mid 1990s, $B_{12}^+$ and $B_{13}^+$, as well as their neutral counterparts, have been shown to be planar or quasiplanar[57, 160, 161, 162, 163]. and the $3D$ icosahedral bulk-like cluster topology is not stable[49, 50]. Later, a series of photoelectron spectra succeeded in verifing these predictions[52, 164, 165, 166, 167, 168]. Henceforth, it is generally expected that boron and carbon form a set of complimentary chemical systems: the bulk carbon is stable in $2D$ graphitic structure and carbon clusters are characterized by $3D$ cages, whereas bulk boron is characterized by $3D$ cages and boron clusters are characterized by $2D$ structures. But how far does this statement hold remains an open question in the boron cluster science.

Synthesis of single-walled boron nanotubes has recently been reported showing an extreme sensitivity to the high-energy electron exposure. This experimental study opened up many unanswered questions on the stability, energetics, and the electronic properties of the nanotubular boron structures[56]. Stimulated by this experimental finding, a recent experimental study, together with computational simulations revealed that boron clusters seemed to only to favor planar ($2D$) structures up to 18 atoms, and prefer $3D$ structures beginning at 20 atoms[53]. Using the global optimization methods, they found that $B_{20}$ neutral clusters has a double-ring tubular

structure which is shown to be isoenergetic to $2D$ planar structures, which were observed and confirmed by the photoelectron spectroscopy. The $2D$-to-$3D$ structural transition observed at $B_{20}$, reminiscent of the ring-to-fullerene transition at $C_{20}$ in carbon clusters[169, 170, 171], suggests it may be considered as the embryo of the thinnest single-wall boron nanotubes.

Based on these reports, one can easily conclude that the studies of boron clusters within the small cluster regime, i.e. $B_n$ with $n \leq 15$, are rather well-established. Despite the dynamics and kinematics constraints of the growth environments, the findings to support the high stability of $2D$ planar structures over the $3D$ structures are well-supported[52, 172, 173]. However, a lot of unknowns remain unexplored in the bigger boron cluster regime, specifically the genuine relations between clusters size and the boron nanotubular structures are awaited for further studies. Thus before understanding the stability and electronic properties of a boron nanotubules like inifinite single-walled boron nanotubes, it becomes necessary to understand the physics and chemistry of medium-size and large boron clusters within a systematic study.

Our primary focus in boron nanoclusters research is clear: "a size-dependent study and its correlation with boron nanotubes". To achieve this objective, we have initiated such a study of neutral of $B_n$ clusters within three different cluster size regimes: small (i.e. $B_6$, $B_{12}$)[4], medium (i.e. $B_{24}$)[5], and large clusters (i.e. $B_{60}$)[6], in order to have an overview on their physical and chemical properties.

We will present most of our theoretical results based on Density Functional Theory (DFT) with a focus on the understanding of the trend of size-dependent structural transitions observed in boron clusters. Furthermore as recently been pointed out that the ground state configuration of neutral and ionized state of a given cluster may not be the same[174], we will investigate the ionization-induced structural changes in $B_n$. In particular, we have analyzed molecular orbitals of several conformers of $B_n$, $B_n^+$ and $B_n^-$ to establish a general pattern of physics and chemistry of boron clusters. It is expected that such an analysis will reveal an interplay between the the degree of localization of molecular orbitals and the coordination number for the cluster atoms in predicting the stability of configurational isomers of $B_n$ in general. Besides, we will also calculate, for the first time, the vibrational stability and static dipole polarizability of several isomeric configurations of $B_n$ and $B_n^\pm$ to assess the variation in the vibrational frequencies, and polarizability with different structural arrangement of boron atoms under the different 'charged' states.

The presentation of this chapter is organized as follows: In Section 3.2, we briefly describe the details of the computational methods. Results and discussion of the geometrical features, cluster stability and energetics, chemical bonding, vibrational stability, and static dipole polarizability of boron clusters, are presented in Section 3.3 accordingly. In Section 3.4, conclusions are given.

## 3.2   Computational Method

The electronic structure calculations were performed on several neutral, anionic, and cationic isomers of $B_{24}$ using the Gaussian 98 code[123]. All calculations were carried out by solving Kohn-Sham equations in the framework of density functional theory. We employed the generalized gradient approximations (GGA) using the functionals of Becke's 3-parameter hybrid exchange functional and Lee, Yang and Parr correlation functional (B3LYP)[175, 176] and a double-zeta basis set (i.e. 6-31G(d,p) or 6-31G$^{**}$ ) in these calculations (Appendix 1). We have considered the reliability and accuracy of the 6-31G(d,p) basis set in our previous study of $B_{12}$[4]. It was found that the use of a larger basis set, e.g. the 6-311G(df) basis set does not introduce significant changes in structural energetics and electronic properties of $B_{12}$ obtained by the 6-31G(d,p) basis set.

All the structures have been fully optimized by employing the gradient and updated Hessian. The convergence criteria for the gradient and energy were set to $10^{-4}$ hartree/Å and $10^{-9}$ hartree respectively. The stability of the isomers considered was addressed by computing the vibrational frequencies under the harmonic approximation with analytical force constants. We have also calculated the static dipole polarizability of all the structures by applying an external electric field of strength 0.001 a.u. along the x, y and z axes separately.

## 3.3 Results and Discussion

### 3.3.1 Structural Stability and Energetics

#### 3.3.1.1 Size Dependent Structural Transition

Firstly, it is important to note that there is a correlation between the boron nanoclusters and other boron nanostructures (e.g. boron nanotubes, boron sheets, etc.). Therefore, a study on the size-dependent structural evolution of boron nanoclusters is one of the possible way to uncover this correlation. Based on the reported works since the 1990s, it was predicted that the ground state structural configurations of small boron clusters do not resemble the fragments of either crystalline or amorphous lattice of the boron. They were predicted to be planar, convex, or quasi-planar structures[57, 160, 161, 162, 163]. Furthermore, instability of the $B_{12}$ icosahedral cluster was predicted [49, 50], though the bulk boron consists of the $B_{12}$-icosahedral networks. In order to have a more comprehensive understanding of the small boron clusters, recent theoretical work [4, 172, 173, 177, 178, 179, 180] have been focused on peculiar bonding features, static polarizability, and the vibrational properties of both the neutral and ionized clusters. In the meantime, the stability of the previously proposed planar, convex and quasi-planar structures of the neutral and ionized $B_n$ clusters, with n = 3 - 15, has been probed and also confirmed experimentally by a series of photoelectron spectroscopy measurements[52, 164, 165, 166, 167, 168]. Here, the reason for the high stbility of $2D$ planar topology found in small $B_n$ clus-

ters is rather intriguing, and can be related to its unique bonding characteristics as suggested.

Analogous to hydrocarbons, it was also proposed that the concepts of aromaticity and anti-aromaticity (Figure 3.1), can be applied to explain the cluster stability in conjunction with the planar topology found in small boron clusters regime (e.g. especially for $B_n$, where $6 \leq n \leq 15$)[52, 166, 167, 168, 181, 182]. In order to explain the high stability due to these peculiar bonding, a tentative explanation is given based on the concepts of the Hückel rule. The number of $\pi$-electron in the occupied molecular orbitals of boron clusters can be define as aromatic as $(4n + 2)$ or anti-aromatic as $(4n)$, where n is the positive integer which defines the number of sets of degenerate bonding orbitals in the molecular orbitals (MOs) diagram. Accordingly for the stable "closed-shell" system, the $B_{10}$, $B_{11}^-$ and $B_{12}$ clusters possessing six $\pi$-electrons are aromatic, while $B_{13}^-$ and $B_{14}$ possessing eight $\pi$-electrons are anti-aromatic. $B_{15}^-$ which possess ten $\pi$-electrons, is again aromatic[52].

However, when we consider larger boron clusters, obviously one can ask the question whether the Hückel rules hold for the larger boron clusters leading to the preferrence of planarity in the ground state configurations. If planarity is not preferred, then one would like to determine the cluster size where the transition to $3D$ structures is likely to occur. However, there are relatively few experimental or theoretical studies that have been performed in the cluster regime of ($B_n$, n $\geq$15). Recently, Zhai et al. have shown that the $\pi$-orbitals appear start to be localized or 'fragmented' into different parts of $B_{14}$ and $B_{15}$ clusters. Therefore, it appears that the Hückel rules which work
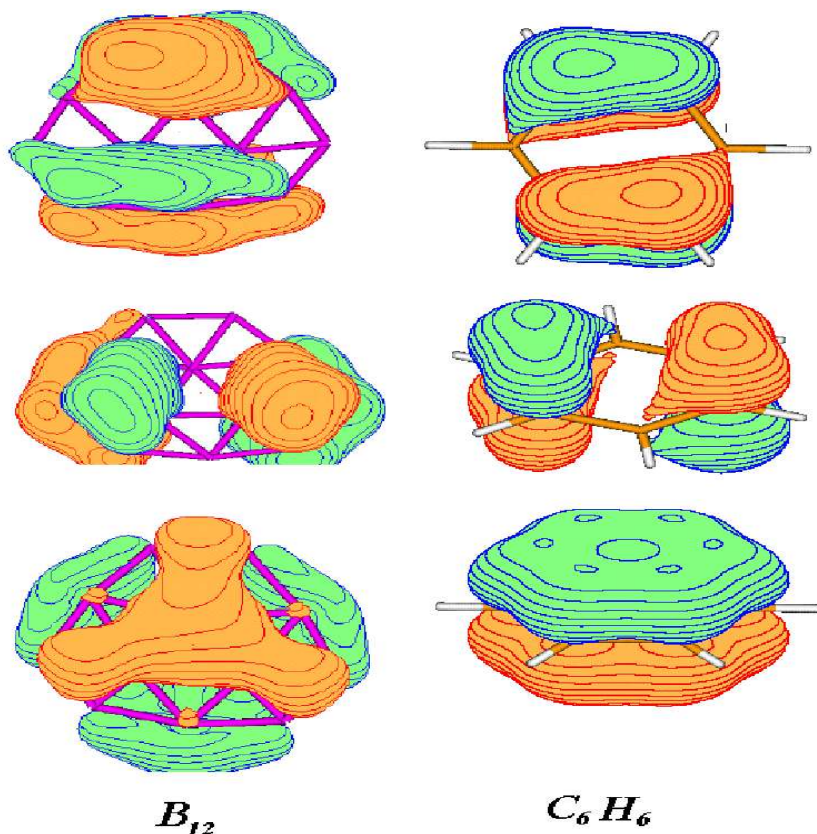
**Figure 3.1:** Selected occupied $\pi$-molecular orbitals of benzene together with those of the $B_{12}$ cluster. [4]

quite well in explaining the high stability of planarity in the small clusters may not be applicable in the large clusters. The $2D$-$3D$ transition in the structural configuration is therefore expected for the bigger cluster regime where the unsaturated dangling bonds in planarity become overwhelming.

Here, instead of performing an exhaustive exploration of all possible configurations and isomers on the potential energy surface which is very onerous, several distinctive shapes of configurations are being proposed in the bigger clusters regime. For the medium and large boron clusters (e.g. $B_{20}$[53, 183], $B_{24}$[5, 184], $B_{32}$[185], $B_{60}$[6] and

$B_{96}$[186]), the possible stable geometries of the clusters are considered in the literature for electronic structure calculations are: ring, chain, tubular, spherical cages, convex, quasiplanar, and bulk fragments as shown in Figure 3.2.

The calculated results predict that the large clusters (i.e., $B_{24}$[5, 184], $B_{32}$[185], $B_{60}$[6] and $B_{96}$[186]) favor a $3D$ tubular structure over the $2D$ planar structure regardless of the charged states of the cluster[5], with the binding energy (or cohesive energy) increase and approaching bulk limit, as size of the clusters increased. Therefore, the exact $2D$-$3D$ structural transition shown in Figure 3.3 should occur somewhere in the regime of $B_{15} < B_n < B_{24}$, and indeed the proposed range of the transition has also been suggested through the most recent experimental photoelectron spectra on $B_{20}$ [53]. In this case, the calculated results based on density functional theory at the B3LYP/6-311+G* level found the double-ring (tubular) configuration to be the ground state for both $B_{20}$ and $B_{20}^-$, but analysis of the photoelectron spectra appears to favor the planar structures. In fact, such incongruity can be explained by the difficulties associated with the experimental and computational techniques. Numerically, *first principles* calculations find the double-ring (tubular) and planar configurations to be degenerate (with $\Delta G = 0.02$ eV). Furthermore in the case of $B_{20}^-$, the four low-lying isomers are merely separated by less than 0.015eV/atom, which is the order of the precision of the quantum chemistry methods employed in the study [53]. On the other hand, experimentally it is known that the production of clusters is mainly controlled by kinematics, and is dependent on experimental techniques employed, as found in the case of $C_{20}$ [171].

In this context, the carbon clusters have been reported to have a very interesting size-dependent structural evolution starting from chains to rings to fullerenes[169]. However, such an evolution is not predicted for the boron clusters where a linear chain or a ring configuration is never found to be the preferred configuration (e.g. the monocyclic ring configuration in neutral $B_{24}$ is at 1.00 eV/atom higher than the double-ring configuration[184]). In general, the double-ring configuration in $B_{2n}$ clusters with n $\geq$ 6 is preferred in the staggered arrangements which facilitate the $sp^2$ hybridization, with the coordination number of four for each $B$ atom[6]. We note that the double-ring without the staggered configuration, and with the coordination number of three for each $B$ atom found to be less stable[4, 5, 6]. Though both carbon and boron clusters are found to exhibit the $2D$-$3D$ structural transition around a 20-atom cluster [53, 171], the dissimilar bonding characteristic determines the composition of the $3D$ configuration. The boron clusters prefer the $3D$ configuration to be a double-ring (tubular), while the carbon clusters prefer it to be a $3D$ cage-like configuration. We therefore believe that the stable cage structures, similar to those of $C_{20}$, $C_{32}$ and $C_{36}$ [169, 170, 187], are not likely to be found for the large boron clusters[6].

Here, the energetics and stability for the competition among $2D$ and $3D$ structures in boron clusters via the variation of clusters size can be defined as follows[6]. Figure 3.4 shows the size-dependent stability of the $3D$ configuration relative to the $2D$ configuration in terms of $\Delta E_{BE}$ defined as $E_{BE}(3D)$ - $E_{BE}(2D)$ for each lowest energy configuration. In the small cluster regime (e.g. $B_{12}$) where the 2D planarity is pre-

ferred, $\Delta E_{BE}$ is -0.19 eV/atom [4]. When we double the cluster-size to $B_{24}$, the $3D$ double-ring configuration gains about 0.26 eV/atom in energy yielding $\Delta E_{BE}$ to be 0.07 eV/atom[5]. Similarly, a consistent trend can also be seen in the large clusters regime for $B_{32}$, $B_{60}$ and $B_{96}$ clusters [6, 185, 186]. As also mentioned in the previous section, the emergence of preference over $2D$ planarity boron clusters can be compre- hended as a consequence of effective charge delocalization from Hückel Rules. Here, the trend in the stability of the $2D$ Vs. $3D$ configurations defined in $\Delta E_{BE}$ as shown in Figure 3.4, can be better explained in terms of a energetics competition between the curvature strain (favoring $2D$ planarity) and elimination of dangling bonds(favoring $3D$ staggard double-ring)[5, 6, 185].

Here it is worthwhile to mention that for the $B_n$ (i.e. $n \geq 20$) clusters, the experimen- tal studies are not available, and first principles calculations are rather limited. So far, only the Hartree-Fock calculations which used the standard STO-3G basis set to- gether with the symmetry-constrained optimization being used, predict the low-lying structures to be quasi-planar and tubular configurations for $B_{32}$ and $B_{96}$[185, 186] In the case of $B_{32}$, the double-ring (tubular) isomer in $D_4$ symmetry with a diameter of 8.1  Å is predicted to be more stable than $C_{2h}$ quasi-planar and $D_{4h}$ spherical cage by 0.29 and 0.36 eV/atom, respectively. The preferred topological structure of the $B_{32}$ cluster suggested that the interplay between curvature-strain and elimination of dangling bonds determine the stability among these 2D and 3D configurations. A similar argument can be applied to tubular and quasi-planar configurations of $B_{96}$. The Hartree-Fock calculations [186] reported that the segments of tubular and quasi-

planar sheet turn out to be more stable than the fragments of $\alpha$-boron solid. In $B_{60}$[6], density functional theory calculations using the standard STO-3G basis set predict the $C_{60}$-like spherical cage to be about 1.0 eV/atom less stable in energy relative to the tubular structure of diameter of about 1.53 nm. Similarly, the $C_{5v}$ boron bulk fragment (Figure 3.2) and the 2D convex (in $C_2$ symmetry) configurations are at 0.67 and 0.23 eV/atom relative to the tubular isomer.

On the other hand, the $3D$ bulk fragment (i.e. $\alpha$-boron unit-cell cluster) of $B_{96}$ is almost degenerate with the $2D$ quasi-planar sheet, though the tubular isomer with a diameter of 2.35 nm is predicted to be the ground state. Hence, it is noteworthy to point that the bulk fragments of boron can become a competitive isomeric configuration with the increase in the cluster-size, instead of $3D$ spherical cages observed in carbon clusters. We believe that as the delocalized $\pi$ MOs which are responsible in eliminating the dangling bonds of the $2D$ planar boron clusters, expected to be more 'fragment' and 'localized' in different parts of the clusters in the so-called boron 'supercluster' regime, consequently this will cause the $2D$ planarity less favorable in this regime. Therefore, the emergence of all possible boron bulk fragments based on the $B_{12}$ icosahedral networks, cannot be ignored as a probable competitive isomer for large boron clusters. We may therefore conclude that the key role in determining the structural configuration is played by the delocalized $\pi$ bonds in the small cluster regime, while the inter-icosahedral and intra-icosahedral bonds which coincide with the possible interlink of $B_{12}$ icosahedrons are expected to play an important role in determining the configurations in the large cluster regime of the elemental boron[6].

### 3.3.1.2 Neutral and Ionized States: $B_n$ and $B_n^{\pm}$

Compared to the size-dependent structural transition of boron clusters, sometimes the extra theoretical studies on its ionized clusters, $B_n^{\pm}$ may provide an useful supplementary information on the corresponding clusters for future experimental findings, e.g. photoelectron spectroscopy. In cluster science research, a photoelectron spectroscopy experiment is known to provide accurate information on the electronic structure of mass-selected negative cluster ions[188]. Instead of neutral clusters, here one can start with an anionic cluster and analyze the energy of the photodetached electron with a fixed-frequency laser. Assuming that $E(X_n^-)$ and $E(X_n)$ are, respectively, the total energies of the anionic cluster, $X_n^-$, and neutral cluster, $X_n$, the following equation must hold:

$$E(X_n^-) + h\mu \;=\; E(X_n) + E_k \tag{3.1}$$

where $h\mu$ is the energy of the photon, and $E_k$ is the kinetic energy of the ejected electron. The peaks in the photoemission spectra then correspond to the various transitions from the ground state of the anion to the neutral cluster at the ground state energy. If the ground state geometries of both anion and neutral clusters do not differ much from each other, the transition peaks are narrow. Thus the broadening of the peaks provides a measure of how different the geometries of the anion and neutral cluster could be. In addition, the photoemission peaks also carry information about the vibrational, electronic excitations, etc. Hence, theoretical studies on these ionized

clusters are never a trivial task. Here, instead of giving exhaustive details of all sizes of the ionized boron clusters, specifically only $B_{12}^{\pm}$ and $B_{24}^{\pm}$ will be discussed. The details of the compiled results on electron affinity (EA) and ionization potential (IP) will be given in the following section.

The isomers of $B_{12}$ considered for studies, can be categorized into planar ($2D$) and $3D$ configurations. The calculated results find the neutral isomers to be in the singlet spin state. Total energy of the $3D$ structures are always higher than that of the planar structures. The most stable configuration is a convex structure with $C_1$ symmetry (i.e. $B_{12}$-I), which is in contrast to the reported $C_{3v}$ structure as the most stable configuration of $B_{12}$[52, 57, 161] The $C_1$ configuration (i.e. $B_{12}$-I) consists of three $B_7$ units which are reported[167] to be the most stable structure of $B_7$. While, the double-ring isomer is the forth lowest-energy structure (i.e. $B_{12}$-IV). Even though it is less stable relative to the convex $C_1$ structure of $B_{12}$, it is predicted to be extremely stable for large boron clusters as mentioned in the previous section. The $B_{12}$ icosahedra unit which is a fragment of the bulk is found to be more than 3 eV higher in energy than the ground state of $B_{12}$.

Here, the ionization-induced changes in ordering of the lowest-energy isomers of $B_{12}$ are found to be small. The ground state of $B_{12}^{+}$ remains in the convex $C_1$ structure, as predicted. The ordering of next two lowest energy isomers of $B_{12}^{+}$ clusters are almost same as that in the neutral clusters. In this case, double-ring with $C_1$ symmetry and $3D$ cage-type $C_{2h}$ structure are nearly degenerate with energy difference ($\Delta$E) of 0.03 eV. The optimized geometry of the $B_{12}^{+}$ icosahedra is slightly distorted from its $I_h$

symmetry and is found to be 2.78 eV higher in energy relative to the ground state. Overall, the ionization introduces small changes in the bond lengths and bond angles of the ionized clusters as compared to their corresponding neutral species.

Similar to its neutral species, the stability of the isomeric configurations of ionized $B_{12}$ can be assessed in terms of the binding energy per atom (BE) as: $E_b[B_n] = -(E[B_n] - nE(B))/n$, where $E$ is the total energy of the system and $n$ is the total number of atoms. For the lowest-energy structure of $B_{12}$, BE is 4.81 eV/atom. Our calculations shows that BE increases from $B_6$ (3.95 eV/atom) to $B_{12}$. This is consistent with the increasing trend of BE with the cluster-size approaching the cohesive energy of about 6.0 eV for the bulk boron.[189] In this case, the calculated binding energy per atom for the ground state of $B_{12}^+$ is 4.11 eV/atom, found to be less stable than its neutral species due to its electronic open-shell structure.

The lowest energy configuration of the neutral $B_{24}$ cluster is the double-ring structure ($B_{24}$-I) with $C_{4v}$ symmetry and $^1A_1$ electronic state (Fig. 3.5). Two rings of twelve boron atoms, each of diameter with 6.25 Å and 1.68 Å apart are arranged in a staggered configuration. The binding energy (BE) of this structure is 5.04 eV/atom, consistent with the increasing trend as we suggested for bigger boron clusters. The next low-lying isomer is an elongated quasi-planar configuration ($B_{24}$-II) which is 1.60 eV above the double-ring isomer. After the optimization, C$_{2h}$ configuration leads to C$_1$ symmetry. It is worth mentioning that a competition between the double-ring and elongated quasi-planar structures in becoming the ground state configuration can be understood on the basis of curvature strain (favoring quasi-planar structure)

and elimination of dangling bonds (favoring double-ring structure).[185] Two possible tubular structures, namely $3 \times B_8$ and $4 \times B_6$ were also considered here. Total energy calculations without the symmetry-constraint optimization for $D_{4h}$ configuration of $3 \times B_8$ tubular structure yields a 'square-shape' tube with $C_1$ symmetry. It is also the case with $D_{6d}$ configuration of $4 \times B_6$ tubular structure ($B_{24}$-IV) which goes to $C_1$ symmetry after the geometry optimization. The 3D isomeric configurations, such as a $D_{6d}$ cage or a spherical configuration are found to be more than 3 eV higher than the calculated ground state of $B_{24}$. It therefore suggests that the reported[169, 170, 187] stable spherical cage structures of $C_{24}$, $C_{32}$ and $C_{36}$ are not likely to be preferred configurations for the large boron clusters.

As we add one extra electron into the corresponding neutral species, $B_{24}$, all the anionic isomeric configurations of $B_{24}^-$ are found to be in doublet spin state, and are more stable in energy than their respective neutral species. The ordering of these configurations in terms of total energy is almost similar to what was calculated for the neutral $B_{24}$. Addition of an electron tends to induce a larger distance between the rings during the structural optimization. The lowest energy configuration is the double-ring ($B_{24}^{-1}$-I) structure in $C_1$ symmetry. We note that the symmetric $C_{4v}$ double-ring structure is only 0.06 eV higher in energy, making it to be nearly degenerate with the $C_1$ double-ring configuration. The next isomer is the elongated quasi-planar configuration which is about 0.47 eV higher in energy with respect to the $C_1$ double-ring isomer.

As the case with the anionic $B_{24}$, the removal of an electron does not alter the ordering

of cationic $B_{24}$ isomers, as shown in Fig. 3.5. The lowest energy configuration is still the $C_1$ double-ring structure ($B_{24}^+$-I) with a diameter of about 6.20 Å, around 0.06 eV more stable than cationic $C_{4v}$ double-ring structure.

In order to assess the effect on the ionization onto the neutral species of clusters, one has to consider the electron affinity and ionization potential of $B_n^{\pm}$. The vertical ionization potential is defined as the energy difference between the cationic and neutral clusters with both at the optimized geometry of the neutral cluster, (i.e. $IP_{vertical} = E_{q=0} - E_{q=+1}$, where E is the total energy of the cluster and $q$ is the charge on the cluster). The adiabatic ionization potential is defined as the energy difference between the cationic and neutral clusters at their own respective optimized geometries. The calculated vertical and adiabatic IP values are 8.52 and 8.40 eV, respectively. The experimental IP value[46] is reported to be 8.20 eV. The high value of the IP for $B_{12}$ is mainly due to the closed-shell electronic configuration in its ground state that provides a high stability of the cluster configuration.

## 3.3.2   Electronic Properties

### 3.3.2.1   Electron Affinity and Ionization Potential

As shown in Chapter 2, it is known that the DFT is valid for the lowest energy states in each particular symmetry (i.e. spatial and spin) channel. Since we have performed extensive structural relaxation beginning with different spatial configurations for each spin multiplicity for both $B_n$ and $B_n^{\pm}$ series (e.g. $n = 12$ and 24), we believe that

66

the ground state configurations are identified unambiguously. Therefore, comparison of properties of these states with experimental data (i.e. photoelectron spectra) can provide a further confirmation for our prediction.

Consider an anionic cluster to have $N$ number of unpaired electrons, and, hence, the relationship between the spin multiplicity $M = 2S + 1 = N + 1$, with the number of electrons in the spin-up ($n_\alpha$) and spin-down ($n_\beta$) representations is given by:

$$2S + 1 \;=\; \int [\rho^\alpha(r) - \rho^\beta(r)] \;=\; n_\alpha - n_\beta + 1 \qquad\qquad (3.2)$$

where $\rho^\alpha$ and $\rho^\beta$ are the densities of electrons with $\alpha$ and $\beta$ spins and the total electron density is $\rho^\alpha + \rho^\beta$. The direct product of symmetries of partially occupied Kohn-Sham molecular orbitals defines the spatial symmetry of a state described by a given electronic configuration.

In order to access the effect on the ionization onto the neutral species of clusters, one has to consider the electron affinity and ionization potential of $B_n^\pm$. The vertical ionization potential (VIP) which are responsible for the features in photodetachment spectra, can be evaluated as the energy difference between the cationic and neutral clusters with both at the optimized geometry of the neutral cluster, (i.e. $IP_{vertical}$ = $E_{q=0}$ - $E_{q=+1}$, where $E$ is the total energy of the cluster and $q$ is the charge on the cluster). While the adiabatic ionization potential (AIP) is defined as the energy difference between the cationic and neutral clusters at their own respective optimized geometries. Similary, the values of electron affinity (EA) are obtained as follows: $EA$

$= E_{(q=0)}$ - $E_{(q=-1)}$, where E is the total energy of the cluster and q is the charge on the cluster. In this way, the vertical electron affinity (VEA) or vertical detachment energy (VDE)[190] is defined as the energy difference between the anionic and neutral clusters with both at the optimized geometry of the anionic cluster. While adiabatic electron affinity (AEA) is defined as the energy difference between the anionic and neutral clusters at their own respective optimized geometries.

For $B_{12}^+$, the calculated vertical and adiabatic IP values using the 6-31G(d,p) basis sets are 8.52 and 8.40 eV, respectively. The experimental IP value[46] is reported to be 8.20 eV. To test the reliability and accuracy of the 6-31G(d,p) basis set used in this study, we also performed DFT calculations for the first two low-energy geometries of $B_{12}$ and $B_{12}^+$, using the 6-311G(df) basis set. With 6-311G(df), the calculated values of vertical and adiabatic IP come out to be 8.81 and 8.68 eV, respectively. The high value of IP for $B_{12}$ is mainly due to the closed-shell electronic configuration in its ground state that provides a high stability of the cluster configuration. Similarly, by using the 6-31G(d,p) basis set, the VIP and AIP values of the lowest energy configuration (double-ring, $B_{24}$-I) is 6.88 eV and 6.80 eV respectively. For elongated quasi-planar structure ($B_{24}$-II), the VIP and AIP values are 7.19 and 7.06 eV, respectively. While for convex structure ($B_{24}$-III), its VIP and AIP is 7.12 and 6.98 eV. A comparison of VIP and AIP values of these cationic isomers with those of small cationic boron clusters, $B_n^+$ ($n = 2$ - 14) [4, 160] indicates that the IPs of $B_{24}$ is showing a decreasing trend towards the bulk boron work function[46] of 4.6 eV.

To calculate VDE, we use the 6-311+G(d) basis set for the equilibrium structure

obtained using the 6-31G(d,p) basis set with an aim to obtain a more accurate value of energies, knowing that the calculated equilibrium structure of double-ring ($B_{24}$-I) remains nearly the same for both basis sets[4]. Employing the similar approach, we also calculate the vertical attachment energy (VAE) which defined as the energy difference between the neutral and anionic clusters with both at the optimized geometry of the neutral cluster. The calculated VAE and VDE values come out to be 2.67 and 2.81 eV, respectively. Thus, if the nuclear configuration of the negative ion does not drastically differ from that of the uncharged parent species, the VAE and VDE will provide lower and upper bounds, respectively[190] for the electron affinity of the double-ring $B_{24}$. Hence, by applying the concept of quantification of chemical hardness[191] of a particular system as $\eta \approx (IP - EA)/2$ where IP and EA are the first vertical ionization energy and electron affinity of the chemical species, the double-ring $B_{24}$ is found to be the most chemically inert among the other $B_{24}$ isomers by having the highest value of $\eta$, besides it is energetically the most stable.

### 3.3.2.2   Chemical Bonding

In boron clusters, the chemical bonding is dominated by the 'electron-deficient' character in a sense that more atomic orbitals are available for the bonding than electrons associated with atoms. Thus, multi-center bonds such as the delocalized bonding on three-center triangular $B - B - B$ units, are expected to become a key bonding feature in boron compounds to accommodate their electron deficiency[14]. It then results in the tendency of the boron atoms to prefer configuration based on a polyhedral unit

(e.g. $B_{12}$ icosahedral unit) in which the triangular faces prevail. However, at the cluster level, calculations predict the preference of planar isomers over three-dimensional isomers, including the icosahedral unit. To understand the difference in the preferred configurations at the cluster and bulk level, we have performed analysis of molecular orbitals for $2D$ planar, $3D$ double-ring, and other isomers for both small and large clusters. Similar to the previous section, we will dicuss the bonding properties only on $B_{12}$ and $B_{24}$ in this section.

In general, in order to analyse the bonding characters in a clusters, several theoretical techniques are available[66, 123]. Based on the Natural Bond Orbital (NBO) analysis[192], we find that the isomeric configurations of boron clusters we considered generally prefer $sp^2$-like hybridization, as the case with $B_6$ in small clusters[4]. For example, the lowest-energy configuration (i.e. $2D$ planar $B_{12}$-I), the natural electron configuration for the atoms are $(\text{core})2s^{0.88}2p^{2.03}$, $(\text{core})2s^{0.82}2p^{2.09}$ and $(\text{core})2s^{0.55}2p^{2.66}$. While for the $3D$ double-ring structure (i.e. $B_{12}$-IV), the natural electron configuration for the atoms is $(\text{core})2s^{0.76}2p^{2.22}$. On the other hand, the natural electron configurations of the the icosahedra isomer are$(\text{core})2s^{0.88}2p^{2.12}$, $(\text{core})2s^{0.66}2p^{2.31}$ and $(\text{core})2s^{0.67}2p^{2.30}$. Besides NBO analysis, the general qualitative trend of bonding characters in $B_n$ can also be accessed via Mulliken Population[66]. Here, Mulliken-partitioned atomic charge analysis generally suggests a negligible charge transfer among atoms in the $B_n$ isomers, showing the significant electron sharing feature found in typical covalent bonding. Thus based on these two bonding analysis, one can suggest that the mixing of $2s$ and $2p$ orbitals among boron atoms in the clusters

is expected to play an important role in forming the covalent bond which stabilizes the atomic binding, irrespective to its structural configurations.

Here, for an example in $B_{24}$, the unique bonding features of boron clusters can also be visualized through the electron distribution on each molecular orbitals (MOs). In Fig. 3.6, we present the analysis of the molecular orbitals (MOs) for the ground state of $B_{24}$, $B_{24}^{-}$, and $B_{24}^{+}$. This analysis reveals the interesting features of delocalized $\pi$, $\sigma$, and multi-centered $\sigma$ bonds between the boron atoms in these clusters. Instead of giving exhaustive description of these MOs, we will only extract general features of the bonding orbitals using the notation HOMO-$n$ to represent the $(60\text{-}n)^{th}$ occupied molecular orbital in the neutral cluster.

As shown in Fig. 3.6, the highest occupied molecular orbital (HOMO) shows the $\pi$ bond between the atoms of each ring, while the lowest unoccupied molecular orbital (LUMO) shows a lateral $p - p$ overlap between the atoms of both rings. The HOMO and (HOMO-1) are doubly-degenerate giving rise to an effective delocalization. On the other hand, (HOMO-2) and (HOMO-3) orbitals show localized $\pi$-bonding in $B_1$ state. The (HOMO-6) and (HOMO-7) degenerate orbitals show a delocalized $\pi$-bonding at the sides in $E$ state. The full-delocalization of benzene-like $\pi$ bonds between the two staggered rings is achieved in $A_1$ state of the (HOMO-8) orbital. Being facilitated by the delocalized $\pi$ bonds which are perpendicular to the plane of the double-ring structure, the benzene-like delocalized $\pi$ bonding in plane is shown in the double-degenerate (HOMO-11) and (HOMO-12) orbitals. A strong multi-centered $\sigma$ bonds is shown in the (HOMO-25) and (HOMO-29) orbitals in $E$ state which are

formed by the hybridization of $s-$ and $p-$type bonds, also seen in the neutral $B_{12}$[4].

The anionic double-ring configuration shows the similar features to those seen in the neutral case (Fig. 3.6). The HOMO is, in fact, the LUMO of the neutral cluster. Addition of an extra electron to LUMO of the neutral $B_{24}$ shifts the anionic HOMO to the lower energy relative to the energy of the neutral HOMO. It has also resulted in a shifting of the localized $\pi$ bonds and the 'benzene-like' delocalized $\pi$ bonds to (HOMO-3), (HOMO-7) and (HOMO-9) orbitals, respectively in the anionic $B_{24}$. Although the cationic double-ring configuration is found to have a similar features in their MOs, the magnitude of the electron delocalization is relatively less than that of either neutral or anionic configurations. For example, the electron density plots of the (HOMO-7) and (HOMO-15) $\alpha$-orbitals appear to be less dense and less delocalized. Furthermore, the 'benzene-like' delocalized $\pi$ bonding is not seen in MOs of the cationic $B_{24}$. We believe that absence of these features in MOs of the cationic $B_{24}$ may explain why the cationic double-ring configuration is energetically less stable than its corresponding neutral and anionic configurations.

Analysis of MOs of the other isomers of $B_{24}$ also reveals that the delocalized $\pi$ and multi-centered $\sigma$ bonds between boron atoms of the quasi-planar and convex isomers are 'fragmented' into different parts of the cluster configurations. On the other hand, the dominant features in MOs of 3D isomers are mainly associated with the localized orbitals. We may therefore conclude that the presence of delocalized $\pi$ and multi-centered $\sigma$ bonds plays an important role in stabilizing the double-ring configuration over the 2D quasi-planar and other 3D configurations for the neutral and ionized $B_{24}$

clusters.

### 3.3.3 Vibrational Properties

The initial part of this section will focus on a quick overview on how we calculate the atomic vibrations of boron clusters, which is implemented in Gaussian98/03 program suit, before the results and discussion on this section will be given.

By assuming the interaction among the individual cluster is minimal in determining the vibrational properties, within the Born-Oppenheimer approximation (i.e. adiabatic approximation in Chapter 2), we calculate the total electronic energy for a fixed nuclear coordinates for each clusters, by neglecting the nuclear spin. As given in Chapter 2, the total energy $E = E^{ele} + \frac{1}{2}\sum_{k=1}^{M} \frac{Z_k Z_l}{R_k - R_l}$ is a function of $\vec{X}$:

$$E = E(\vec{X}) = E(R_{1,x}, R_{1,y}, R_{1,z}, ....., R_{M,x}, R_{M,y}, R_{M,z}) \tag{3.3}$$

with $\vec{X}$ in the representation of cartesian coordinates. For the optimized structure $\vec{X^e}$, $E$ has a minimum. By expanding $E$ to second order about the minimum (i.e. $1^{st}$-order derivatives will be vanish at minimum), we find

$$E(\vec{X}) \simeq E(\vec{X^e}) + \frac{1}{2}\sum_{k_1,k_2=1}^{M} \sum_{\alpha_1,\alpha_2=x,y,z} \frac{\partial^2 E(\vec{X^e})}{\partial R_{k_1,\alpha_1} R_{k_2,\alpha_2}} \times (R_{k_1,\alpha_1} - R_{k_1,\alpha_1}^e)(R_{k_2,\alpha_2} - R_{k_2,\alpha_2}^e)$$

$$\tag{3.4}$$

In principle, the series can include also higher-order terms but in most practical cases, the approximation above (i.e. also called as *harmonic approximation*) is a good and quite reliable[123, 193] for our interest, and we can obtain the *Hessian matrix*, $\overline{H}$ defined as $\left(\frac{\partial^2 E(\vec{X}e)}{\partial R_{k_1,\alpha_1} R_{k_2,\alpha_2}}\right)$ for a stable configuration, which give non-negative $\overline{H}$. Then with the Hessian, this leads naturally to the so-called *dynamical matrix* defined as:

$$\overline{D} = \frac{1}{\sqrt{M_{k_1} M_{k_2}}} \frac{\partial^2 E(\vec{X}e)}{\partial R_{k_1,\alpha_1} R_{k_2,\alpha_2}} \tag{3.5}$$

in *mass weighted cartesian coordinates (MWC)* as implemented in Gaussian98/03. Then, the principal axes of inertia of the system will be determined to generate coordinates in the rotating and translating frame. The dynamical matrix, $\overline{D}$ will be transformed into internal coordinates and diagonalized. Consequently, this will yield $3N - 6$ or $3N - 5$ (i.e. for linear clusters) modes for vibrational modes leaving out the translation and rotation modes from the original $3N$ vibration modes. At this point, each eigenvalues from the diagonal matrix will be used to calculate the corresponding frequency. Then, the reduced mass, force constants, and the corresponding cartesian displacements for each vibrational modes will be calculated accordingly. Later, these quantities will be useful for predicting a series of spectroscopic properties, including infrared (IR) intensities, Raman activities, dipole polarizability, etc[123, 193].

### 3.3.3.1   Vibrational Spectrum

It is noteworthy to point out that vibrational study on clusters is crucial in locating the real minima, which gives all real vibrational modes in the spectra. For a transition state or a metastable structure, a series of imaginary vibrational modes can be found. Overall for the $3N - 6$ vibrational modes given by a $3D$ structural configuration, the addition or removal of an electron onto a boron cluster only shifts the values of each individual vibrational modes, and does not induce any significant changes in their spectra, unless a significant structural reconstruction of the corresponding anionic or cationic cluster is taking place. Therefore, one can suggest that the local geometrical configuration of a cluster is a main factor to determine the vibration spectra accordingly to its corresponding vibrational modes: bending, stretching (i.e. symmetric and asymmetric), etc.

As the vibrational properties of small boron clusters can be found elsewhere[52, 164, 165, 166, 167, 168], here we will only focus on the results and discussion in bigger clusters: $B_{24}$. The analysis of vibration spectrum of lowest energy structure: $B_{24}$ double-ring (tubular) and other tubular isomer (i.e. $4 \times B_6$) reveals the characteristic vibrational modes typically observed in carbon nanotubes, together with its corresponding IR spectrum. Hence, this suggest that double-ring and tubular isomer can be considered as the building blocks of small radii boron nanotubes, besides being a signature of $2D$-to-$3D$ structural transition in boron clusters, as we mentioned in the previous section.

Fig. 3.7 shows the distribution of the calculated vibrational frequencies of neutral, anionic and cationic $B_{24}$ which lie in the range of 30-1500 $cm^{-1}$. In general, addition or removal of an electron only shifts the values of the frequencies, and does not induce any significant changes in their spectra. It is noteworthy to point out that the calculated spectra of the double-ring and ($4 \times B_6$) tubular structures are almost similar. The tubular structure can be considered as a segment of the boron nanotube, and has the vibrational properties which are similar to those of carbon and boron nitride nanotubes.[194, 195]. For example, the frequency region below 500 cm$^{-1}$ in the ($4 \times B_6$) tubular structure are associated with different 'radial buckling modes', such as $E$, $B_1$, $B_2$, $A_1$ and $A_2$ modes, as the case with carbon nanotubes.[195]

In the neutral and ionized double-ring $B_{24}$, the low-frequency modes ($\nu \leq 500$ cm$^{-1}$) correspond to vibrations in the 'radial modes'. In the neutral case, the lowest 'radial mode', $\nu_{lowest}$, is at 77 cm$^{-1}$ which is associated with two nearly degenerate $B_1$ and $B_2$ modes. The 'radial breathing modes' at 381 and 389 cm$^{-1}$ are $A_1$ modes. It is to be noted here that the radial modes in the region ranging from 200 to 500 cm$^{-1}$ have recently been identified in the boron nanotubes by Raman experiments.[56]

The 'longitudinal modes' along the ring (tubular) axis are found to be in the region of 600-900 cm$^{-1}$, while the 'tangential modes' due to stretching of the stronger $B - B$ covalent bonds along the ring circumference are associated with frequencies above 900 cm$^{-1}$. The highest frequency of the tangential mode, $\nu_{highest}$ is 1325 cm$^{-1}$ in neutral $B_{24}$ double-ring. Addition of an electron to the neutral double-ring $B_{24}$ reduces both $\nu_{lowest}$ and $\nu_{highest}$ to 68 and 1323 cm$^{-1}$ respectively. On the other hand, the removal

of an electron reduces $\nu_{lowest}$ to 41 cm$^{-1}$, while increasing $\nu_{highest}$ to 1259 cm$^{-1}$.

The frequency spectrum of the $(4 \times B_6)$ tubular structure shows the same unique features in the vibrational modes which were seen in the double-ring configuration. The low-frequency region below 500 cm$^{-1}$ is dominated by the 'radial buckling modes'; the lowest 'radial mode' being at 139 cm$^{-1}$. The 'radial breathing mode' associated with the open ends is at 207 cm$^{-1}$. On the other hand, the breathing modes associated with the center of the tube are at 292 and 299 cm$^{-1}$. The 'tangential modes' are dominant in the frequency region of 500 - 900 cm$^{-1}$, while the 'longitudinal modes' via vibrations along the tubular axis are at about 1248 cm$^{-1}$. Since both double-ring and $(4 \times B_6)$ tubular structures exhibit the vibrational modes, which are known to be typical characteristic vibrational modes reported in $C$ and $BN$ nanotubes, these tubular structures can be considered as a basic building block of boron nanotubes. For example, $(4 \times B_6)$ structure can be considered as a segment of a boron nanotube with a radius of 0.33 $nm$.

Compared to the double-ring and other tubular structures of $B_{24}$, the elongated quasi-planar structure ($B_{24}$-II) is associated with a distinctively different distribution of frequencies, as shown in Fig. 3.7. The lowest frequency of the neutral isomer, $\nu_{lowest}$ is 36 cm$^{-1}$. The high frequency region is dominated by the symmetric and asymmetric stretching modes. The highest vibrational frequency, $\nu_{highest}$ is at 1535 cm$^{-1}$ associated with the asymmetric stretching of atoms along the edge of the plane.

### 3.3.3.2   Infrared (IR) spectra

The calculated (Lorentzian-broadened) infrared (IR) spectra of some of the isomeric configurations of neutral, and ionized $B_{24}$ clusters are shown in Fig. 3.8. We note that the prediction of infrared intensities can be accomplished by using the mixed second derivatives of energy with respect to geometric motion and an external electric field by permitting estimation of changes in the dipole moment as a function of the vibrations. Therefore the intensity (km/mole) of an infrared absorption band is proportional to the square of change in molecular electric dipole moment $\mu$ in the normal coordinates (i.e. $I_i = \text{const.} \times \left(\frac{\partial \mu}{\partial Q_i}\right)^2$).

The double-ring $B_{24}$ configuration shows the IR-active $E$ modes at 512 and 852 cm$^{-1}$ arising from its C$_{4v}$ symmetry. The peak at 512 cm$^{-1}$ is due to the 'tangential mode' while the strongest peak at 852 cm$^{-1}$ corresponds to the 'longitudinal mode'. In the ionized $B_{24}$, distribution of the IR intensities is altered due to dissimilar atomic charges. The noticeable IR peaks are at 515 and 1184 cm$^{-1}$ in $B_{24}^{-}$, while they are at 822, 1198 and 1273 cm$^{-1}$ in $B_{24}^{+}$.

In the $(4{\times}B_6)$ tubular structure, the IR peaks are more evenly distributed than those in the double-ring structure. In the low-frequency region, the IR peak at 469 cm$^{-1}$ is associated with the 'radial buckling mode'. There are two nearly degenerate 'tangential modes' at 911 and 913 cm$^{-1}$. The other two distinctive IR peaks located at 1042 and 1201 cm$^{-1}$ are associated with the 'longitudinal modes' along the tubular axis. The neutral quasi-planar and convex ($B_{24}$-II and $B_{24}$-III) structures, in general,

have relatively more widely distributed IR peaks due to their 2D extended planar configurations.

### 3.3.4 Static Dipole Polarizability

Measurements of static dipole polarizability are frequently used by experimentalists to characterize the nature of atomic, molecular and cluster species. Physically, it describes the response of the electronic cloud of the given cluster in the presence of an external static electric field. Instead of giving an exhaustive description of different characters in each isomers, we are presenting some of the features predicted by calculations in this study. Similar to their corresponding vibrational properties, in general, the calculated dipole moments, $\mu_i$ (i.e. $\mu_x$, $\mu_y$, $\mu_z$ corresponds to $\vec{E}_x$, $\vec{E}_y$, and $\vec{E}_z$ direction) of the neutral, anionic and cationic $B_n$ show a close relationship with structural symmetry of the cluster. For a cluster which does not have a center of symmetry, it will have a nonzero dipole moments (e.g. $2D$ $B_{12}$ convex structure), whereas for $3D$ cage-type and double-ring structure (i.e. $B_{12}$ and $B_{24}$, regardless of cluster size) which have a center of symmetry, a zero dipole moment is found. Accordingly, the ionization induced changes in the dipole moments become noticeable only for some of the isomers. For example, the added electron to the neutral tubular structure (e.g. $B_{24}$) appears to be shared by all the atoms. In the cationic tubular structure, however, the ionized electron appears to come from only few atoms. Therefore, no general trends is observed or can be concluded.

From electrodynamics, it is known that if a molecular cluster in which an electric dipole moment $\mu$ is induced is isotropic, then the relation between $\mu$ and the external applied electric field vector $\vec{\varepsilon}$ of the incident radiation is simply defined as: $\mu = \alpha\vec{\varepsilon}$, where $\alpha$ is a constant called the polarizability of the cluster. In general, however, for an anisotropic cluster, the relation mentioned above has to be replaced by a more complex expression as follows:

$$
\begin{pmatrix} \mu_x \\ \mu_y \\ \mu_z \end{pmatrix} = \begin{pmatrix} \alpha_{xx} & \alpha_{xy} & \alpha_{xz} \\ \alpha_{yx} & \alpha_{yy} & \alpha_{yz} \\ \alpha_{zx} & \alpha_{zy} & \alpha_{zz} \end{pmatrix} \begin{pmatrix} \varepsilon_x \\ \varepsilon_y \\ \varepsilon_z \end{pmatrix} \tag{3.6}
$$

in which the quantities $\alpha_{ij}$ are independent of the components of the electric vector, but are dependent upon the orientation of the corresponding cluster relative to the nonrotating axes, $X$, $Y$, $Z$. These quantities $\alpha_{ij}$ are called the components of a polarizability tensor by virture of their transformation under the changes of the coordinates system. Consequently under an external applied static electric field[123], a direct comparison with the parallel ($\alpha_{xx}$), transverse ($\alpha_{yy}$), and perpendicular ($\alpha_{zz}$) components of the static dipole polarizability of different isomers in the $B_n$ series reported in the previous studies[177, 178, 179] in small $B_n$ clusters is not possible because of the different orientations of x, y and z-axes chosen in calculations. Thus, we have calculated the directional averaged static polarizability, $\alpha_{avg} = (\alpha_{xx} + \alpha_{yy} + \alpha_{zz})/3$ to extract a general trend with the increase in the cluster-size. Table 3.1 shows the calculated dipole moments and the static polarizability tensor along x, y and z

directions with the total dipole moment and directional averaged static polarizability

of the low-energy configurations of $B_{24}$ and $B_{24}^{\pm}$.
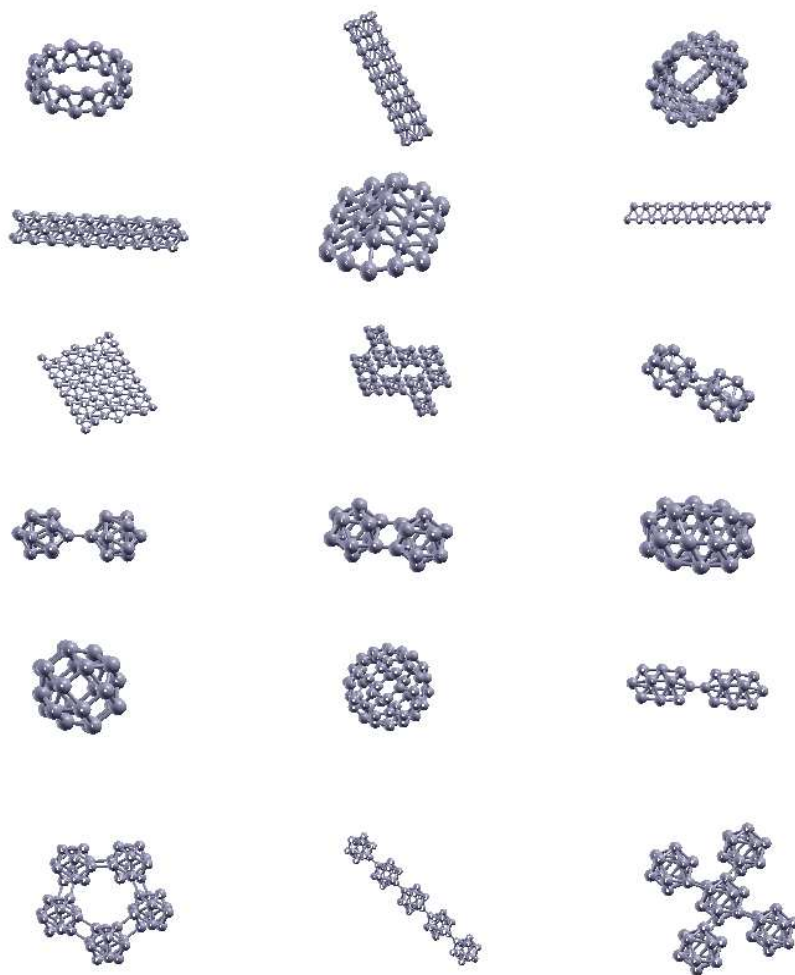
**Figure 3.2:** Several distinctive families of the possible configurations proposed in elemental boron clusters: ring, tubular, spherical cages, convex, quasiplanar, and hypothetical boron bulk fragments.
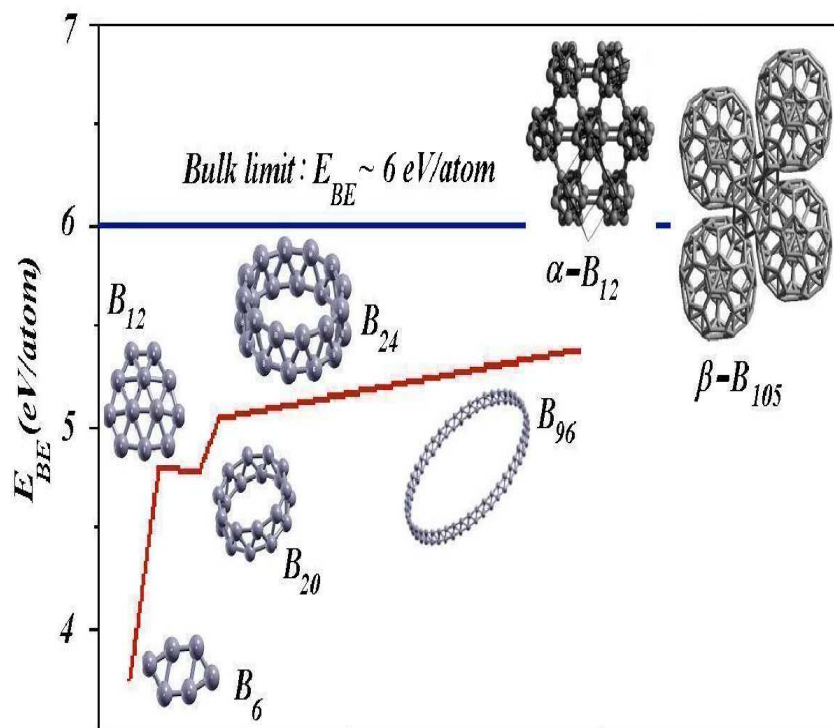
**Figure 3.3:** Size-dependent $2D$ planar to $3D$ tubular structure transition in elemental boron clusters. The figures of $\alpha$-$B_{12}$ and $\beta$-$B_{105}$ crystalline phases are taken as the references for boron bulk solid.
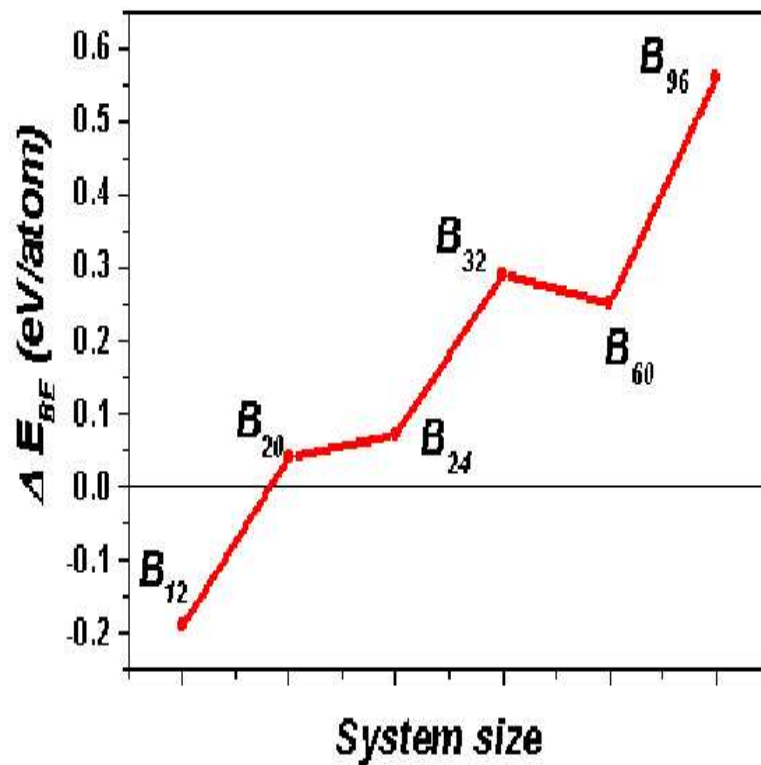
**Figure 3.4:** The size dependence of the relative stability of boron clusters (e.g. 2D planarity Vs. 3D double-ring (tubular)). The $\Delta E_{BE}$ is defined as $E_{BE}(3D)$ - $E_{BE}(2D)$. The respective values of the energy are taken from the references [4, 5, 6, 53, 185, 186]

singlet spin state, $(Q = 0)$    doublet spin state, $(Q = -1)$    doublet spin state, $(Q = +1)$

**$C_{4v}$, $B_{24}$-I**
$\Delta E = 0.00$
BE = 5.04 eV/atom

**$C_1$, $B_{24}^-$-I**
$\Delta E = 0.00$
BE = 5.13 eV/atom

**$C_1$, $B_{24}^+$-I**
$\Delta E = 0.00$
BE = 4.75 eV/atom

**$C_1$, $B_{24}$-II**
$\Delta E = 1.60$
BE = 4.97 eV/atom

**$C_1$, $B_{24}^-$-II**
$\Delta E = 0.47$
BE = 5.11 eV/atom

**$C_1$, $B_{24}^+$-II**
$\Delta E = 1.86$
BE = 4.68 eV/atom

**$C_1$, $B_{24}$-III**
$\Delta E = 1.85$
BE = 4.96 eV/atom

**$C_1$, $B_{24}^-$-III**
$\Delta E = 1.13$
BE = 5.08 eV/atom

**$C_1$, $B_{24}^+$-III**
$\Delta E = 2.04$
BE = 4.67 eV/atom

**$C_1$, $B_{24}$-IV**
$\Delta E = 2.36$
BE = 4.94 eV/atom

**$C_1$, $B_{24}^-$-IV**
$\Delta E = 2.66$
BE = 5.02 eV/atom

**$C_1$, $B_{24}^+$-IV**
$\Delta E = 3.10$
BE = 4.62 eV/atom
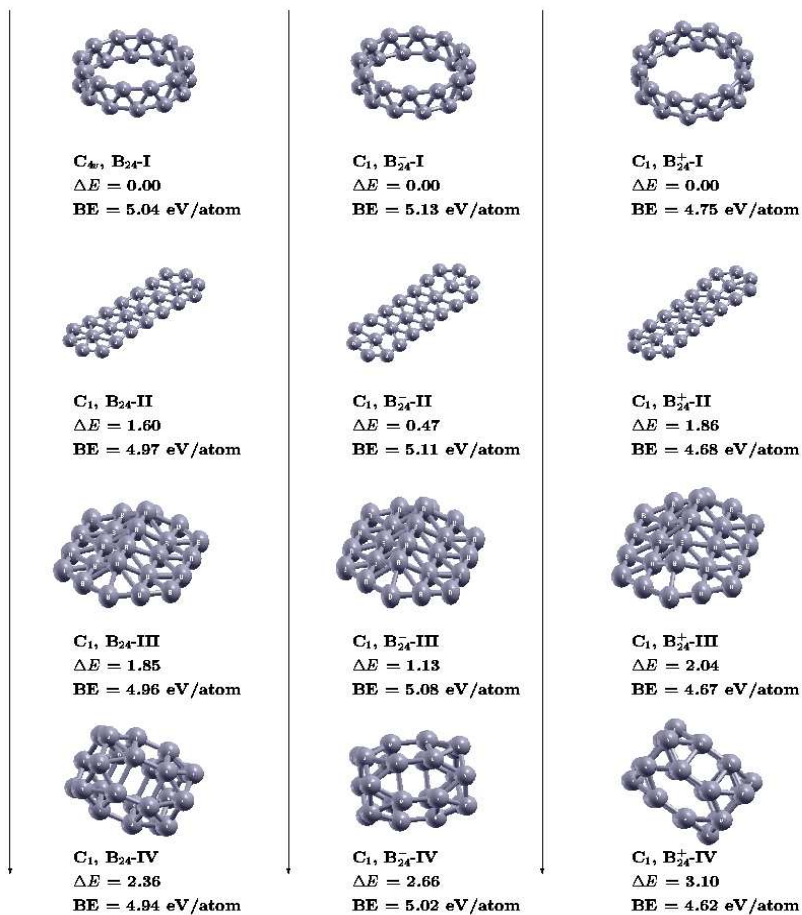
**Figure 3.5:** Energy differences ($\Delta$E in eV), binding energy (eV/atom), and symmetry for some of the low-lying isomers of neutral, anionic and cationic $B_{24}$ clusters.

MOs of double-ring, (Q = -1)    MOs of double-ring, (Q = 0)    MOs of double-ring, (Q = +1)

LUMO

HOMO

HOMO-1          HOMO-2          HOMO-2

HOMO-3          HOMO-6          HOMO-6

HOMO-7          HOMO-8          HOMO-7

HOMO-9          HOMO-11         HOMO-11

HOMO-15         HOMO-15         HOMO-15

HOMO-17         HOMO-25         HOMO-25

HOMO-26         HOMO-29         HOMO-29
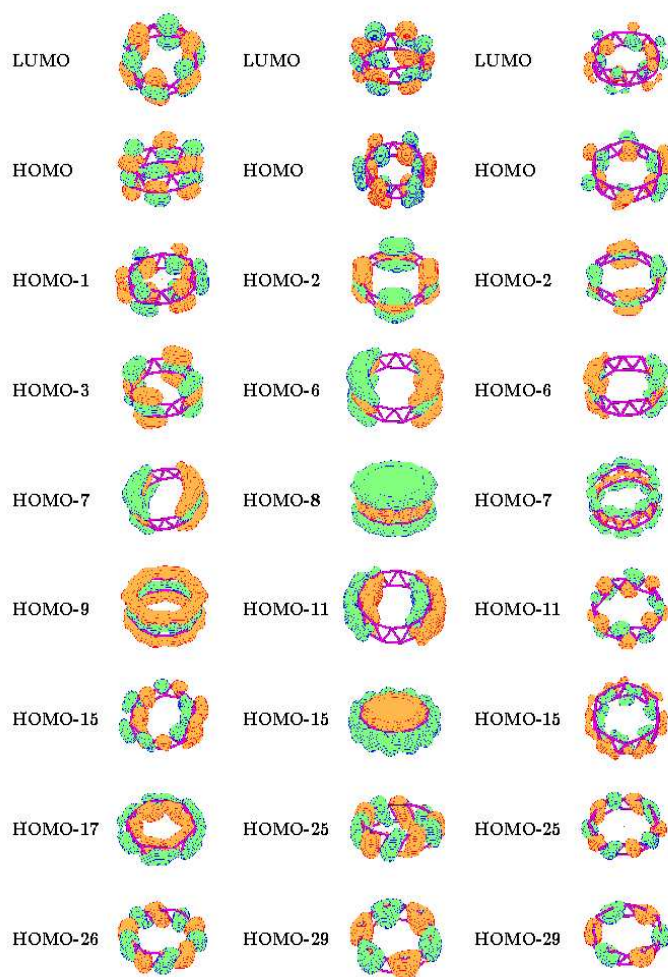
**Figure 3.6:** The selected molecular orbitals (MOs) of neutral, anionic and cationic double-ring $B_{24}$ configuration.

86
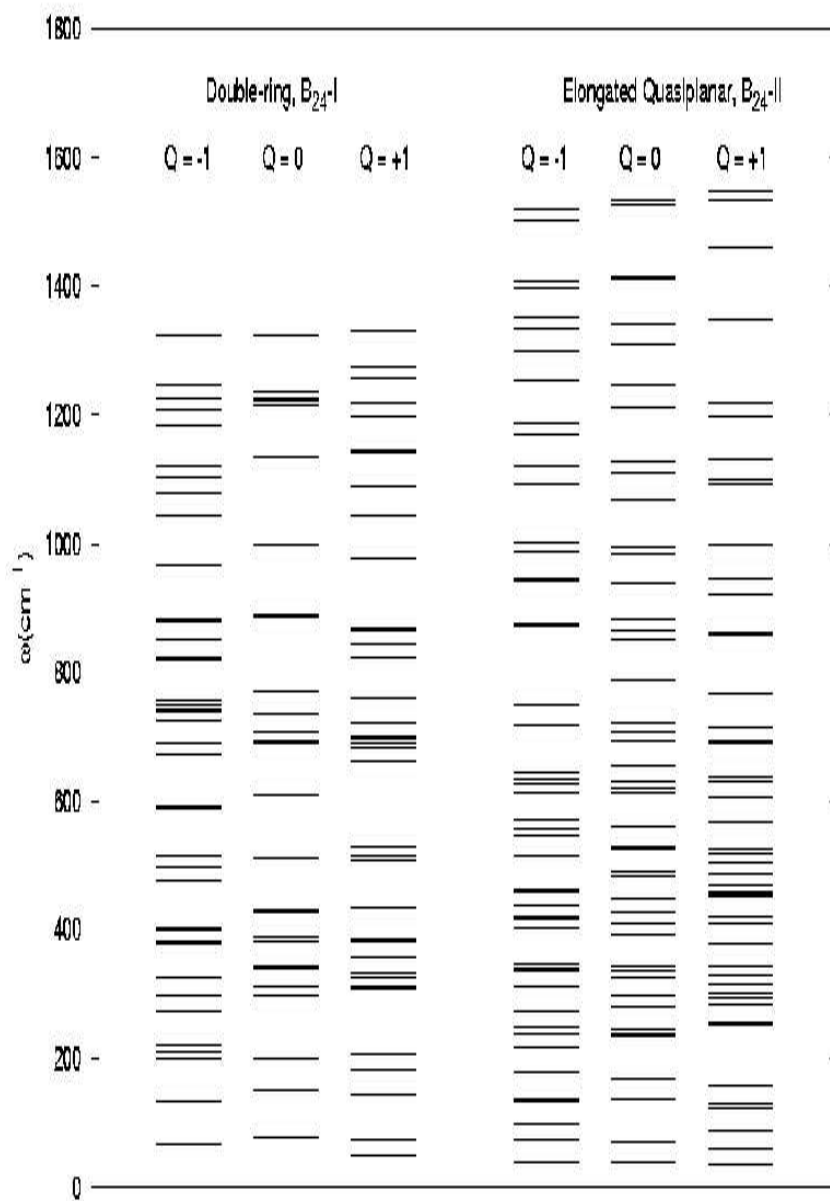
**Figure 3.7:** The calculated vibrational frequencies of the double-ring ($B_{24}$-I) and elongated quasi-planar ($B_{24}$-II) structures in the neutral, positive- and negative charge states.
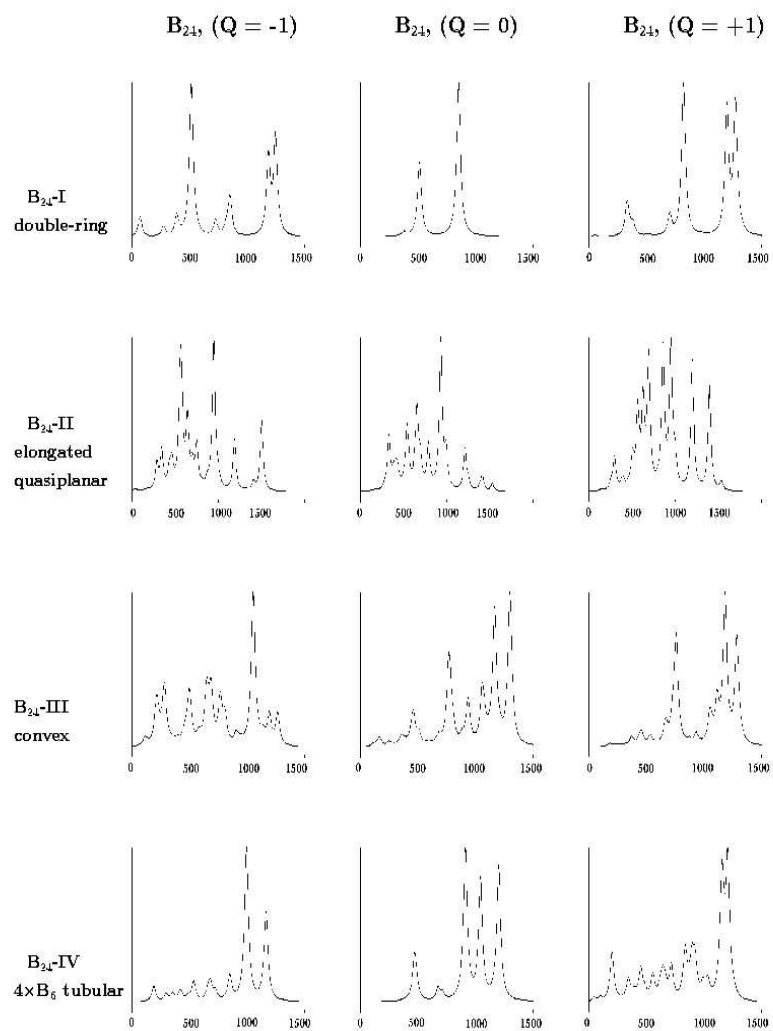
**Figure 3.8:** Infrared (IR) spectra for different isomers of the neutral, anionic andcationic $B_{24}$ clusters.

**Table 3.1:** Dipole moment ($\mu_i$ in Debye), diagonal components of static polarizability tensor($\alpha_{jj}$ in a.u.), and average static polarizability ($\alpha_{av}$ in a.u.) for the neutral, anionic and cationic isomers of $B_{24}$.

| Properties | $B_{24}$, Q= 0 | | | | $B_{24}$, Q= - 1 | | | | $B_{24}$, Q= +1 | | | |
|---|---|---|---|---|---|---|---|---|---|---|---|---|
| | $B_{24}$-I | $B_{24}$-II | $B_{24}$-III | $B_{24}$-VI | $B_{24}^{-}$-I | $B_{24}^{-}$-II | $B_{24}^{-}1$-III | $B_{24}^{-}$-VI | $B_{24}^{+}$-I | $B_{24}^{+}$-II | $B_{24}^{+}$-III | $B_{24}^{+}$-VI |
| $\mu_x$ | 0.0000 | -0.0040 | 0.0000 | -0.0002 | -0.0047 | 0.0080 | 0.0046 | -0.001 7 | 0.0039 | -0.0075 | -0.0093 | -0.0008 |
| $\mu_y$ | 0.0000 | -0.0006 | 0.0000 | -0.0009 | -0.0054 | 0.0072 | 0.0000 | -0.00 14 | 0.0001 | -0.0022 | 0.0004 | -0.1420 |
| $\mu_z$ | 0.0001 | 0.0077 | 0.4982 | -0.0003 | 0.0078 | 0.0064 | 1.1546 | -0.0017 | -0.0199 | 0.0010 | 0.4701 | 0.0161 |
| $\mu_{Tot}$ | 0.0001 | 0.0087 | 0.4982 | 0.0009 | 0.0106 | 0.0125 | 1.1546 | 0.00 28 | 0.0203 | 0.0079 | 0.4702 | 0.1429 |
| $\alpha_{xx}$ | 413.43 | 934.89 | 479.67 | 280.64 | 420.35 | 984.37 | 549.22 | 303 .66 | 407.09 | 943.75 | 471.21 | 291.77 |
| $\alpha_{yy}$ | 413.43 | 292.67 | 386.05 | 230.46 | 420.25 | 303.73 | 426.77 | 249 .40 | 406.80 | 291.40 | 371.59 | 225.03 |
| $\alpha_{zz}$ | 199.62 | 115.94 | 124.68 | 230.37 | 206.94 | 114.77 | 128.40 | 249 .33 | 194.97 | 112.81 | 123.13 | 225.24 |
| $\alpha_{av}$ | 342.16 | 447.83 | 330.13 | 247.16 | 349.18 | 467.62 | 368.13 | 267 .46 | 336.29 | 449.32 | 321.98 | 247.35 |

By extending from small to bigger clusters regime, the $\alpha_{avg}$ increase as the size of $B_n$ increase. However, the directional averaged static polarizability per atom (i.e. $\alpha_{avg}/n$, where $n$ is the total number of boron atoms in the cluster), shows overall decrease from 17.63 a.u. to 12.23 a.u. in going from $B_3$[178] to $B_{24}$[5]. The addition or removal of an electron onto the clusters, does not introduce any significant changes in $\alpha_{avg}$ of clusters (Table 3.1). The electron distribution which determine the chemical bonding in clusters, appears to be a main factor to affect the polarizability, $\alpha$. For example, the ground state of the neutral cluster (i.e. $B_{12}$-I) has a significantly less polarizability ($\alpha_{avg} = 146.79$ a.u.) as compared to that of the chain-like structure ($\alpha_{avg} = 241.60$ a.u.) reported in a previous study[179]. It suggests that the delocalization of the charge distribution in a given cluster configuration plays an important role in reducing the static dipole polarizability. The large difference in $\alpha_{avg}$ between the chain-like and convex planar structure may therefore be attributed to the localized $\pi$-electron population along chain direction[179] as compared to delocalized $\pi$ and $\sigma$ bonds in the covex planar configuration of $B_{12}$. Similarly this observation is persistent in $B_{24}$ regime. The double-ring $B_{24}$ is found to be significantly less polarizable than the elongated quasi-planar $B_{24}$, suggesting that delocalization of charge distribution plays an important role in reducing the static dipole polarizability. In the elongated quasi-planar structure, the $\pi$-electron population is expected to be localized along the chain direction.

## 3.4 Summary

The rich features of physics and chemistry of boron nanoclusters are often found dominated by its structural dimensionality and chemical bonding from which some of the qualitative features of boron clusters can easily be extracted. In this work, we review such features to discuss size-dependent structural properties of $B_n$ clusters, which covers both small-cluster regime ($n \leq 20$) and large-cluster regime ($n \geq 20$). Based on the recent observation of photoelectron spectra on $B_{20}$, the significant size-dependent structural transition can be very obvious based just on several sets of our calculations using density functional theory within a different cluster size regime: $B_6$, $B_{12}$, $B_{24}$ and $B_{60}$. From this size-dependent structural transition of $B_n$ clusters, we suggest that the preferred topological structures are the result of the interplay between bonding factors related to the delocalized $\pi$ bonds and the emergence of inter-icosahedral and intra-icosahedral bonds. The bulk fragments of boron are also expected to become a competitive isomeric configuration with the increase in the cluster-size, in contrast to $3D$ spherical cages observed in the large carbon clusters. Overall, small structural changes in $B_n$ is observed within the corresponding anionic and cationic clusters. Specifically, the removal or an addition of an electron onto $B_n$ clusters is found not to induce any significant variation in electronic, vibration and dipole polarizability properties of these clusters.

Here it is noteworthy to point out that the emergence of tubular structures in $B_n$ nanoclusters is rather unique, compared to other elemental clusters, especially on the

equilibrium geometries, energetics, stability, electronic and vibrational properties, and static polarizability of $B_{24}$ and $B_{24}^{\pm}$ clusters. *First principles* calculations based on density function theory predicts the staggered double-ring (tubular) configuration to be the ground state for $B_{24}$, $B_{24}^{-}$ and $B_{24}^{+}$ , in contrast to the $2D$ quasi-planar structure observed in small neutral and ionized $B_n$ clusters with $n \leq 15$. Furthermore, the $(4 \times B_6)$ tubular structure is found to be relatively stable in comparison to the three-dimensional cage structure. Analogous to boron crystalline solids, the presence of delocalized $\pi$ and multi-centered $\sigma$ bonds appears to be the cause of the stability of the double-ring and tubular isomers. Besides, analysis of the frequency spectrum of the double-ring and tubular isomers reveals the characteristic vibrational modes which are typically observed in carbon nanotubes. The corresponding IR spectrum also reflects the presence of some of these characteristic modes in the neutral and ionized $B_{24}$, suggesting that double-ring and tubular structures can be considered as the building blocks of boron nanotubes.

# Chapter 4

# Boron Sheets: A Precursor For Boron Nanotubes

## 4.1 Why Boron Sheets ?

As a continuation to the work discussed in the previous sections (Chapter 3) on the emergence of the nanotubular configurations, a search for the possibility of the formation of boron nanotubes has become an overwhelming important. So far, there is only one experimental paper reported on the syntheses of single-walled boron nanotubes (SWBNTs)[56] within the diameter of $\sim 3\ nm$ using Mg-MCM-41 catalyst. However, the tubular structures were found to be extremely sensitive to the high-energy electron beam. Therefore, details of the structural morphology are still unknown, and consequently their properties have not yet been fully elucidated. With this respect,

a systematic study based on a reliable computational model (i.e. *first-principles* simulation) is required.

As we know, carbon nanotubes are a structural paradigm for all nanotubular materials, and they can be seen as cylindrical modifications of graphite, which may geometrically be constructed by cutting a rectangular piece out of a single graphene sheet and rolling it up to form a tube. However, not a single direct clue can be found in boron nanotubes and boron sheets, because there is no boron sheet or graphitic like boron layers in nature. If we assume the formation of SWBNTs can be analogous to SWCNTs, which formed only under kinetically-constrained conditions on $2D$ graphene sheets, study on the possible stable structures of $2D$ boron sheets becomes necessary. Here, one can even further conjecture that: " *one of the main difficulties in synthesizing boron nanotubes appears to be the instability of a graphene-like boron sheet*". Accordingly, since the elemental boron compounds neither have a purely covalent nor a purely metallic character, we can then argue that in contrast to carbon, multi-centered bonds and electron-deficient features of boron [14, 15] are energetically more competitive and stable than bonding features with only the $sp^2$ hybridization as found in carbon graphitic system.

Analogous to SWCNTs, the correlation on the structural basis among the proposed SWBNTs and their corresponding $2D$ boron sheets can be very obvious based on the so-called 'folding mechanism'[196]. Following the same analogy, as shown in Figure 4.1, one can easily model the possible geometry of a $2D$ boron sheet based on the extension from the unique characteristic structural basis of $B_{24}$ clusters[5].

94

The two low energy tubular configurations in $B_{24}$ clusters: $2 \times B_{12}$ (double-ring), and $4 \times B_6$ (tubular) basically can be comprehended as a basic building block of a small radius SWBNT[5]. Consequently, if we extend these two tubular units along the tubular axes infinitely long, two different species of infinite SWBNTs will be formed. Subsequently, if we 'unfold' the two SWBNTs into two-dimensional structures, two distinct $2D$ boron sheets: idealized {1212} (triangular boron sheet) and reconstructed {1221} (reconstructed triangular boron sheet) are formed (Figure 4.1). In spite of this fact, similar yet slightly distinct model were proposed[57]. According to Boustani[57], one can construct a SWBNT by folding a hypothetical triangular boron sheet (i.e. idealized {1212} boron sheet in our model) which was constructed by the hexagonal pyramidal $B_7$ units based on a general 'Aufbau principle' for boron clusters. It is to be noted here that stability and electronic properties of such a triangular boron sheet has so far not been verified by experiments. Therefore, so far it remains a theoretical prediction based on *first-principles* simulation.

We have recently performed a theoretical study to investigate energetics and electronic properties of a boron sheet and the corresponding boron nanotubes[7]. The results based on density functional theory (DFT) within the generalized gradient approximation (GGA) show the relative stability of the sheet reconstructed from the planar triangular lattice[7]. On the other hand, the calculations based on local density approximation (LDA) in density functional theory find the ground state of a boron sheet to consist of a buckled triangular lattice [197, 198, 199]. Since neither GGA-DFT nor LDA-DFT calculations have resulted in an exhaustive search for the
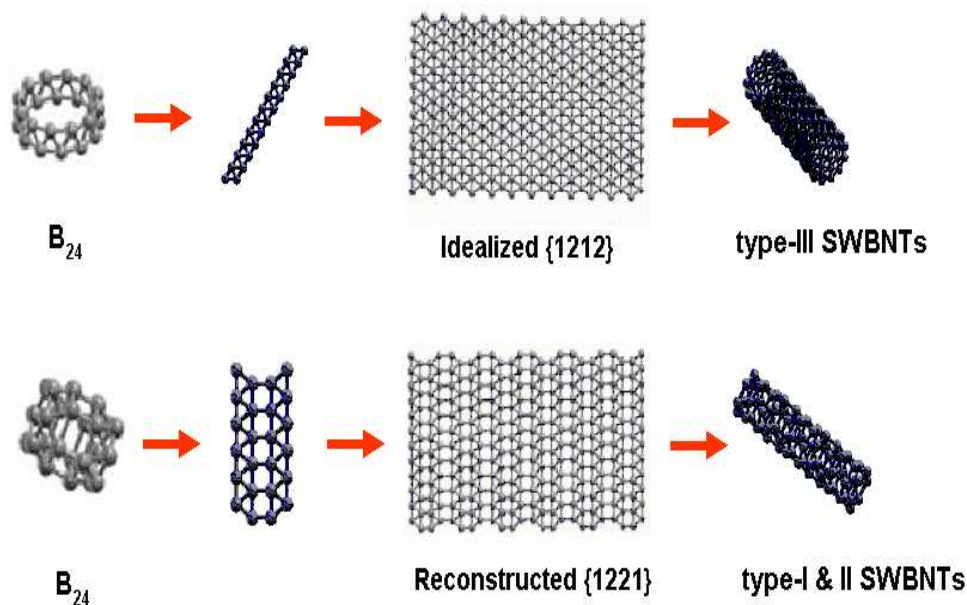
**Figure 4.1:** The 'folding-mechanism' of $2D$ boron sheet to construct a boron nanotube, based on our $B_{24}$ clusters

geometric configurations which can be considered for the stable configurations, the nature of the ground state of a 2D boron sheet still remains an open question, which we would like to address in the present study.

Henceforth, we have organized the rest of this chapter as follows. The computational method used in this work is presented in the following section. In the section of results and discussion, we present and discuss our results on structural stability, energetics, chemical bonding, and electronic properties of different $2D$ boron sheets. Then, finally a summary of the results will be given in Section 4.3.

## 4.2   Computational Methodology

Electronic structure calculations were performed under the framework of density functional theory with the Perdew-Wang (PW91) exchange and correlation functionals[200] within the generalized gradient approximation of electron density*. To utilize its $2D$ periodicity in its infinite extended geometrical congurations, a planewave basis set, mentioned in Chapter 2, was used. The valence-core interaction was described by the ultrasoft Pseudopotential (US-PP)[153] as implemented in the Vienna *ab initio* simulation package (VASP) [157]. In the course of both the cell parameters and atomic positions optimization, the $k$-space integrations were carried out using the method of Methfessel and Paxton[201] in the first order, with employed smearing width of 0.05 eV. An energy cutoff of 260 eV in the planewave expansion and of 443 eV for the augmented charge was used. The sizes of the $k$-point sampling for different systems with different unique cells were individually converged, with a precision of 5 meV/atom. For each optimized structure, total energy was again calculated by using the tetrahedron method with Blöchl corrections[158] using the cut-off energy value of 320 eV in the planewave expansion as used in VASP.

The reliability and accuracy of the computational model employed was tested on the well studied boron crystalline solid, $\alpha$-$B_{12}$, which occurs in the rhombohedral phase at ambient pressure and temperature. Table 4.1 shows that the model parameters used in the current study have successfully reproduced the results of previous

---

*The compatibility among the planewave basis set and GTOs basis sets as we mentioned in Chapter 3 is shown in Appendix 2.1

**Table 4.1:** $\alpha$-$B_{12}$ boron solid : binding energy (BE (eV/atom)) and geometrical parameters. $d_{intra}$ is the intra-icosahedral bond length, $d_{inter}$ is the inter-icosahedral, and $a$ is the lattice parameter. The unit is Å.

| Model | | | | $\alpha$-$B_{12}$ | | |
|---|---|---|---|---|---|---|
| | | BE | $d_{intra}$ | $d_{inter}$ | $a$ |
| LDA | [This Work] | 7.10 | 1.72, 1.76, 1.77 | 1.65, 1.97 | 4.97 |
| | Ref.[198] | 6.84 | - | - | - |
| | Ref.[197] | 7.37 | - | - | - |
| GGA | [This Work] | 6.18 | 1.74, 1.77, 1.80 | 1.66, 2.00 | 5.04 |
| | Ref.[198] | 6.22 | - | - | - |
| | Ref.[33] | 6.95 | - | 1.67, 1.99 | 4.98 |
| | Ref.[31] | - | 1.72, 1.76, 1.78 | 1.65, 1.98 | 4.98 |
| Experiment[202, 203] | | 5.81 | - | 1.71, 2.02 | 5.06 |

theoretical[31, 33, 197, 198] and experimental[202, 203] studies on $\alpha$-$B_{12}$ solid. Both LDA (i.e. using Perdew-Zunger-Ceperley-Alder exchange-correlation functional) and GGA results predict very similar values of the structural parameters, though the LDA overestimates the binding energies.

We have used the same set of model parameters for calculations of the boron sheet which were used for elemental structure calculations of $\alpha$-$B_{12}$. For the monolayer boron sheet, a supercell was constructed by placing a basic unit of the sheet in the $xy$-plane inside a rectangular grid with a surface-to-surface separation of $\sim 10$ Å in the $z$-direction, which ensures a negligible interaction between the sheet and its image[61]. In general, the configurations considered for the sheet were built by repeating the basic unit which is composed of 8 to 12 boron atoms depending on a given configuration. The Brillouin zone was sampled using a $8 \times 8 \times 8$ Monkhorst-Pack grid for the integration in the reciprocal space. Calculations were deemed converged when changes in total energy were less than $10^{-5}$ eV and those in the inter-atomic

forces were less than 0.01 eV/Å.

## 4.3    Results and Discussion

Owing to its vast variety of structures and complexity in bonding features, a full understanding of properties of boron nanostructures is not likely to be an easy task. Boron has three valence electrons and a short covalent radius. It can undergo $sp^2$ hybridization in forming atomic clusters that leaves one unoccupied $2p_z$ atomic orbital rendering boron to be electron-deficient. [14] Consequently, the $2D$ planar and quasi-planar boron clusters benefit from $\pi$-delocalization due to the unoccupied $2p_z$ orbitals. In fact, the anomalous stability of these planar boron clusters is attributed to aromaticity arising from $\pi$-electrons [4, 52, 160, 172, 173, 204]. However, the extension of this study in an infinite $2D$ boron sheet, is rather limited[7, 197, 198, 199]

Due to its electron-deficient character, multi-centered bonds are expected to help in understanding the way boron atoms tend to interact with each other. For example, dominance of three-centered bonds in boron compounds precludes the formation of chains or rings in boron clusters[6, 184], and leads to the importance of a B-B-B unit in boron chemistry. In this case, a three-center bond generally involves two electrons in a localized molecular orbital formed by three atomic orbitals (AOs) directed towards the center of the triangle[14, 15]. Realizing that the boron atoms tend to assume the geometries that are based on polyhedra or fragments of a polyhedra in which triangular faces prevail, our choice of sheet configurations for DFT calculations will

be based on the interplay of these bonding features, overlap of the atomic orbitals, and geometrical features in the formation of the $2D$ boron sheet with respect to the 3D boron crystal.

Since the previous studies[7, 197, 198, 199] on the boron sheet were limited in sampling the potential energy landscape, calculations were performed considering a diverse and extensive set of initial configurations with and without symmetry constraints. The resulting optimized configurations are then classified into different categories to provide a better representation of the potential energy landscape of the boron sheet.

## 4.3.1  Structural Stability and Energetics

Figure 4.2 displays the several sheet configurations divided into several distinct categories, namely hexagonal graphene-like sheet, idealized and buckled {1212} sheets, reconstructed {1221} sheets, sheets based on the icosahedral configuration, low symmetry sheets, and hybrid sheets. It is to be noted that our previous preliminary work considered only idealized {1212} and reconstructed {1221} sheet configurations.[7]

Expecting the polymorphism of boron crystalline solids to resemble that of boron sheets, some of the structural features can be extracted from the configurational parameters given in Table 4.2. Most of the sheet geometries have $\sim$ 90-92 % of the binding energy of the $\alpha$-$B_{12}$ solid, and the atomic arrangements can be found to have variations of those in the triangular {1212} lattice. The flat {1212} sheet has a six-fold coordination of boron atoms which is uniformly repeated in a basic
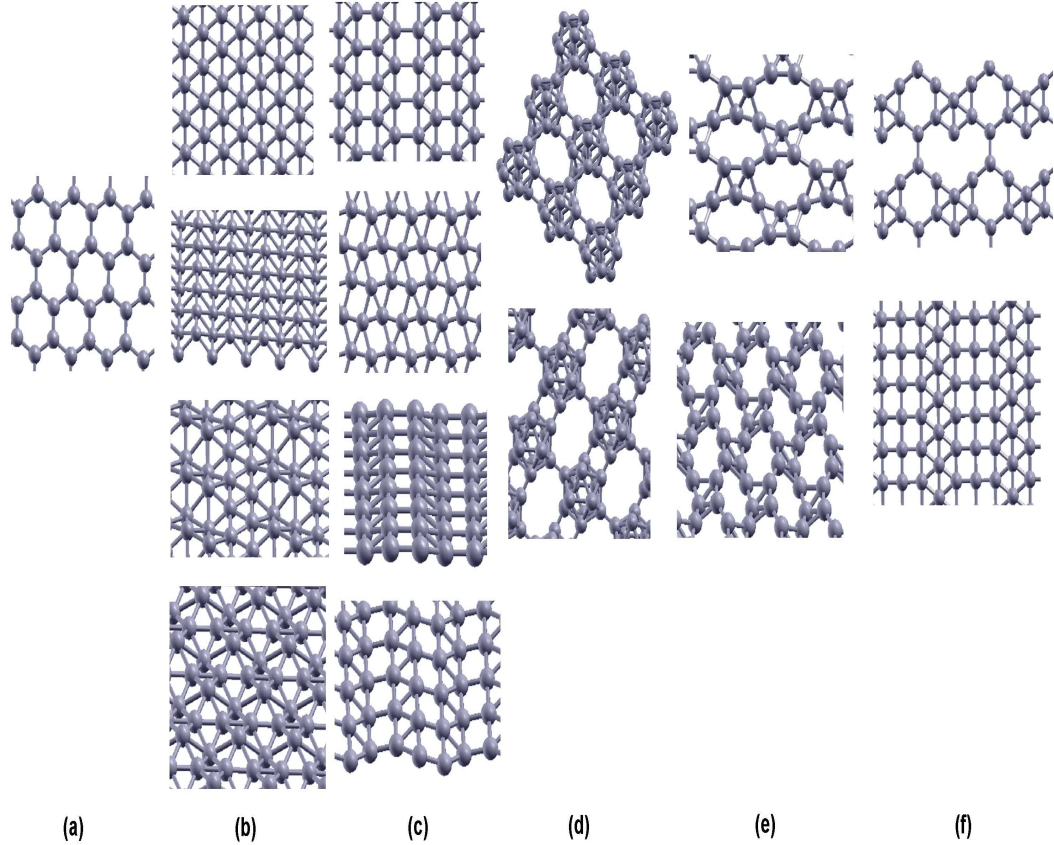
**Figure 4.2:** Boron sheets: (a) hexagonal graphene-like, (b) idealized {1212}, (c) reconstructed {1221} , (d) icosahedral, (e) low symmetry, and (f) hybrid sheets.

triangular three-atom unit. In fact, this terminology can be derived through a planar projection of the *Aufbau principle*[57] where the motifs consisting of a pentagonal pyramidal $B_6$ and the hexagonal pyramidal $B_7$ are found to be the basic unit to form elemental boron clusters. The calculated cohesive energy of the flat {1212} sheet is 5.48 eV/atom, higher than that of the $sp^2$-bonded hexagonal graphene-like boron sheet, which is only 4.96 eV/atom (Table 4.2). When symmetry of the flat sheet is broken, we find several degenerate meta-stable buckling configurations depending on the degree and direction of buckling.

Among the several candidates in the 'broken-symmetry' of flat {1212} boron sheet, the calculated results find the buckled {1212} sheet to be the most stable configuration with cohesive energy 5.70 eV/atom, achieving $\sim$ 92 % of stability of the $\alpha$-$B_{12}$ solid. The buckling has induced stability with $\triangle E = 0.22$ eV/atom over the flat {1212} sheet. The order of the stabilization energy introduced by the buckling is in agreement with the previous theoretical studies[197, 198, 199] as shown in Table 4.3. The optimized puckering height of 0.93 Å, is also comparable with the reported LDA height of 0.82-0.85 Å[198, 199].

Among all the planar isomers, the reconstructed {1221} boron sheet turns out to be the most stable configuration. It is $\sim$ 0.10 eV/atom more stable than its next competitive planar isomer, the idealized {1212} sheet. Instead of favoring the pure $sp^2$ graphene-like structure, the reconstructed configuration settles down to a 'distorted' hexagonal unit yielding a triangular-square-triangular unit network. Such a network facilitates the charge transfer, thereby forming a strong localized $\sigma$-bond with a bond length 1.63 Å. In contrast to the case of the flat {1212} sheet, buckling of reconstructed {1221} boron sheet does not appear to enhance its stability (Table 4.2).

We also find several stable configurations, other than those in the {1212} category. Despite the predicted instability of the isolated $B_{12}$ icosahedral configuration[49] in the small boron cluster regime, the 2D sheet consisting of the icosahedral network of boron atoms (i.e. icosahedral-I in Table 4.2) is the second lowest isomer with the binding energy of $\sim$ 5.60 eV/atom. The icosahedral boron sheet mimics its bulk struc-

ture, and the average inter-icosahedral, $(R_{inter})$ and intra-icosahedral bond, $(R_{intra})$ are nearly the same as in the $\alpha$-$B_{12}$ solid. Another competitive isomer arising due to a different cluster orientation, (i.e. icosahedral-II) is separated by only 0.09 eV.

Knowing that the nearly flat energy surface requires the use of more accurate methods for total energy calculations, Table 4.3 shows the calculated results obtained using the projector augmented wave (PAW) method for three representative sheet configurations. Briefly speaking, the projector augmented wave (PAW) method is analogous to pseudopotentials, that introduces projectors acting on smooth valence functions $\tilde{\psi}^v$ that are the primary objects in the calculation. It also introduces auxiliary localized functions like the "ultrasoft" pseudopotential method. However, the localized functions actually keep all the information on the core states like the OPW and APW methods[69, 158]. Thus, many aspects of the calculations are identical to pseudopotential calculations, e.g. all the operations on smooth functions with FFTs, generation of the smooth density, etc., are the same. However, the difference is that the PAW approach keeps the full all-electron wavefunction in a form similar to the general OPW expression[69, 158].

Since the full wavefunction varies rapidly near the nucleus, all the integrals are evaluated as a combination of integrals of smooth functions extending throughout space plus the localized contributions evaluated by radial integration over the muffin-tin spheres, as in the augmented planewave (APW) approach[69]. Although the PAW method is computationally intensive, it is known to provide relatively more accurate energy than the ultrasoft pseudopotentials[153] (US-PP) within DFT.[157, 158] In or-

der to get a consistent comparison among different schemes (i.e. US-PP and PAW), we have used the same set of model parameters for all calculations as we mentioned in Section II. The GGA-DFT calculations either in terms of US-PP or PAW predict the reconstructed-{1221} sheet to be energetically preferable ( $\triangle E \sim 0.10$ eV/atom) over the flat idealized {1212} sheet. At the LDA-DFT level, however, both methods (i.e. US-PP and PAW) find the reconstructed-{1221} sheet to be nearly degenerate with the idealized {1212}.

On the basis of some obvious structural similarities among boron nanoclusters (i.e. in Chapter 3), we note that the reconstructed-{1221} boron sheet can be visualized as an assembly of the ground state configuration of $B_6$ unit in $D_{2h}$ symmetry[57, 166] with aromaticity in bonding which facilitates extra stability over the other planar configurations, such as the idealized {1212} sheet.[166] To enhance the extra stability of the planar {1212} boron sheet, 'buckling' has to be induced to break the symmetry of perfect triangular lattice, to facilitate stronger localized bonds in the network. Table 4.3 also collects the LDA and GGA results for the buckled {1212} sheet which are consistent in both US-PP and PAW models, and are in agreement with the previous LDA studies.[197, 198, 199]

**Table 4.2:** Buckled and idealized {1212}, and reconstructed {1221} sheet configurations: binding energy BE (eV/atom) and the bond lengths ($R_{B-B}$).

| | Model | idealized {1212} | | buckled {1212} | | reconstructed-{1221} | |
|---|---|---|---|---|---|---|---|
| | | BE | $R_{B-B}$ (Å) | BE | $R_{B-B}$ (Å) | BE | $R_{B-B}$ (Å) |
| [This work] | LDA | 6.36 | 1.69 | 6.54 | 1.60, 1.83 | 6.33 | 1.62, 1.64, 1.92 |
| | PAW-LDA | 6.39 | 1.70 | 6.57 | 1.60, 1.83 | 6.37 | 1.62, 1.65, 1.97 |
| [This work] | GGA | 5.48 | 1.71 | 5.70 | 1.61, 1.89 | 5.57 | 1.63, 1.66, 2.00 |
| | PAW-GGA | 5.69 | 1.71 | 5.92 | 1.61, 1.88 | 5.78 | 1.63, 1.66, 2.01 |
| [$Ref.$21] | LDA | 6.53 | - | 6.79 | - | - | - |
| [$Ref.$23] | LDA | 6.06 | 1.70 | 6.27 | 1.63, 1.81 | - | - |
| [$Ref.$24] | LDA | 6.76 | 1.69 | 6.94 | 1.60, 1.82 | - | - |
| [$Ref.$23] | GGA | 5.49 | 1.71 | 5.72 | 1.64, 1.82 | - | - |

## 4.3.2 Chemical Bonding

We will now begin analysis of the chemical bonding knowing that stability of a given sheet configuration is controlled by an interplay of the valence electrons with its atomistic configuration. Indeed, we find that the atomic coordination index, $Z$ (i.e. number of nearest neighbors of a given atom in the 2D network) essentially determines the bonding features and stability of a given sheet. Furthermore, a combination of the localized two-center ($2c$) and delocalized three-center ($3c$) covalent bonds network which threads through atoms on the icosahedron surface to stabilize the lattice of a conventional 3D boron crystalline solid[14, 15, 24, 31, 32, 33, 35] plays a vital role in determining the stability of the boron sheet. Interestingly, these bonding features are accessible through the comparative study within the electron density distribution of the corresponding system. Similarly, the relative strength of the bonding can also be studied accordingly.

In order to analyse these bonding features in a consistent way, we start our bonding analysis based on our benchmark case study: $\alpha$-$B_{12}$ boron solid. In $\alpha$-$B_{12}$, boron atoms tend to form multi-center bonds in addition to two-center two-electron covalent bonds between neighboring icosahedra which typically appear at high electron density region $\sim$ of 0.95 e/$\mathring{A}^3$ (Fig. 4.3-AI). There are intra-cluster $3c$ bonds on the twenty triangular planes of an icosahedron at low density region of 0.77 e/$\mathring{A}^3$ (Fig. 4.3-AII ), and a relatively weaker inter-cluster ($3c$) bond at low density region of $\sim$ 0.60 e/$\mathring{A}^3$ (Fig. 4.3-AIII) among three icosahedra on a (111) plane of rhombohedral lattice.[14, 31, 32, 33, 35] It therefore helps us in explaining why the isolated $B_{12}$ icosahedral unit

## α-B₁₂ rhombohedral solid    icosahedral-I boron sheet



**Figure 4.3:** The equidensity surfaces of electron density with the section contour maps of the icosahedral based $\alpha$-$B_{12}$ solid (left-AI, AII and AIII), and the icosahedral-I boron sheet (right-BI,BII and BIII). The red region represents the high electron density contour, while the low electron density contour is shown by the blue region. The bonding is represented by the grey isosurfaces. AI-$2c$ inter-icosahedral bond at 0.95 e/$\text{Å}^3$. AII- $3c$ intra-icosahedral bond at 0.77 e/$\text{Å}^3$. AIII-$3c$ inter-icosahedral bond at 0.60 e/$\text{Å}^3$. BI-$2c$ inter- and intra-icosahedral bond at 0.94 e/$\text{Å}^3$. BII-$3c$ intra-icosahedral bond at 0.91 e/$\text{Å}^3$. BIII-$3c$ inter-icosahedral bond cannot be found at 0.63 e/$\text{Å}^3$.

is not stable in the small cluster regime[4, 6, 49] without the coexistence of both intra- and inter-icosahedron bonds. Indeed, such subtle bonding characters are present in

the 2D icosahedral-based (i.e. icosahedral-I and II) boron sheets.

Being one of the energetically competitive isomers among the boron sheets (see Table 4.2), the icosahedral-I sheet is being stabilized by both inter- and intra-icosahedral $2c$ $\sigma$-bonds with comparable strength (Fig. 4.3-BI). In addition, a stronger intra-icosahedral $3c$ bond (Fig. 4.3-BII) appears which can be interpreted as the preservation of the intrinsic stability of each individual icosahedron by the unusual $3c$ bonds , where the electron-deficient nature of bonding forces electrons to be shared at the triangular surfaces of the icosahedron. However, in contrast to $\alpha$-$B_{12}$, the icosahedral-I sheet has no inter-icosahedral $3c$ bonds (Fig. 4.3-BIII) at low electron density of 0.63 e/$\text{Å}^3$, as compared to the solid which possess fairly strong inter-icosahedral $3c$ bonds at 0.60 e/$\text{Å}^3$ shown in Fig. 4.3-AIII. Therefore, it might explain why the 2D icosahedral boron sheet cannot be the lowest energy isomer due to the absence of the inter-icosahedral $3c$ bond which utilizes the 3D space configuration, despite the unsaturated dangling bonds on its surface.

In the {1212} category, the atomic coordination index, $Z$ essentially determines the bonding features and stability of a given boron sheet. In the flat idealized {1212} sheet, presence of the degenerate $p$-orbitals makes the highly symmetrical planar {1212} sheet be less energetically stable (Table 4.2). Here, the atomic environment with the high coordination number (i.e. $Z = 6$) together with the electron-deficient character yield the nearly homogeneous delocalized bonds (Fig. 4.4-AI) with metallic-like bonds character, appear in this typical covalent bonded element. A homogeneous charge density distribution associated with delocalized $\pi$-electrons is dominant, as
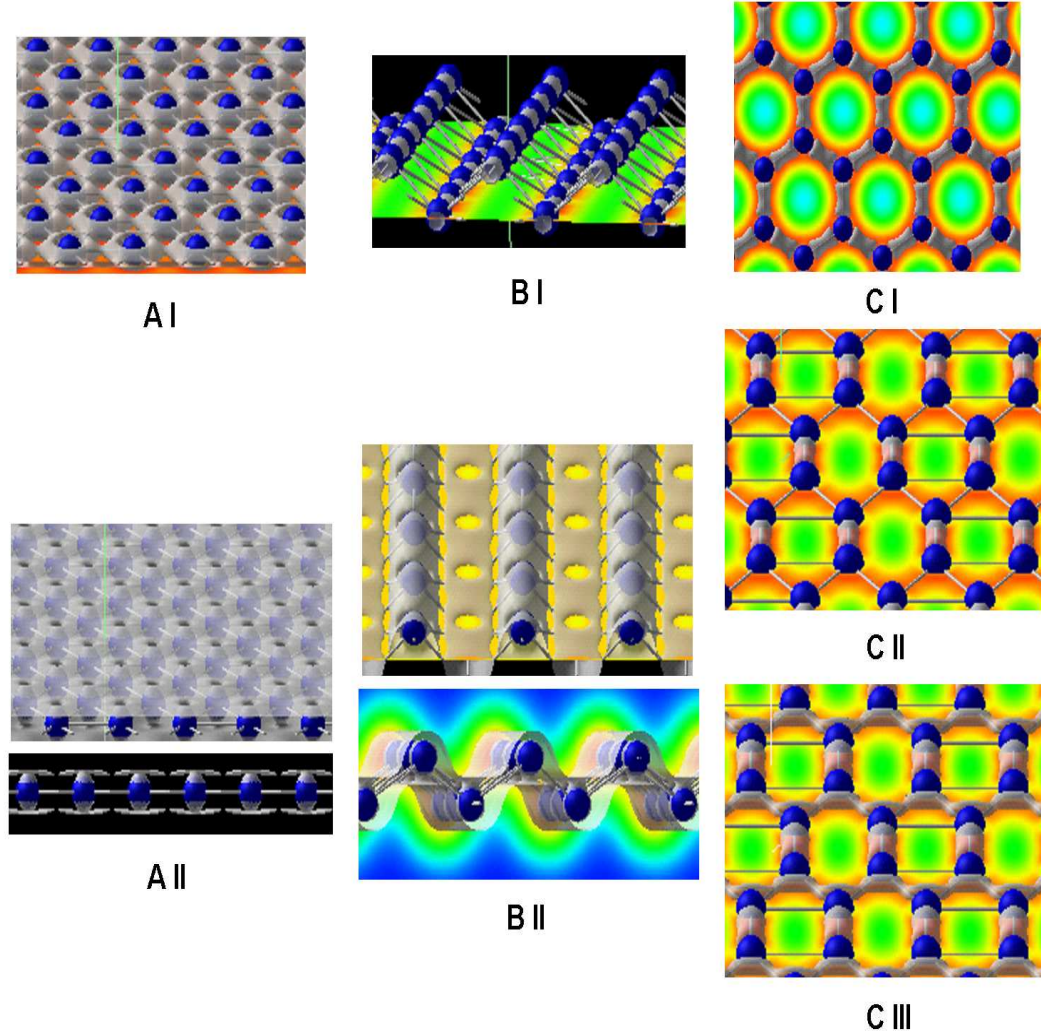
**Figure 4.4:** The equidensity surfaces of electron density with the section contour maps for the idealized {1212} (left-AI, AII), buckled {1212} (center-BI, BII), graphene-like (top right-CI) and reconstructed {1221} (right-center and bottom-CII, CIII). The red region represents the high electron density contour, while the low electron density contour is shown by the blue region. The bonding is represented by the grey isosurfaces. The isosurfaces are at 0.82 e/Å$^3$ (AI), 0.65 e/Å$^3$ (AII), 0.95 e/Å$^3$ (BI), 0.61 e/Å$^3$ (BII), 0.87 e/Å$^3$ (CI), 0.98 e/Å$^3$ (CII) and 0.87 e/Å$^3$ (CIII).

shown in Fig. 4.4-AII, for the density region around 0.65 e/Å$^3$.

When the symmetry of the planar sheet is broken by inducing a buckling height of 0.90 Å, the buckled {1212} sheet becomes the lowest energy configuration by gaining

extra stability of 0.22 eV/atom with $Z = 2$ and $Z = 4$ for the first and second

nearest neighbors. Here, the puckering stabilizes the triangular sheet by inducing a

strong directional $\sigma$-bond along the infinite boron chains (Fig. 4.4-BI) which breaks

the degeneracy of $p$-orbitals. Also, the infinite long boron chains along the 'hill' and

'valley' rows are each connected by a more delocalized weaker $\sigma - \pi$ bond between

the adjacent rows (Fig. 4.4-BII), despite the chain-like configurations are not stable

on their own in the cluster regime[5, 184]. Therefore, similar to the $B_{12}$ icosahedral

clusters based configurations (i.e. $\alpha$-$B_{12}$ solid), the buckled {1212} sheet prefers a

mixture of localized and delocalized covalent bonds, which is analogous to dominant

features of a mixed $2c$ and $3c$ covalent bonded network.

Regarding the most stable planar 2D boron sheet, the reconstructed {1221} sheet

can be viewed as a 'distorted' hexagonal ring as compared to the graphene sheet. By

altering the symmetry, the reconstructed {1221} sheet has the atomic coordination

index $Z = 1$ and $Z = 2$ for its first and second nearest neighbors in the 'triangular-

square-triangular' (i.e. {1221} lattice) network, in contrast to $Z = 3$ for the $sp^2$-

dominant (Fig. 4.4-CI) hexagonal graphene-like sheet. In a planar configuration, it

has been pointed out by Evans *et. al*[197], boron has one less electron than carbon,

which makes the bonding in the graphene-like sheet be dominated by both $sp^2$ and

$\pi$ bonds energetically unfavorable. It is likely to be the main reason why one cannot

find the analogous graphene sheet for boron in nature.

In the reconstructed {1221} sheet, there exists anisotropic chemical bonding[7, 9] with

significant contributions from the both in-plane localized directional covalent (i.e. $\sigma$-

bond) and delocalized $3c$ bonds spreading along the triangular lattice networks. The electron density distribution, shown in Figure 4.4-CIII, reveals that the charge transfer between the delocalized $3c$ bonds at 0.87 e/Å$^3$ in the network can be accommodated by the formation of directional covalent bonds (i.e. $\sigma$-bond) that interconnect these triangular units (Fig. 4.4-CII). Analogous to the case of the solids (i.e. $\alpha$-$B_{12}$) [14, 31, 32, 33, 35] and the buckled {1212}, it therefore appears that the co-existence of three-center and two-center covalent bonds makes the reconstructed {1221} sheet more stable relative to the pure $sp^2$-bonded graphene-like boron sheet. Hence, we believe, that the mixture of $2c$ and $3c$ bonds found in several lower energy 2D sheet configurations in the present study might give us an insight in understanding and designing of the boron-based novel nanostructures.

### 4.3.3  Electronic Properties

As we know, all $2D$ boron sheets are semi-periodic system, and can be properly treated within a periodic supercell technique under a continuous planewave basis. Here, all the electronic properties of $2D$ infinite boron sheets resemble the basic features of a surface. It has periodicity in the plane of the surface (i.e. boron sheet in this case), and non-periodic perpendicular to the surface. Therefore, for all the single-layered boron sheets mentioned in this study, their electronic properties can only be defined on the Brillouin zone in $k_x$ and $k_y$ plane, as defined by their corresponding $x$- and $y$- geometrical planes. Due to their varied distinction in bravais lattice and symmetry point in $2D$ Brillouin zone, we will study their electronic bands only on 0 to 0.5 from $\Gamma$ point spanning in $k_x$ and $k_y$ plane. The electronic properties of the sheet configurations considered depend on their unique atomic arrangements and bonding features. The icosahedral-I and buckled 'twisted-helix' boron sheets are semiconductors, while the rest of the boron sheets are metallic.

The semiconducting icosahedral-I boron sheet yields different features in its band diagram as compared to the metallic {1212} and reconstructed {1221} boron sheet. It possesses a rather flat band dispersion (Fig. 4.5) for both valence and conduction bands. The icosahedral-I boron sheet has an indirect band gap of $\sim$ 0.50 eV at $\Gamma$ (Fig. 4.5). Knowing that the conventional 3D boron crystalline solid (i.e. $\alpha$-$B_{12}$) and boron nanowires [54] are semiconducting, the semiconducting nature of the icosahedral sheet can be attributed to similarity of the atomistic and bonding features in the icosahedral-based configurations. Accordingly, the rich features of the $p$-states
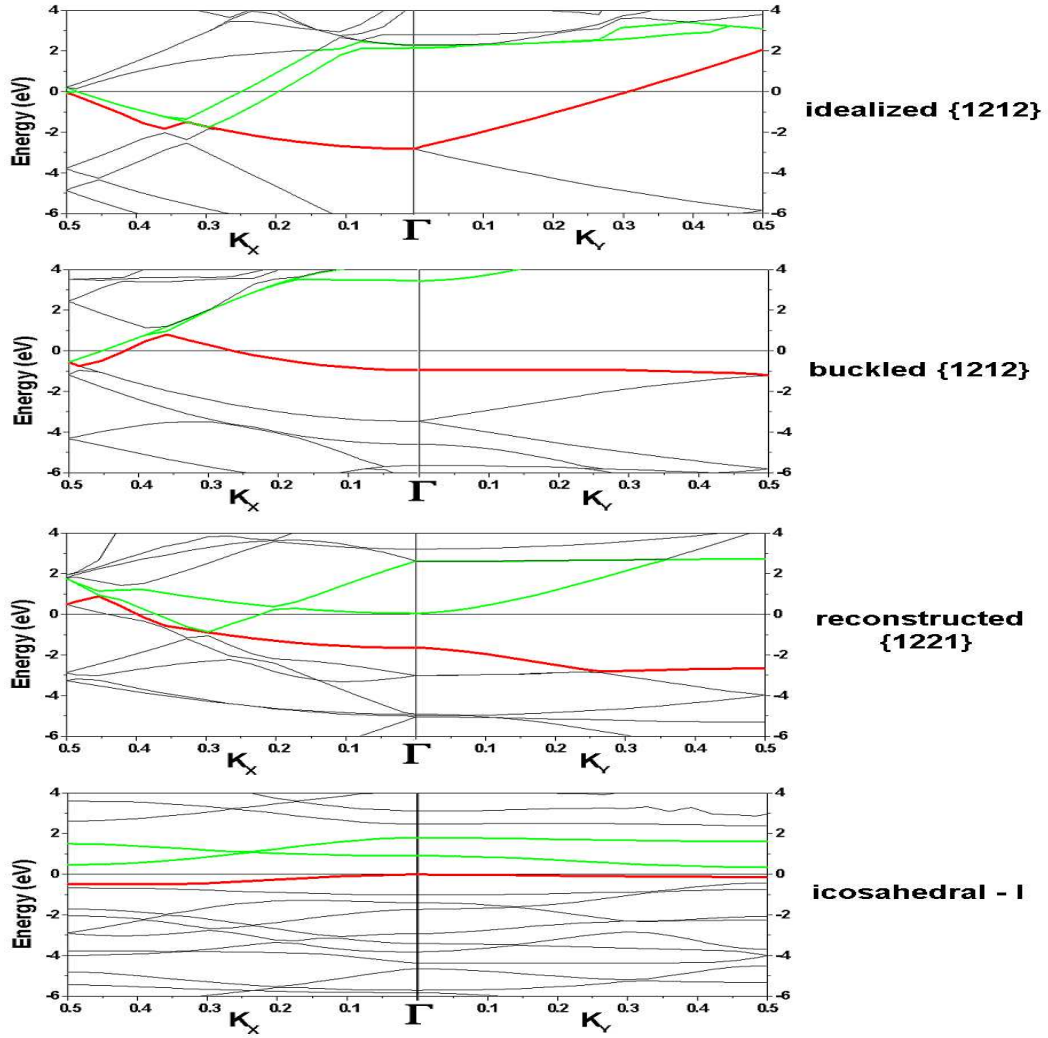
**Figure 4.5:** Band structure (from top to bottom) of the idealized {1212}, buckled {1212}, reconstructed {1221} and icosahedral-I boron sheets. Zero is aligned to the Fermi energy. The red and green lines represent the valence and conduction bands, respectively.

around the top of the valence band (Fig. 4.5) can be attributed to the localized directional inter-icosahedral $\sigma$-bonds. Whereas in the close proximity of the bottom of the conduction bands, contributions of the overlap of $s$ and $p$-states can be seen in the projected density of states.

In contrast to the icosahedral-I boron sheet, dispersion of electronic bands is rather

significant in the idealized {1212} sheet. The nearly homogeneous distribution of the electron cloud of the {1212} sheet leads to the isotropic metallic character in the band structure. A partially filled conduction band and strong overlap among valence and conduction bands can be seen in Fig. 4.5 which also displays the isotropic features of metallic character in the band dispersion along the $K_X$ and $K_Y$ directions. Total density of states shown in Fig. 4.6 indicates the appearance of the non-vanishing states near the vicinity of Fermi level, suggesting that the high electron conductivity is accessible in the {1212} sheet. From the calculated $l$-projected DOS, it can be seen that $s$ and $p$-states contribute equally to the conduction bands, and thereby indicate the occurrence of the $s$ and $p$ hybridization. Since the conduction bands are unoccupied, the no $s$-states occupied feature found in the idealized {1212} sheet might be the cause of why it is energetically less favorable as compared to the others. Buckling of the {1212} sheet induces anisotropy in the band dispersion along $K_X$ and $K_Y$ directions (Fig. 4.5). In $K_X$ direction, the conduction bands are partially filled suggesting a metallic-like character for the buckled {1212} sheet. The $l$-projected DOS identifies top of the valence band and bottom of the conduction bands to be associated with $\pi$ and $\pi^*$-states, respectively.

In the reconstructed {1221} sheet, the anisotropic nature of the chemical bonding yields different dispersions along $K_X$ and $K_Y$ directions (Fig. 4.5) in its band structure. In contrast to the planar {1212} sheet, the $l$-projected DOS shows dominant features associated with the $p$-state (i.e. $p_y$ and $p_z$ characteristics) in the proximity of Fermi level (Fig. 4.6). Accordingly, the rich features of the $p$-states around top
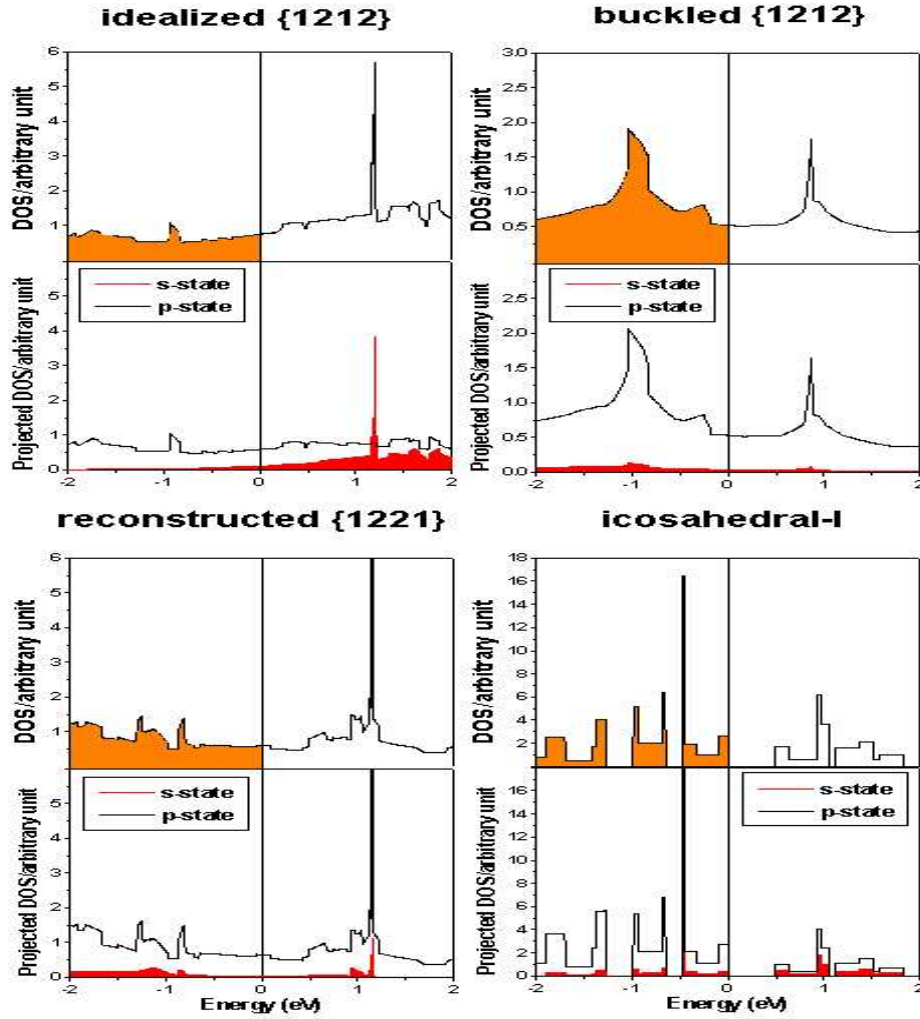
**Figure 4.6:** Total density of states, DOS (top panel), and $l$-Projected $s$ and $p$-orbital in separated cases (bottom panel). (top left) idealized {1212}*sheet*, (top right) buckled {1212} sheet, (bottom left) reconstructed {1221} sheet and (bottom right) the icosahedral-I boron sheet. Zero is aligned to the Fermi energy. The orange color shaded region on top panel represents the occupied states in DOS, while the red color shaded region on the bottom panel represents the $s$-orbital in $l$-Projected DOS.

of the flat valence band are attributed to the localized directional $\sigma$-bonds along the $Y$-direction. They open up the gap ($\sim 0.8$ eV) at $\Gamma$ along the $K_Y$-direction by lifting the degeneracy of the bands. On the other hand, the low-lying conduction bands are associated with the delocalized $p_z$-type $\pi$-bonding with bands crossing at Fermi level

in the $K_X$-direction. Similar to the buckled {1212} sheet, anisotropic features of the chemical bonding together with its band dispersion in the reconstructed {1221} sheet suggest a strong variation in the electronic and mechanical properties of the corresponding nanotubes, when the sheets are rolled into different chirality of single-walled boron nanotubes.

## 4.4 Summary

In summary, *first principles* planewave calculations were performed to study the stability, morphology and electronic properties of several sheet configurations of boron. We suggest the $2D$ boron sheets can be stable, and can achieving $\sim$ 92 % of the stability of $\alpha$-$B_{12}$ solid.

Similar to the 3D boron solids, calculations predict a varied polymorphism in the 2D boron sheets, categorized into hexagonal graphene-like, idealized {1212}, icosahedral-like, reconstructed {1221}, low symmetry amorphous-like, and the hybrid 2D sheets. From all the varieties of boron sheets in study, we found there are three promising candidates of boron sheets: idealized {1212}, buckled {1212} and reconstructed {1221}, can be utilized to form a boron nanotube, if an appropriate growth condition is available. Among the planar sheet configurations, GGA-DFT calculations predict the stability of a novel reconstructed {1221} boron sheet over the idealized {1212} triangular sheet. Instead of having nearly homogeneous electron density on the 2D plane as the case of the planar {1212} sheet, the reconstructed {1221} sheet is stabilized by co-existence of the localized $\sigma$-bonds and the delocalized three-center bonds.

The unique features in geometry and electronic properties of both {1212} and {1221} configurations suggest that a strong variation of electronic and mechanical properties is expected to occur when the plane is rolled into different chirality of single-walled boron nanotubes. Furthermore, the emergence of icosahedral-based boron sheet as

one of the low-lying configurations suggests the stability of inter-icosahedral and intra-icosahedral bonds, despite the fact that the discrete units of $B_{12}$ icosahedral unit are not stable on their own in the small cluster regime. The most stable buckled {1212} sheet is found to be stabilized by the anisotropic bond properties due to the interplay between the localized $\sigma$- and the delocalized superimpose $\sigma - \pi$-like bonds between the boron atoms in adjacent rows of boron chains.

# Chapter 5

# Single-Walled Boron Nanotubes: Pristine and Crystalline Bundles

## 5.1 Introduction

### 5.1.1 Why Boron Nanotubes ?

Following the immeasurable impact of carbon related nanostructures and the high expectations from $B_xC_yN_z$ hybrid nanostructures[205], and their corresponding $B_xC_yN_z$ ternary crystalline compounds, boron is expected to hold a very unique place, by playing vital role in the synthesis of these novel materials. Compared to the roles played by carbon, boron nitride, boron carbide, and carbon nitride, the roles played by the boron itself remains ambiguous, either in crystalline phases or in nanostructures.

Due to the versatility in its chemistry[14, 15, 18, 19] as neither being a purely covalent nor a purely metallic character, the elemental boron nanostructures itself can be remarkably interesting. So far in experiments, the studies in elemental boron nanostructures: such as nanowires, nanoribbons, nanowhiskers, and nanotubes remain at the infant stage[54, 55, 56]. In particular, the nanotubes is the most unique candidate for study, because the details of their structural morphology remain unknown, while the rest (i.e. nanowires, nanoribbons, nanowhiskers), are all bulk-like either in crystalline or amorphous phase[54, 55]. Therefore, one of the alternatives to resort to these problems will be theory and simulation, and the reliable theoretical tools which allow for a proper description of its chemistry, will be the *first-principles* (DFT) calculations.

We will discuss the basic properties of boron nanotubes (BNTs) based on DFT calculations. Specifically, we will try to establish such a basic connection between $2D$ boron sheets and $1D$ boron nanotubes, based on our results[7, 8, 9], together with some related work in the previous studies[197, 198, 199]. The presentation of this chapter is organized follows: In Section 5.2, a brief mathematical decsription of the model of BNTs will be given, followed by the computation methodology in Sec 5.3. The results and discussion covering several different aspects will be given in the following section, such as structural stability and energetics of both pristine and crystalline bundles of boron nanotubes, chemical bonding, electronic, mechanical and thermodynamical properties. A summary of these results will be presented in Section 5.5.

## 5.2 Mathematical Description of An Ideal Boron Nanotube

As mentioned in Sec. 4.1, the structure of BNTs is strongly related to the configurations of the corresponding $2D$ boron sheet. There are three competing boron sheets which can be wrapped to form a nanotube, similar to the construction of carbon nanotubes from a wrapped graphene sheet[196]. Therefore, in general, analogous to the case of carbon nanotubes (CNTs), the wrapping in BNTs can be described by a chiral vector (wrapping vector) $W = na + mb$, denoted as (n,m), where n and m are integers. The BNTs can form a 'zigzag', 'armchair' and 'chiral' structures, depending upon the values of n and m[196].

Among the three possible candidates of boron sheets (Figure 5.1): the idealized {1212}, buckled {1212} and the reconstructed {1221}, the energetically least stable idealized {1212}. The {1212} sheet consists of six equal coordinated ($Z = 6$) boron atoms in a perfect triangular lattice which is a common structural basis of among the boron polymorphs, is the earliest proposed candidate[206]. Based on a generalization of the Euler-Poincaré formula for a cyclinder[206]: $P - C + F = 0$, where $P$ is the number of vertices, $C$ is the number of contacts, and $F$ is the number of faces, an ideal boron nanotubes (BNTs) can be constructed by the appropriate 'wrapping' of an 'idealized' triangular boron sheet (i.e. idealized {1212} boron sheet).

Later, as the more stable buckled {1212} was found from DFT results[9, 197, 198, 199]
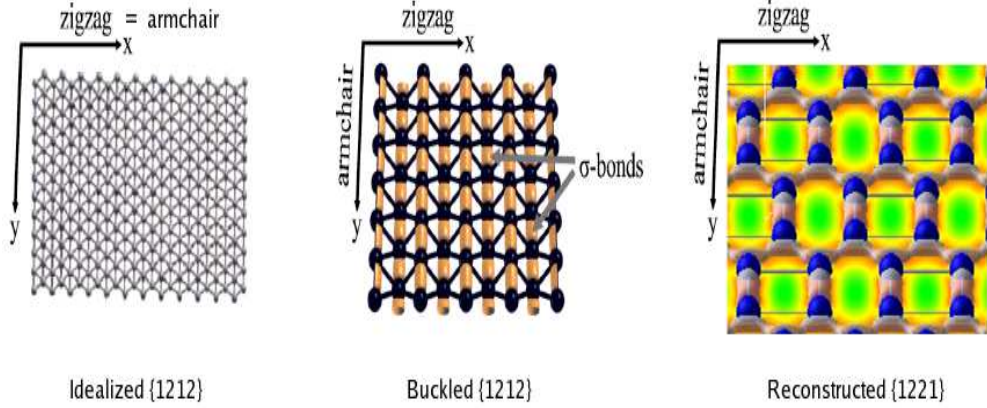
**Figure 5.1:** Three most promising candidates of $2D$ boron sheets to form boron nanotubes in our study, namely: idealized {1212}, buckled {1212}, and reconstructed {1221}.

through the 'breaking' of symmtery of the idealized {1212} boron sheet, a more proper classification scheme for the mathematical description of BNTs have been proposed[197, 198, 199]. By following the mathematical description proposed by Kunstmann *et al.*[199], the basic tubular structure of a BNT is characterized by a wrapping vector, $W$. From a rectangular area of a boron sheet (Figure 5.2), a BNT with its radius $R$ can be defined as $\frac{|W|}{2\pi}$, which $W$ will become the circumference of the nanotube when the boron sheet is rolled up. Instead of triangular[197] and honeycomb-derived[198] primitive cells (Figure 5.2), we therefore adopt the rectangular primitive cell which is shown to be more universal by including BNTs constructed from both idealized and buckled {1212} boron sheets. Accordingly, the wrapping vector $W^r$ is defined as[199]

$$W^r = (k, l) = k\mathbf{a_1^r} + l\mathbf{a_2^r} \tag{5.1}$$

122

with $k$, $l$ being integers, and $a_1^r = A(1,0)$ and $a_2^r = B(0,1)$ are the primitive vectors

of the rectangular lattice, where the $A$ and $B$ are the lattice constants shown in Sec

5.3.
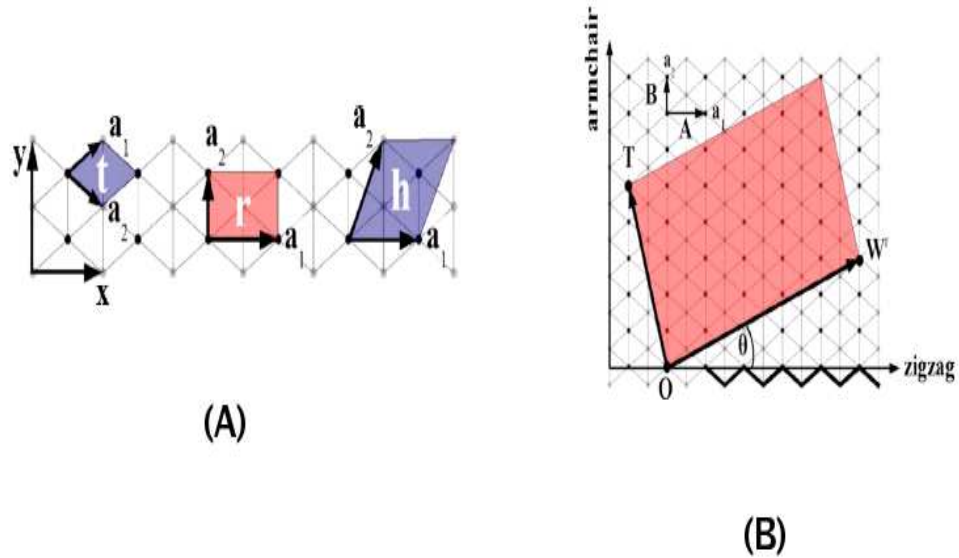


**Figure 5.2:** (A) The triangular (t), the rectangular (r), and the honeycomb-derived (h) primitive cells that are used to characterize boron nanotubes. They contain one, two, and three atoms, respectively. Only the rectangular cell may properly describe the geometrical features of buckled {1212} boron sheet. The puckering of the boron sheet is indicated by black and grey atoms in the background. (B) The geometrical construction of an ideal boron nanotube from a boron sheet: red (gray) area is cut and rolled up such that $W^T$ will become the circumference of the nanotube. $O$ is the origin, $W^T$ is the wrapping vector, $T$ is the translation vector, $\theta$ is the chiral angle measured with respect to the zigzag direction, $a_{1,2}$ are the primitive vectors of the underlying rectangular lattice, and $A$ and $B$ are the lattice constants. The puckering of the boron sheet is indicated by black and gray atoms in the background. Zigzag and armchair directions are perpendicular to each other[199].

In order to advoid confusion, here the $a_1^r$ and $a_2^r$ can be defined according to the local

bonding features of buckled {1212} boron sheet. The armchair direction (i.e. $a_2^r$) is

defined corresponding to the $\sigma$ bond direction, while the zigzag direction (i.e. $a_1^r$) is associated with the delocalized bonds along the direction of triangular lattice within the boron sheet. Following the analogy to the Dresselhaus construction for carbon nanotubes[196], we define the chiral angle $\theta$ as the angle between the vectors $W^r$ and $a_1^r$, i.e. $\theta$ is measured with respect to the zigzag direction coinciding with $a^r$. With this respect, the zigzag BNTs will correspond to $\theta = 0^o$ with $(k, l) = (k, 0)$, while the armchair BNTs will correspond to $\theta = 90^o$ and $(k, l) = (0, l)$. Similarly, the BNTs which constructed from the idealized {1212} (i.e. the perfect triangular boron sheet in Figure 5.1), both zigzag and armchair BNTs are found to be equivalent, as the $a_1^r$ = $a_2^r$. While for the reconstructed {1221} boron sheet (Figure 5.1), the distinction among the corresponding zigzag and armchair BNTs will remain the same, and its classification can be defined according to the zigzag, $a_1^r$ and armchair direction, $a_2^r$ from its delocalized bonds and local $\sigma$ bonds lying on the separated direction, within the 'triangular-square-triangular' lattice.

## 5.3    Computational Methods

*First principles* calculations were performed on the crystalline bundles of SWBNTs and their corresponding pristine SWBNTs in the framework of all-electron density functional theory (DFT) with the Perdew-Wang 91 exchange-correlation functional form[200]. The periodic linear combination of atomic orbitals (LCAO) approximation as embedded in the CRYSTAL03[207] program was employed. A linear combination of Gaussian-type orbitals (GTOs) was used to construct a localized atomic basis from which Bloch functions were constructed by a further linear combination with planewave phase factors.

A split-valence basis set with polarization functions (i.e. 6-31G(d,p)) was considered for boron atoms whose exponents of the most diffuse $sp$ and $d$-shells were reoptimized. The optimized diffuse Gaussian exponents are below*:

Standard basis: 6-31G(d,p)

S 6 1.00

0.2068882250E+04 0.1866274590E-02

0.3106495700E+03 0.1425148170E-01

0.7068303300E+02 0.6955161850E-01

0.1986108030E+02 0.2325729330E+00

---

*The basis set given is following the format used by the Gaussian98 and Crystal03 program. The $1^{st}$ column specify the exponents, while the $2^{nd}$ ($2^{nd}$ and $3^{rd}$ column for $SP$ shells) column specify the contraction coefficients of the Contracted Gaussian Type Orbitals (CGTOs). The $SP$ shells share the same exponents for $s$ and $p$ functions.

0.6299304840E+01 0.4670787120E+00

0.2127026970E+01 0.3634314400E+00

SP 3 1.00

0.4727971071E+01 -0.1303937970E+00 0.7459757990E-01

0.1190337736E+01 -0.1307889510E+00 0.3078466770E+00

0.3594116829E+00 0.1130944480E+01 0.7434568340E+00

SP 1 1.00

0.1600000000E+00 0.1000000000E+01 0.1000000000E+01

D 1 1.00

0.6000000000E+00 0.1000000000E+01

Here the accuracy of the optimized basis sets on the outer diffuse $SP$ and $D$ orbitals are optimized within the convergence of $\sim$ 1 mili Hartree. The accuracy on this optimized basis sets is around 0.03 eV/atom.

The Brillouin zone was sampled using a $8 \times 8 \times 8$ Monkhorst-Pack grid for the integration in the reciprocal space. The total energy tolerance with $10^{-7}$ Hartree, and eigenvalue tolerance with $10^{-6}$ Hartree in the iterative solution of the Kohn-Sham equations were set. Additional details of the calculations can be found from us. The reliability and accuracy of the computational model employed was successfully tested on the well-studied boron crystalline solid, $\alpha$-$B_{12}$, whose structural and electronic properties[31, 33, 202, 203] were reproduced by the modeling elements employed in the present study in Table 5.1.

**Table 5.1:** $\alpha$-$B_{12}$ boron: binding energy (BE (eV/atom)) and geometrical parameters. $d_{intra}$ is the intra-icosahedral bond length, $d_{inter}$ is the inter-icosahedral, and $a$ is the lattice parameter. The unit is Å. Note: The calculated lattice constant of $\alpha$-$B_{12}$ is 5.05 Å as compared to the experimental value of 5.06 Å[202, 203]. The calculated indirect band gap 1.64 eV agrees well with the previous theoretical[30, 33, 208] (within range of 1.43 - 1.72 eV) and experimental[209] ($\sim$ 1.9 eV) values

| Model | | $\alpha$-$B_{12}$ | | | |
|---|---|---|---|---|---|
| | | BE | $d_{intra}$ | $d_{inter}$ | $a$ |
| GGA | [This Work] | 6.18 | 1.74, 1.78, 1.80 | 1.67, 2.01 | 5.05 |
| | [Ref. 3] | 6.18 | 1.74, 1.77, 1.80 | 1.66, 2.00 | 5.04 |
| | [Ref. 4] | 6.22 | - | - | - |
| | [Ref. 18] | 6.95 | - | 1.67, 1.99 | 4.98 |
| | [Ref. 19] | - | 1.72, 1.76, 1.78 | 1.65, 1.98 | 4.98 |
| LDA | [Ref. 6] | 7.51 | - | - | - |
| | Experiment | 5.81 | - | 1.71, 2.02 | 5.06 |

Additionally, the same set of model parameters were used to get a consistent comparison among previous studies[197, 198, 199] on boron sheets. The boron sheets forming the competing low-lying configurations considered are idealized {1212}, buckled {1212} and reconstructed-{1221} sheet configurations[7, 9, 197, 198, 199]. As shown in Table 5.2, the results of the present study for idealized and buckled {1212} sheet configurations are essentially found to be consistent with the structure models of previous studies[9, 197, 198, 199] indicating the reliability of the model elements of the present study.

**Table 5.2:** Boron Sheet Configurations: Buckled and idealized {1212}, and reconstructed {1221} configurations: binding energy BE (eV/atom) and the bond lengths ($R_{B-B}$).

| Ref. | Model | idealized {1212} | | buckled {1212} | | reconstructed-{1221} | |
|---|---|---|---|---|---|---|---|
| | | BE | $R_{B-B}$ (Å) | BE | $R_{B-B}$ (Å) | BE | $R_{B-B}$ (Å) |
| [This work] | GGA | 5.37 | 1.71 | 5.62 | 1.62, 1.84 | 5.48 | 1.63, 1.69, 2.18 |
| [VASP] (Chapter 4) | LDA | 6.36 | 1.69 | 6.54 | 1.60, 1.83 | 6.33 | 1.62, 1.64, 1.92 |
| | PAW-LDA | 6.39 | 1.70 | 6.57 | 1.60, 1.83 | 6.37 | 1.62, 1.65, 1.97 |
| [VASP] (Chapter 4) | GGA | 5.48 | 1.71 | 5.70 | 1.61, 1.89 | 5.57 | 1.63, 1.66, 2.00 |
| | PAW-GGA | 5.69 | 1.71 | 5.92 | 1.61, 1.88 | 5.78 | 1.63, 1.66, 2.01 |
| [*Ref.*1] | LDA | 6.53 | - | 6.79 | - | - | - |
| [*Ref.*4] | LDA | 6.06 | 1.70 | 6.27 | 1.63, 1.81 | - | - |
| [*Ref.*6] | LDA | 6.76 | 1.69 | 6.94 | 1.60, 1.82 | - | - |
| [*Ref.*4] | GGA | 5.49 | 1.71 | 5.72 | 1.64, 1.82 | - | - |

## 5.4   Results and Discussion

It is well known that some of the interesting properties of carbon nanotubes (CNT) which can be synthesized as pristine nanotubes appear only in the condensed phase[210, 211] in which they tend to form close-packed bundles[211]. Therefore, it is of great interest to understand how boron nanotubes can be assembled into stable form via inter-tubular interactions in the condensed phase, knowing that the chemical bonding in the boron nanotube is quite different from that in the carbon nanotube[7, 8, 199] even in pristine condition.

In a recent theoretical study[199], it was suggested that the strain energy together with inter-tubular interaction of single-wall boron nanotubes are diameter and chirality dependent, in contrast to carbon nanotubes. Following this suggestion, we have considered a specific case of SWBNTs with small diameter to investigate their morphological evolution in the close-packed bundles in the crystalline phase. Specifically in the following chapters, we will study bonding, stability, thermodynamic, and electronic properties of SWBNT bundles using the state-of-the-art density functional theory. The calculated results show that the subtle interplay between two-centered $\sigma$ and three-centered $\pi$ bonds found in the idealized and reconstructed boron sheet configurations yields a different morphological features in the corresponding bundles of both zigzag and armchair chiralities, and the presence of a relatively stronger inter-tubular interaction modifies stabilities, structural and electronic properties of SWBNTs of small diameter in the crystalline bundles.

### 5.4.1 Structural Stability and Energetics

#### 5.4.1.1 Pristine SWBNTs

We noted that the local geometric structure of these SWBNTs are different from that of icosahedral clusters based boron solids[14], and the surface-passivated $1D$ boron nanowires[54, 55]. In this respect, the pristine SWBNTs can be characterized by one lattice parameter: $c$, which represents the $1D$ periodicity along the tubular axis, together with its corresponding symmetry which defined by its rod group (i.e. the subset of the 230 space group) within CRYSTAL code. Analogous to conventional definition of crystallographic cell, each unit cell of the SWBNTs can well-represented by distinct numbers of crystallographically non-equivalent $B$ atoms, which depends on its structural configuration and chirality of the nanotubes as we mentioned in Sec. 5.2.

For the small radii SWBNTs, we have considered several possible configurations, shown in Fig. 5.3, of pristine SWBNTs, namely: the $(6,0)$ zigzag Type-I, $(0,6)$ armchair Type-II, $(0,6)$ armchair type III, $(0,6)$ zigzag type IV, and $sp^3$-like tetragonal SWBNT for electronic structure calculations. Here, we have used the convention established for CNTs[196, 212] as we mentioned in Sec. 5.2 to describe SWBNTs chiralities derived from the corresponding $2D$ sheet configurations.

It must be pointed out that all the prototypes of single-walled boron nanotubes (SWB-NTs) proposed in our current study have not been observed experimentally. However,
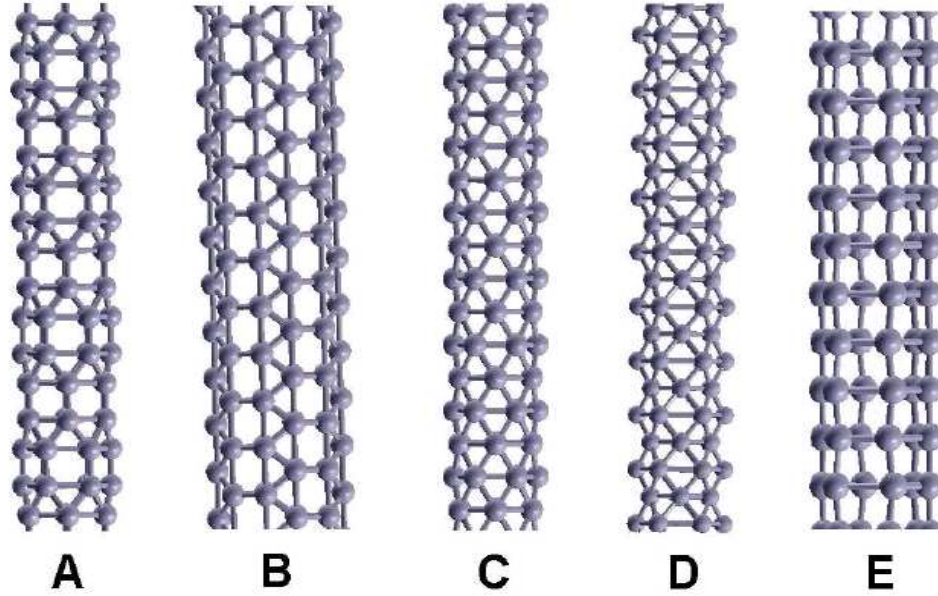
**Figure 5.3:** The possible configurations of pristine single-wall boron nanotubes which represent the various allotropes of elemental boron nanotubes: (A) (6,0) zigzag Type-I, (B) (0,6) armchair Type-II, (C) (0,6) armchair Type-III (also can be referred as (6,0) zigzag Type-III), (D) (0,6) armchair Type-IV, and (E) $sp^3$-like tetragonal SWBNTs.

their relative structural stability can be estimated quite accurately based on the current DFT results. The (6,0) zigzag type I SWBNT (Figure 5.3) can be characterized by a six-fold axis symmetry within the rod group[207] $P6/mmm$. Similarly, the (0,6) armchair type II SWBNT (Figure 5.3) is associated with the rod group $P\bar{3}1m$ and $D_{3d}^1$ symmetry. Both of these SWBNTs can be constructed from the reconstructed {1221} boron sheet[9].

For the triangular-lattice based idealized and buckled {1212} boron sheet derived SWBNTs, the structure model with well-defined classification schemes has been given recently[199]. For the highly symmetrical configuration of the idealized {1212} boron

sheet in a perfect triangular lattice[7, 9, 197, 198, 199], the $(n, 0)$ zigzag and $(0, m)$ armchair type III (Fig. 5.3) should be an equivalent configurations. However when the puckering is induced to break the symmetry of the idealized {1212} boron sheet[9, 197, 198, 199] to form a buckled {1212} boron sheet, the proper classification scheme is proposed by Kunstmann $et$ $al$[199]. Both type III and type IV SWBNTs belong to the rod group of $P6/mmm$, but are different in terms of the crystallographically non-equivalent $B$ atoms. Note that the diameter of all the tubular configurations considered here is about 4 - 6 Å. Following the suggestion of Kunstmann $et$ $al.$, we do not consider zigzag type IV SWBNT configurations which is less likely to be stable[199].

Besides the $2D$ idealized {1212}, buckled {1212}, and the reconstructed {1221} boron sheets derived SWBNTs, other possible configurations of SWBNTs have been explored, and one of the candidate is the $sp^3$-like tetragonal (Figure 5.3) SWBNT. Resembling the features of elemental single-wall silicon nanotubes (SWSiNT)[213, 214, 215], the $sp^3$-like tetragonal SWBNT (i.e. $P\bar{3}1m$ in rod group) can be visualized as a hypothetical self-assembled stacked hexagonal rings, which favors the $sp^3$-like hybridization after structural and cell relaxation. For the most stable pristine SWBNT in current study, the (6,0) zigzag-type I SWBNT with optimized diameter about 3.96 Åis achieving $\sim$ 90 % of the stability of $\alpha$-$B_{12}$ rhombohedral phase, despite its high curvature strain within the small diameter regime. This value is particularly intriguing, as compared to the SWSiNTs which is merely $\sim$ 82 % of stability for Si bulk in diamond structure in large diameter at approximately 12 Å[216, 217]. Therefore,

we suggest the SWBNTs can be realized and are feasible as other homo-nuclei nanotubes which resemble carbon and silicon (i.e. SWCNTs and SWSiNTs), if certain appropriate growth environment is achieved.

Electronic structure calculations were performed on the tubular configurations optimizing their lattice parameter as well as the internal coordinates at each fixed value of crystallographic unit-cell volume. The calculated results show that all SWBNTs considered are stable, except the (0,6) armchair type IV SWBNT which makes transition to (6,0) armchair type III SWBNT during the optimization process. This is consistent with the fact that puckering of the boron sheet is not favorable in forming a small diameter armchair SWBNT due to its high curvature strain energy. This result agrees well with the earlier studies[197, 199] in predicting a smooth surface for the armchair SWBNTs in small radii regime. Here within these small radii regime, we found that the type-I SWBNT is stable over the type-III by nearly 0.46 eV/atom (Table 5.3). Knowing the fact that inter-tubular interactions are expected to play an important role in determining the stability of the system[199], we therefore carry on our studies of SWBNT bundles based on these two distinct BNTs species.

**Table 5.3:** System, symmetry (space group), number of atoms ($N$-atoms/cell), nanotube's diameter (Å), bond length, $R_{B-B}^{intra}$ (Å), and cohesive energy, $E_{coh}$ (eV/atom) of the pristine single-wall boron nanotubes and nanotubes crystalline bundles. *The diameter of (0,6) armchair Type-IV is given in average value is due to its buckling configuration which derived from $2D$-buckled {1212} boron sheet. However in this case, this nanotube is found to be metastable. *The (0,6) armchair Type-III is found to be equivalent to (6,0) zigzag Type-III for this nanotube configuration, due to the equal coordination of each boron atom in the $2D$ idealized {1212} boron sheet[7, 9]. After the full structural relaxation, the (0,6) armchair Type-IV converged to (0,6) armchair Type-III.

| System | Symmetry (Space Group) | $N$ (atoms/cell) | Diameter (Å) | $R_{B-B}^{intra}$ (Å) | $E_{coh}$ (eV/atom) |
|---|---|---|---|---|---|
| (6,0) zigzag Type-I | $P6/mmm$ | 24 | 3.96 | 1.64,1.67,1.98 | 5.53 |
| (0,6) armchair Type-II | $P\bar{3}1m$ | 24 | 5.57 | 1.64, 1.67, 2.04 | 5.25 |
| (0,6) armchair* Type-III | $P6/mmm$ | 24 | 3.70 | 1.74, 1.85 | 5.07 |
| $sp^3$-like tetragonal | $P31m$ | 12 | 4.17 | 1.61, 1.91, 2.25 | 5.02 |
| (0,6) armchair** Type-IV | $P6/mmm$ | 24 | 4.21 (average) | 1.85, 1.86 | 4.87* |

### 5.4.1.2   Crystalline Bundles

Considering the fact that inter-tubular interactions are expected to play an important role in determining the stability of the SWBNT bundles[199], two distinct morphologies of SWBNT bundles consisting of type I (6,0) zigzag and type III (0,6) armchair SWBNTs with small diameter are considered for electronic structure calculations. The crystalline bundles of SWBNTs were represented by arrays of identical nanotubes arranged in a hexagonal lattice. The tubes are of infinite length and not capped. In a hexagonal unit cell, $a$ is defined as the sum of the diameter of the nanotube and its inter-tubular distance, and $c$ represents the periodicity of a SWBNT along its tubular axis.

Figure 5.4 shows the calculated potential energy surface (i.e. total energy *vs.* volume) of the bundles where the lattice parameters as well as the internal coordinates of the tubular configuration were optimized at the each value of the unit-cell volume on the energy surface. It was followed by the optimization of the tubular configuration without using any symmetry constraint during the optimization. As shown in Fig. 5.4, the sparse configuration on the energy surface is defined as a configuration where a bundle consists of weakly interacting SWBNTs with $R_{B-B}^{inter} \geq 3$ Å. On the other hand, the equilibrium configuration is associated with the lowest total energy of a given type of bundles. The calculated equilibrium volume is 200 and 165 Å$^3$ for type I and type III bundles, with cell density 2.22 and 2.69 $g/cm^3$ respectively. Table 5.3 collects structural and geometrical features of the bundles associated with the sparse and equilibrium configurations on the energy surface shown in Fig. 5.4.
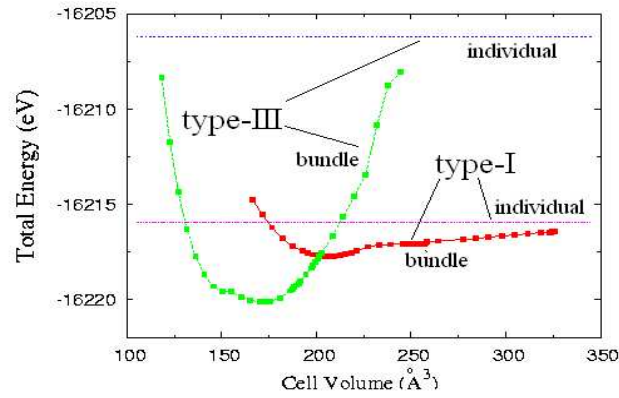
(A)
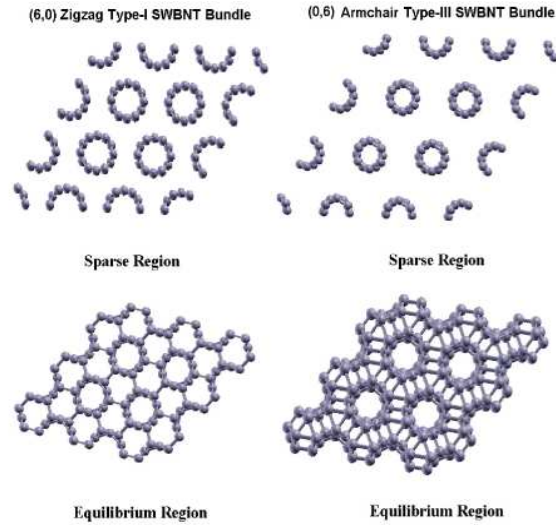


(B)

**Figure 5.4:** (A) The energy surface represented by total energy vs cell volume in different regime, namely the sparse and equilibrium configurations of both type I and type III SWBNTs bundles. In the sparse region, the cell volume is $\geq 240$ Å$^3$ associated with $R_{B-B}^{inter} \geq 3.0$ Å. A straight line represents the total energy of isolated boron nanotubes. (B) A top view of type I and type III crystalline bundles of SWBNTS in the sparse and equilibrium configurations.

There appears to be a cross-over of the stability of bundles as the inter-tubular interaction becomes stronger between SWBNTs with small diameter. As the overall trend,

type I bundles are more stable in the sparse configuration due to their high stability in static energy as pristine nanotubes (Sect. III-A). Whereas type III bundles become more stable in the equilibrium configuration by settling down in a rather compacted, interlinked bundles as shown in Fig 5.4. This fact is reflected in a relatively larger change of the cohesive energy of type III bundles ($\sim$ 0.59 eV/atom) in going from the sparse configuration to the equilibrium configuration (Table 5.3, Fig. 5.4), gaining almost 10 % of cohesive energy relative to $\alpha$-$B_{12}$ solid. For the small diameter SWBNTs, it is noteworthy to point out that type III SWBNT is not energetically preferable relative to type I SWBNT, though a relatively stronger inter-tubular interaction within the bundles is crucial in stabilizing type III bundles over type I bundles. In fact, our prediction is consistent with the results of a previous study[199] predicting the same order of gain in energy ( $\Delta E_{coh} \sim$ 0.30 eV/atom) for a larger diameter (i.e. $\sim$ 6 - 12 Å) armchair SWBNT bundles. Such a large gain in cohesive energy clearly point out to the fact that inter-tubular interaction in the SWBNT bundles is different from that in the carbon nanotube bundles, which are bonded by weak Van der Waals interactions.

**Table 5.4:** Structural parameters and cohesive energy ($E_{coh}$) of the SWBNT bundles. $R_{B-B}^{inter}$ and $R_{B-B}^{intra}$ are inter-tubular and intra-tubular distances, and $V_0$ is the primitive cell volume. $\epsilon^{\alpha-B_{12}}$ is stability of the system relative to the cohesive energy of $\alpha$-$B_{12}$ boron solid.

| System (SWBNT-bundles) | Configuration | space group | lattice $a$, $c$ (Å) | $V_0$ (Å³) | $R_{B-B}^{inter}$ (Å) | $R_{B-B}^{intra}$ (Å) | $E_{coh}$ (eV/atom) | $\epsilon^{\alpha-B_{12}}$ (%) |
|---|---|---|---|---|---|---|---|---|
| (6,0) zigzag | Sparse | $P6/mmm$ | 6.92, 5.93 | 246 | 2.96 | 1.65, 1.98 | 5.51 | 89 |
| Type I | Equilibrium | $P6/mmm$ | 6.21, 5.93 | 198 | 1.94 | 1.63, 1.91 | 5.58 | 90 |
| (0,6) armchair | Sparse | $P6/mmm$ | 7.19, 5.86 | 262 | 3.06 | 1.75, 1.83 | 5.09 | 82 |
| Type III | Equilibrium | $P6/mmm$ | 5.68, 5.86 | 163 | 1.74, 1.98 | 1.65, 1.79, 1.97 | 5.68 | 92 |

## 5.4.2  Chemical Bonding

In general, the bonding features found in SWBNTs are similar to its corresponding $2D$ boron sheet, regardless of the curvature strain acting on these tubes. When all the SWBNTs weakly interact among themselves within the sparse configuration of the crystalline bundles, the individual SWBNTs within the bundles are found share the same bonding features as their corresponding pristine SWBNTs. In type I SWBNT, the chemical bonding is dominated by the localized two-centered ($2c$) $\sigma$ bonds along the tubular direction, whereas the delocalized three-centered ($3c$) $\pi$ bonding features with nearly homogeneous electron distribution describe the bonding in type III SWBNT (Fig 5.5). Similarly, consistent bonding features of these SWBNTs can also be found in $3D$ electron charge density plot based on the planewave basis functions, as we applied in our previous preliminary study[7]. The 'three-centered' bond ($3c$) generally involves two electrons in a molecular orbital (MO) formed by three atomic orbitals (AOs), which renders triangular faces configurations (i.e. a triangular $B - B - B$ unit)[14, 15]. In order to extract this unique feature of bonding in boron nanostructures, we use Mulliken population analysis, together with electronic charge density map for the SWBNTs and crystalline bundles considered.

In the sparse configuration of the crystalline bundles, there is almost no total charge density distribution at the inter-tubular region as shown in Fig 5.6. The total charge density is nearly equivalent to the superposition of charge density of individual pristine nanotubes. For bundles in the equilibrium configuration, we use the Mulliken population analysis to estimate the strength of the intra-tubular and inter-tubular
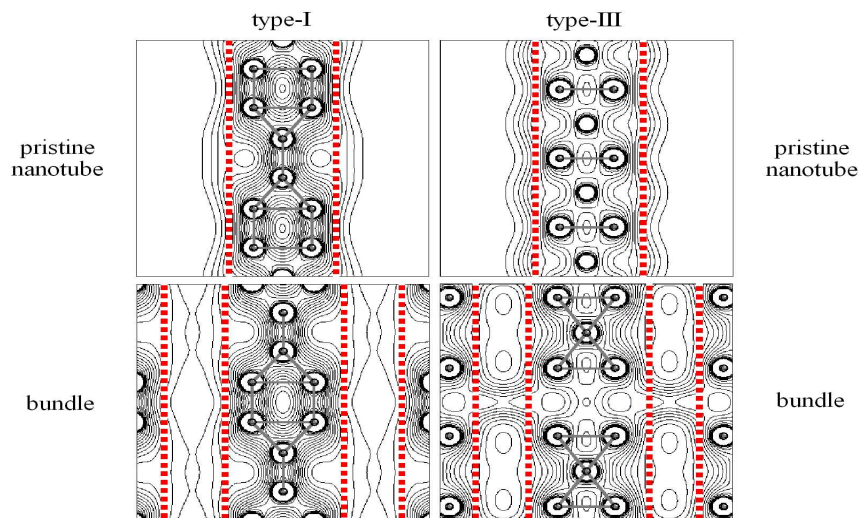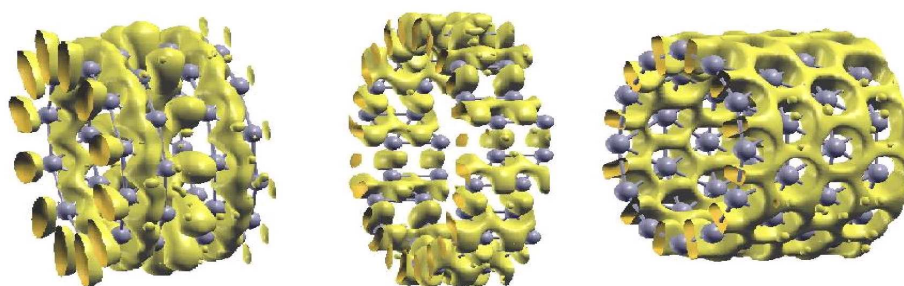
**Figure 5.5:** (A) The side view of the electronic charge density maps on the 2D plane along the tubular axis of pristine SWBNTs and crystalline bundles at the equilibrium configurations. Top: (Left) (6,0) zigzag type I SWBNT, (Right) (0,6) armchair type III SWBNT. Bottom: (Left) (6,0) zigzag type I and (Right) (0,6) armchair type III SWBNTs based crystalline bundles . The red dotted lines represent the outline of the side view of each tubules. (B) The $3D$ charge distribution of the segments of pristine SWBNT: (Left) (6,0) zigzag type I SWBNT, (center) (0,6) armchair type II, (right) (0,6) armchair type III SWBNT.

bonds in terms of the degree of overlap population $b(A^0, B^0)$ in the units of $e$ among the nearest neighbors.

Table 5.4 collects the values of $b(A^0, B^0)$ associated with the atoms in either intra-tubular or inter-tubular bonding regions of the crystalline bundles. In type I bundles, there exists a dominance of the $\sigma$-bonds which interconnect the 'triangle-square-triangle' along the tubular axis over the $\pi$ bonds associated with the boron atoms along the triangular network in the intra-tubular region. The $2c$ bonds in the crystalline bundles, therefore, appear to be as rigid as those in isolated nanotubes.

**Table 5.5:** $b(A^0, B^0)_{intra}$ and $b(A^0, B^0)_{inter}$ are the overlap populations associated with the intra-tubular and inter-tubular bonds, respectively. The $2c$ and $3c$ are referred as 'two-centered' and 'three-centered' bonds respectively. The overlap population among the nearest neighbors is obtained from the Mulliken charge analysis.

| System | | two-centered ($2c$) | | three-centered ($3c$) | |
|---|---|---|---|---|---|
| (pristine SWBNT/bundle) | | $b(A^0, B^0)_{intra}$, $(e)$ | $b(A^0, B^0)_{inter}$, $(e)$ | $b(A^0, B^0)_{intra}$, $(e)$ | $b(A^0, B^0)_{inter}$, $(e)$ |
| (6,0) zigzag | pristine nanotube | 0.66 | - | 0.34 | - |
| Type I | bundle | 0.68 | 0.33 | 0.35 | - |
| (0,6) armchair | pristine nanotube | - | - | 0.41 | - |
| Type III | bundle | 0.32 | 0.52 | 0.35 | 0.36 |

For type III bundles, the inter-tubular interaction is described by both $2c$ and $3c$ bonds; both having significant strength. Interestingly, the strength of $3c$ bonds is nearly the same in both inter- and intra-tubular regions (Table 5.4). Furthermore, a presence of the 'buckling' induced two-centered $\sigma$-bonds in the intra-tubular and inter-tubular region of the bundles is confirmed, though they were not present in the isolated type III SWBNTs. This is also reflected in a rather large value of about 0.92 of the degree of polygonization (i.e. $\eta = r_s/r_l$, where $r_s$ and $r_l$ are the short and the long radial dimensions of the nanotube cross section, respectively) of SWBNTS in type III bundles. [†]

The difference between the inter-tube interactions between type I and type III bundles is mainly due to differences in their bonding features in the respective pristine SWB-NTs. In type I SWBNT, the bonding is dominated by two-centered ($2c$) $\sigma$ bonds with $b(A^0, B^0) = 0.66$ $e$, whereas the bonding features in type III SWBNTs are dominated by three-centered ($3c$) $\pi$ bonds with nearly homogeneous electron distribution with $b(A^0, B^0) = 0.41$ $e$ (i.e. Table 5.4 and Fig. 5.6). When we bring the small-diameter SWBNTs together to form a bundle, the rigid two-centered $\sigma$ bonds along tubule axial direction in type I SWBNTs can not easily be deformed, leading to a weaker (i.e. $b(A^0, B^0) = 0.33$ $e$ from Table 5.4) inter-tube interactions in type I bundles. On the other hand for type III SWBNTs bundle, a relatively weaker two-centered $\sigma$ bonds lies along the circumferential direction are found easily distorted to yield a stronger

---

[†]Although SWBNTs assume a circular cross section in an isolated state, they are not likely to remain in the circular shape in bundles where the inter-tubular interactions are not negligible. Quantitatively, the radial deformation can be expressed in terms of the degree of 'polygonization', $\eta = r_s/r_l$, where $r_s$ and $r_l$ are the short and the long radial dimensions of the nanotube cross section, respectively. When the value of $\eta$ is 1, a perfect circular cross section of a cylindrical nanotube is expected.
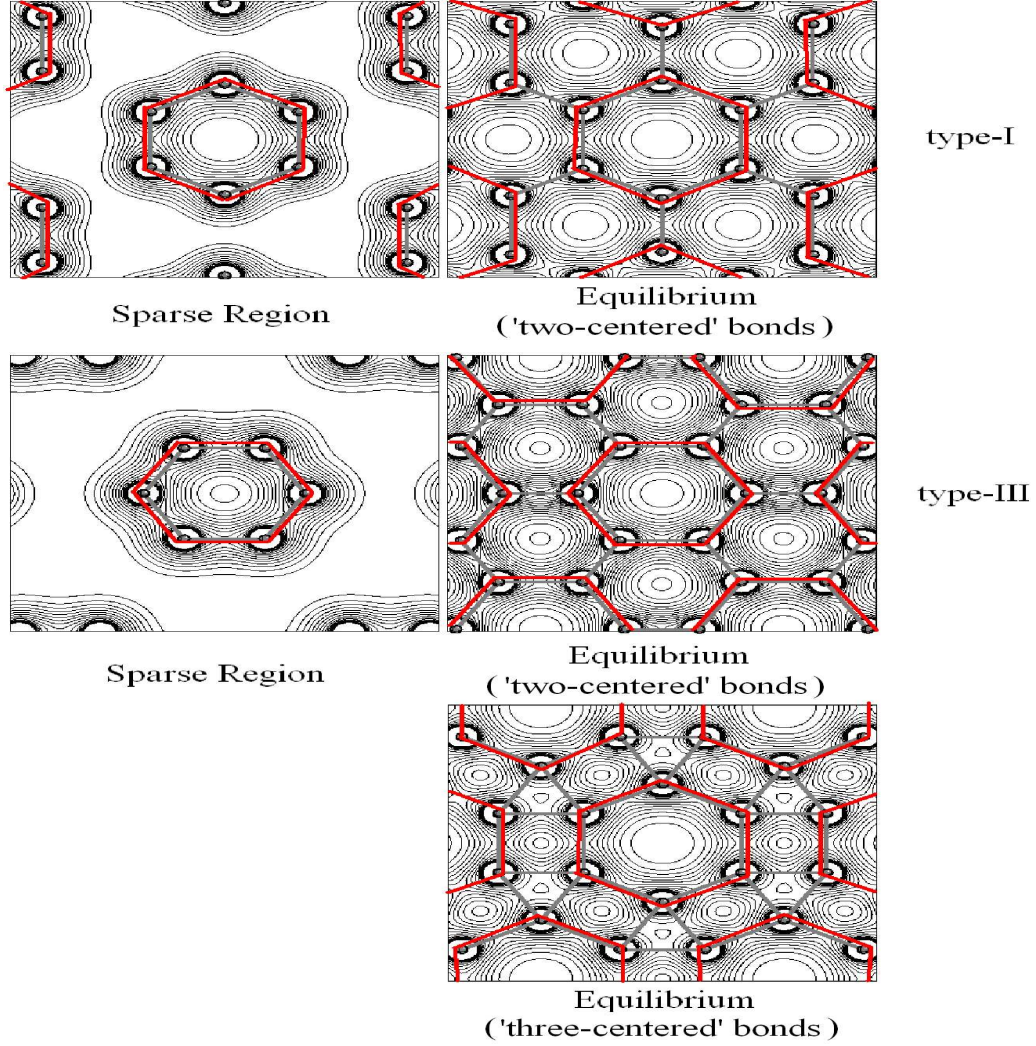
**Figure 5.6:** A top view of the electronic charge density maps on the 2D plane of type I and type III SWBNTs crystalline bundles in the sparse and equilibrium configurations. (Top): type I bundles. (Bottom): type III bundles. The red colored hexagonal box in each figure represents the outline of the top view of SWBNT within the bundle. For type III SWBNTs crystalline bundles in equilibrium configuration, the electronic charge density maps are showing 'two-centered' and 'three-centered' bonds, respectively.

inter-tubular $2c$ and $3c$ bonds (i.e. $b(A^0, B^0) = 0.52$ and $0.36\ e$ respectively). This unique bonding character is consistent with the previous study [199] suggesting that distortion of the circumferential $\sigma$ bonds is expected to enhance the surface chemical reactivity attributed mainly to the unsaturated dangling bonds on the tubular surface

for type III SWBNTs.

Our results, therefore, suggest that a larger gain in the cohesive energy of type III bundles in going from the sparse to equilibrium region (Fig 5.6) can be attributed to the presence of a stronger interaction in the inter-tubular region of type III bundles. The buckling of SWBNTs in bundles due to the presence of the flexible or "softer" $3c$ bonds formed on the tubular surface facilitates the release of the strain of the tubular configurations in bundles. Specifically, the enhanced stability of this system (i.e. $\Delta E_{coh} = 0.59$ eV/atom for small radii SWBNT bundles *vs.* $\Delta E_{coh} \sim 0.30$ eV/atom for large radii SWBNTs bundle[199]) via stronger inter-tubular interactions, can be attibuted to an enhanced reactivity of small diameter armchair type III SWBNTs as hypothesized in the recent study[199].

### 5.4.3 Electronic Properties

All the pristine SWBNTs in current study are found to be metallic. The electronic band dispersion of SWBNTs studied in this work are found to be consistent with our predictions in previous work, which based on *first-principles* pseudopotential planewaves method[7], specifically on Type-I, II and III pristine SWBNTs. For all $1D$ infinite SWBNTs which is periodically repeated along $x$-axis in tubular direction, all the band dispersions (Fig. 5.7) are plotted within the $\pm 3$ eV range of Fermi level at $(\frac{1}{2}00)$ relative to $\Gamma$ in the Brillouin zone. Specifically, the the symmetry path $(000)$-$(\frac{1}{2}00)$ defined as $\Gamma$-$A$ in Brillouin zone, is equivalent to $(000)$-$(00\frac{1}{2})$ (i.e. $\Gamma$-$A$)

in hexagonal bravais lattice, along $z$-axis in tubular direction of their corresponding

crystalline bundles.
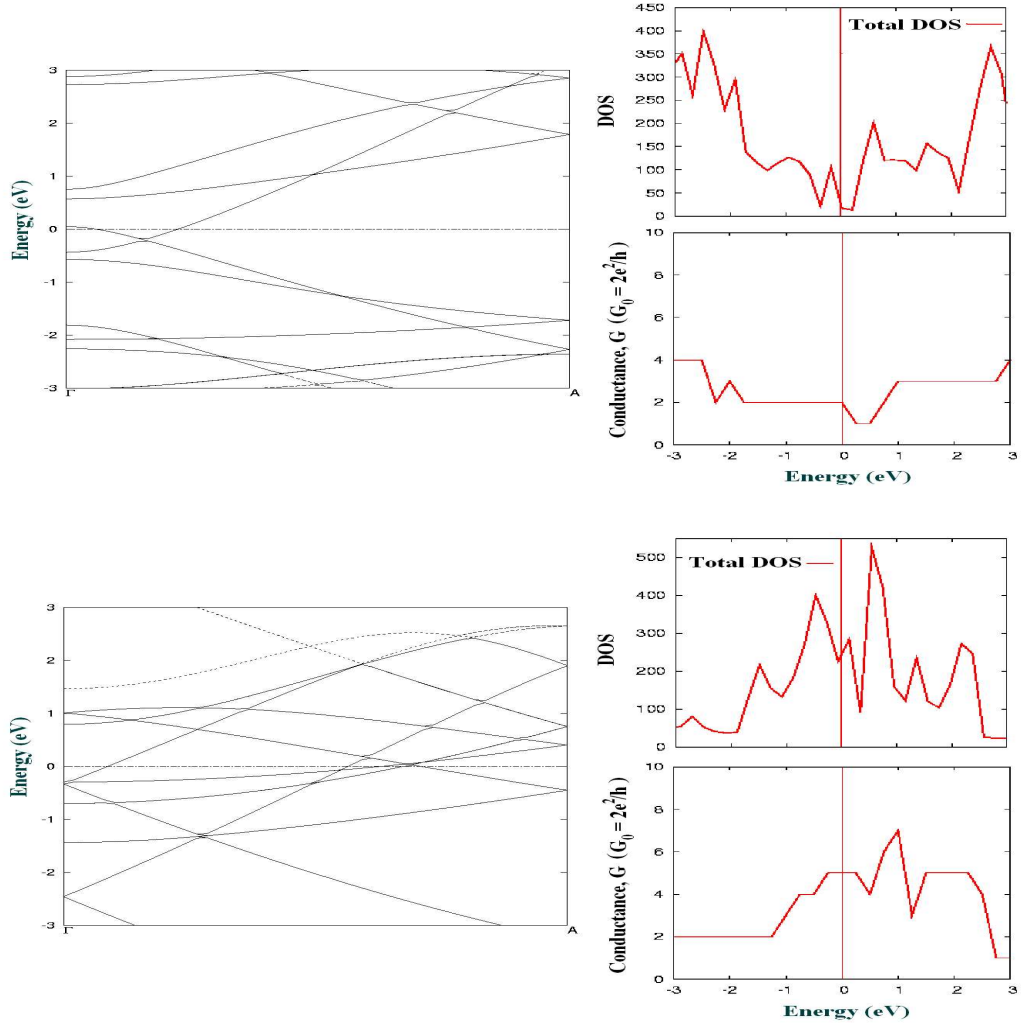


**Figure 5.7:** The band structure along tubular axis associated with the $\Gamma$-$A$ symmetry line, together with total density of states (DOS) and intrinsic quantum conductance plot of both type I SWBNT (top), and type III SWBNT (bottom). All plots are plotted within the range of $\pm$ 3 eV around Fermi level $E_f$, with $E_f$ aligned at zero.

The crystalline SWBNT bundles show metallic features, similar to the pristine boron

nanotubes regardless of composition and chirality. This in contrast to the case of

carbon nanotubes where chirality determines the electronic properties to be metallic or semiconducting. It is to be noted here that the elemental boron nanowires exhibit the semiconducting features[54]. The difference between the electronic properties of bundles and nanowires can be attributed to the distinct local geometric structures of SWBNTs as compared to the $B_{12}$ icosahedral clusters based nanowires.

The dispersion of the bands associated with the crystalline bundles in the Brillouin zone response to the degree of inter-tubular coupling, as expected. It is important to note that the number of the available states near Fermi energy can affect the electron transport properties significantly, either in macroscopic and mesoscopic systems[218]. Accordingly, in the sparse configuration, the band diagram and DOS of the crystalline bundle can be well-represented by that of a pristine SWBNT. As the inter-tubular interaction becomes dominant, multiple bands associated with intra-tubular and inter-tubular bonds cross at the Fermi level in type I bundles (Fig. 5.8).

Considering the ballistic transport[196] consisting of single electron conduction with no phase and momentum relaxation, the intrinsic quantum conductances of a nanotube can be extracted from its band structure. Therefore, the conductance $G$ is given by Landauer formula[196]: $G = \frac{2e^2}{h} MT \equiv \frac{2e2}{h} \sum_{ij}^{M} |t_{ij}|^2$, where $T$ is the transmission probability for a channel, and is given by the sum of transmission probability from $i$-th to $j$-th channel, $|t_{ij}|^2$. Assuming that $T$ is constant near the Fermi energy with no electron scattering, the quantized conductance $G$ is proportional to $M$, which defines the number of channels available for coherent electron propagation in the nanotube.
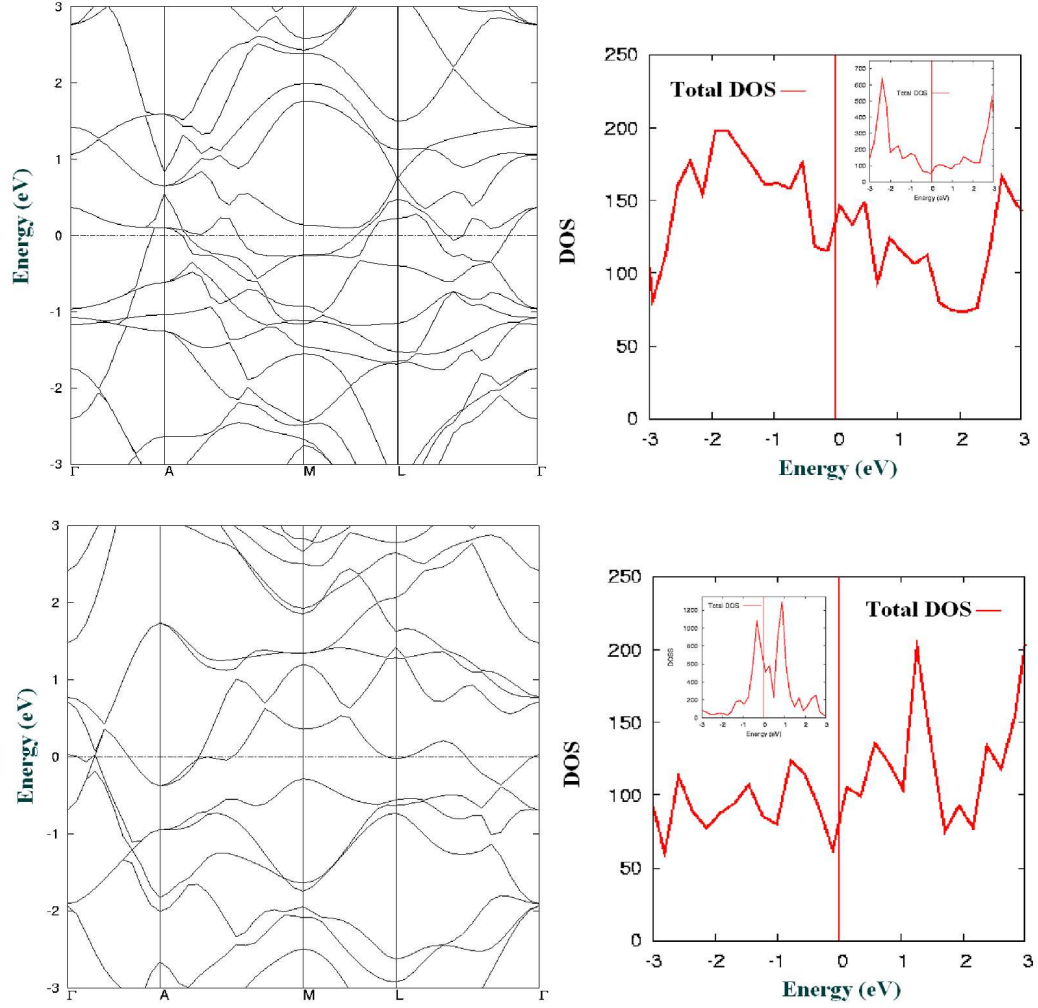
**Figure 5.8:** The band structure along the $\Gamma$-$A$-$M$-$L$-$\Gamma$ symmetry line, together with total density of states (DOS) plot of both type I SWBNT (top), and typeIII SWBNT bundles (bottom). All plots are plotted within the range of $\pm$ 3 eV around Fermi level $E_f$, with $E_f$ aligned at zero. The inset in the figures of DOS shown are the DOS of sparse crystalline bundles of both configurations, which mimic the DOS of pristine SWBNTs in both cases.

Accordingly, the ballistic conductance $G$ of each SWBNT considered in the present study can be determined by the number of bands $M$ crossing the Fermi level defined as $G = MG_0$, where $G_0 = \frac{2e^2}{h}$. Thus, in the ballistic limit, the conductance of metallic type I SWBNT[8] is $2G_0$, similar to that associated with the metallic SWCNTs, and

our previous findings based on pseudopotential planewaves calculations[7]. A higher value of conductance of $5G_0$ associated with type III SWBNTs can be attributed to the valence electrons of boron which are shared uniformly forming a delocalized $3c$-bonds, thereby enhancing the probability of electron conduction in the axial direction.

By taking into account of the presence of neighboring nanotubes in a SWBNT bundle, the intrinsic conductance in the 'bulk-like' crystalline bundles is expected to occur along the tubule axial direction (i.e. along $\Gamma$-$A$), similar to that in the corresponding pristine nanotube. Here, the conductance of type I and type III bundles are found to be $4G_0$ and $3G_0$, respectively. In type I bundles, the enhanced conductance with four conducting channels $\sim 4G_0$ along the tubular direction are attributed to two partially occupied degenerate inter-tubular $\sigma$ and $\pi$-like conduction bands. While the three conducting channels of type III correspond to partially occupied $p$ type non-bonded orbitals crossing the Fermi level. It is also important to note that the intrinsic conductance of a system is purely based on the number of the available states crossing the Fermi level[218], and not necessarily proportional to the strength of interaction. In contrast to type I bundle, the strong inter-tubular $2c$ and $3c$ bonds found in type III bundle are mostly located in the occupied valence bands below Fermi level making no contribution to the intrinsic conductance.

## 5.4.4 Mechanical Properties

### 5.4.4.1 Pristine SWBNTs

Analogous to SWCNTs, we assume all the mechanical properties of SWBNTs can be derived from continuum model. Based on the assumptions of isotropic and homogeneous behavior of the materials within the framework of conventional *linear elastic solid model*, several important elastic constants of SWBNTs, such as: $Y$ (Young's modulus or modulus of elasticity), $\nu$ (Poisson ratio), and $B$ (bulk modulus or modulus of compression) can be predicted through a constitutive stress-strain relations within a set of dual independent elastic constants (i.e. $(Y, \nu)$)[219]. By varying the crystalline lattice constant of a nanotube, the Poisson ratio $\nu$ defined as a ratio of lateral strain and axial strain as defined[219, 220]:

$$\nu = \frac{-1}{\epsilon} \frac{R - R_{eq}}{R_{eq}} \tag{5.2}$$

the $\epsilon$ is the axial strain, $R_{eq}$ is the equilibrium nanotube radius, $R$ is nanotube radius at strain $\epsilon$, is obtained by the variation of the radius of SWBNT resulting from longitudinal deformations along the tubular axis based on CRYSTAL03 result. We find in all cases the Poisson's ratio is positive, namely an elongation of the nanotube reduces its diameter. For the both SWBNTs which rolled by $2D$ reconstructed {1221} boron sheet, (6,0) zigzag type-I SWBNT has $\nu = 0.14$, and (0,6) armchair type-II SWBNT has $\nu = 0.10$. While the (6,0) zigzag type-III SWBNT (i.e. also euivalent to

(0,6) armchair type-III SWBNT) which rolled by $2D$ idealized {1212} boron sheet, the $\nu$ is 0.17, and is close to the values obtained by Evans. et. al. for (7,0) and (8,0) which is 0.2 and 0.1 respectively[197]. All the $\nu$ obtained in current study for elemental SWBNTs are found to be smaller than SWCNTs, BN, and $B_xC_yN_z$ composite single-wall nanotubes[220, 221, 222], which are distributed in the range of 0.23 - 0.30.

Regarding to the other important mechanical characteristics of nanotubes, the modulus of elasticity or Young's modulus, its conventional definition[219, 220] is:

$$Y = \frac{1}{V_0}\frac{\partial^2 E}{\partial \epsilon^2}|_{\epsilon=0} \tag{5.3}$$

where $V_0$ is the equilibrium volume, and $E$ is the total energy of the system. However, in the case of singl-wall nanotubes, the walls of our SWBNTs are only a single atom thick, therefore it is rather controversial to define the nanotube volume, by adopting an *ad hoc* convention to define the nanotube shell thickness for a *hollow* cyclinder. In order to have a better justification on this elastic properties, we adopted a 'modified' Young's modulus $Y_s$, which is independent of any shell thickness:[220].

$$Y_s = \frac{1}{S_0}\frac{\partial^2 E}{\partial \epsilon^2}|_{\epsilon=0} \tag{5.4}$$

with $S_0$ is the surface defined by the tube at equilibrium. Within this definition, the value of the Young modulus for a given convention value $\delta R$ is given by $Y = \frac{Y_s}{\delta R}$, and

we can define $V_0$ for a *hollow* cyclinder as $2\pi LR\delta R$, where $L$ is the length, $R$ is the radius, and $\delta R$ is the shell thickness. By using the polynomial fitting, the calculated $Y_s$ for the (6,0) zigzag Type-I SWBNT is predicted to be 0.15 TPa nm, while for (0,6) armchair Type-II tube which rolled into different chiral angle, the $Y_s$ is merely 0.03 TPa nm, significantly reduced in magnitude due to the curvature strain acting on the $\sigma$-bond 'bent' along the tube circumference, in contrast to the (6,0) zigzag type-I which $\sigma$-bond is along the tubular axis. In this case, the (0,6) armchair type-III SWBNT which uniformly governed by delocalized $3c$ bonds is found with $Y_s = 0.04$ TPa nm, close to (0,6) armchair Type-II nanotube. This suggests that the mechanical properties of SWBNTs crucially depends on its variations of chirality, due to its anisotropic and mixed covalent bonds (i.e. $2c$ and $3c$) on the nanotubes, unlike carbon nanotubes which are bounded in uniform $sp^2$ bonds[196, 220, 221]. In order to have a better justification of the predicted values of $Y_s$ given with the conventional Young's modulus, $Y$ available in experiments on bulks and other nanotubes, we further predict the 'actual' Young's modulus (i.e. $Y = \frac{Y_s}{\delta R}$ as given). By adopting the convention $\delta R$ to be 0.20 nm as an approximation, we found the Young's modulus of SWBNTs being studied here, namely type-I, II and III are 0.75, 0.15 and 0.2 TPa respectively, generally smaller than $C$, $BN$, $BC_3$ and $BC_2N$ nanotubes which typically fall in the range of $Y \sim 0.78 - 1.10$ TPa[220, 221, 223].

In the simplest case, assuming these isotropic nanotubes subjected to hydrostatic pressure (i.e. under uniform normal stress with all shear stress to be zero), the state

of stress for this case can be given by[219]:

$$\sigma_{ij} = \begin{pmatrix} -p & 0 & 0 \\ 0 & -p & 0 \\ 0 & 0 & -p \end{pmatrix} = -p\delta_{ij} \qquad (5.5)$$

with the isotropic state of stress and the strains follows from Hooke's law defined as:

$$\varepsilon_{ij} = \begin{pmatrix} -\frac{1-2\nu}{Y}p & 0 & 0 \\ 0 & -\frac{1-2\nu}{Y}p & 0 \\ 0 & 0 & -\frac{1-2\nu}{Y}p \end{pmatrix} \qquad (5.6)$$

Thus, by calculating the change in nanotube volume from strain $\varepsilon_{kk}$, the elastic constant which could be referred to as the volumetric stiffness of the nanotube, can be represented by the bulk modulus $B$ (i.e. ratio of hydrostatic pressure to the relative volume change) shown as below:

$$B = \frac{Y}{3(1 - 2\nu)} \qquad (5.7)$$

Hence, by using the values of $Y$ and $\nu$ obtained from previous under this approximation, the bulk modulus $B$ for (6,0) zigzag Type-I, (6,0) armchair type-II, and (0,6) armchair type-III SWBNTs is predicted to be 347.2, 62.5 and 101 GPa respectively. Similar to the Young's modulus, the bulk modulus of these 3 SWBNTs show distinct variation depend on their configurations and chiralities, especially when compared

153

to SWCNTs. In this case, all carbon nanotubes are predicted to have $B$ within the range of $\sim$ 130 - 260 GPa regardless of chiralities within the comparable diameters range[221, 224, 225, 226].

In addition, in order to better account for the distinct geometrical and bonding features of these SWBNTs when response to the applied pressure in real case[227], the geometrical part of the pressure dependence from the cyclindrical shape of nanotubes, needed to be addressed. Therefore, instead of assuming uniform isotropic stress and strain in all components as we mentioned previously, different strain components in axial, tangential, and radial directions are needed to be properly taken into account. Within the continuum model[225, 227], we approximate each SWBNT as a rolled up hollow cyclinder with finite wall thickness made out of their corresponding boron sheet. Then, we can define the axial $M_z^e$ and radial $M_\theta^e$ linear moduli as below:

$$M_z^e \; = \; \frac{YA}{(1 - 2\nu)} \tag{5.8}$$

$$M_\theta^e \; = \; M_r^e \; = \; \frac{YA}{(1 - 2\nu)} \left( 1 + \frac{(1 + \nu)R_i^2}{(1 - 2\nu)r^2} \right)^{-1} \tag{5.9}$$

where $A = \frac{R_o^2 - R_i^2}{R_o^2}$, $Y$ is Young's modulus, $\nu$ is Poisson's ratio, $r$ is the SWBNT radius, and $R_i$ and $R_o$ are inner and outer radii of the cyclinder, which can be given by subtracting and adding half of the wall-to-wall distance between the tubes in bundles (e.g. we take 2 Å in current study based on Table 5.4). Accordingly, all

154

the calculated values of axial and radial linear moduli for SWBNTs studied in this work are summarized in Table 5.4, analogous to similar size of carbon nanotube. Inspite of the big difference in wall-to-wall distance among SWBNT ($\sim$ 2.0 Å at covalent bonded regime) and SWCNT ($\sim$ 3.3 Å at vdW regime), both (6,0) Type-I SWBNT and SWCNT (i.e. (6,6),(10,0) and (8,4) in Ref.[225]), show the highly unaxial structure of the nanotube yields a higher linear compressibility in the radial than in the axial direction. In contrast, the (6,0) Type-III SWBNT which possess a rather similar moduli in both radial and axial direction ($\sim$ 27% difference), might attributed to its delocalized $3c$ bonds which cover the whole structure. Specifically, the low value of $M_\theta^e$ of (0,6) Type-II SWBNT, might be possibly caused by its rather 'weak' $\sigma$-bond which is under strain along the tube circumferences.

**Table 5.6:** The calculated values of axial and radial linear moduli according to the continuum model of SWBNTs together with SWCNT [225].

| Elastic Moduli (GPa) | Elemental Single-Wall Nanotubes | | | |
|:---:|:---:|:---:|:---:|:---:|
| | (6,0) Type-I | (0,6) Tpe-II | (6,0) Type-III | SWCNT with r = 4Å |
| $M_z^e$ | 929 | 146 | 276 | 1100 |
| $M_r^e = M_\theta^e$ | 669 | 93 | 201 | 750 |

### 5.4.4.2  Crystalline Bundles

Similar to the pristine SWBNTs, the mechanical properties such as the bulk modulus, $B_0$ of their corresponding crystalline bundles can be derived based on a linear elastic solid model, besides fitting to the equations of states of one material. Assuming very weak intertubular interactions in the initial model of our hexagonal crystalline bundles (i.e. sparse configurations in both type-I and III SWBNTs as shown in Table 5.4), one can expect these bundles to be flexible in the basal plane, yet very stiff along the axial direction (i.e. high $M_z^e$ in general) similar to the individual tubules. Therefore, based on the conventional classical continuum model[210] by assuming extreme disparity between the intertube and intratube interactions, together with neglecting the coupling between the two interactions in our model initially when inter-tubular separation are large, accordingly we can define $B$ which analogous to the deformations in the plane perpendicular to the tubular axis as[210]:

$$B_0 \; = \; \frac{(c_{11} + c_{12})}{2} \; = \; \frac{A_0^2}{V_0} \frac{\partial^2 E}{\partial A^2}\big|_{A_0} \tag{5.10}$$

where the $A_0$ and $V_0$ are corresponding equilibrium cross-section and cell volume of the system. Here from this method, the predicted $B_0$ of type I and type III SWBNTs crystalline bundles are to be 52 and 135 GPa respectively.

On the other hand, these properties can also be extracted by fitting to an equation of states (EOS) of one material, i.e. SWBNTs bundles. We use a quasi-harmonic approximation to obtain thermodynamic properties of the SWBNT bundles in which

the Debye temperature $(\Theta_D)$ is taken to be dependent upon the volume of the crystalline bundles[228]. Accordingly, the calculated potential energy surface (Fig. 5.4) is fitted to the well-known Vinet's equation of state (EOS)[229] as shown in Fig 5.9. It yields the bulk modulus $(B_0 =)$ of 84.9 GPa for type I and 110.5 GPa for type III bundles. Interestingly, these values are found to be consistent with the predicted values of $B_0$ which we obtained from linear elastic solid model with predicted $B_0$ to be: 52 GPa for type I, and 135 GPa for type III, as we mentioned. Thus, it is important to note that the consistency of these two set values of $B_0$ for type I and type III SWBNTs bundles, obtained from two different models, can be compared with $B_0$ of carbon nanotubes bundles at the same footing, since the validity of these models applied to the latter have been well justified[210, 221, 225, 230].
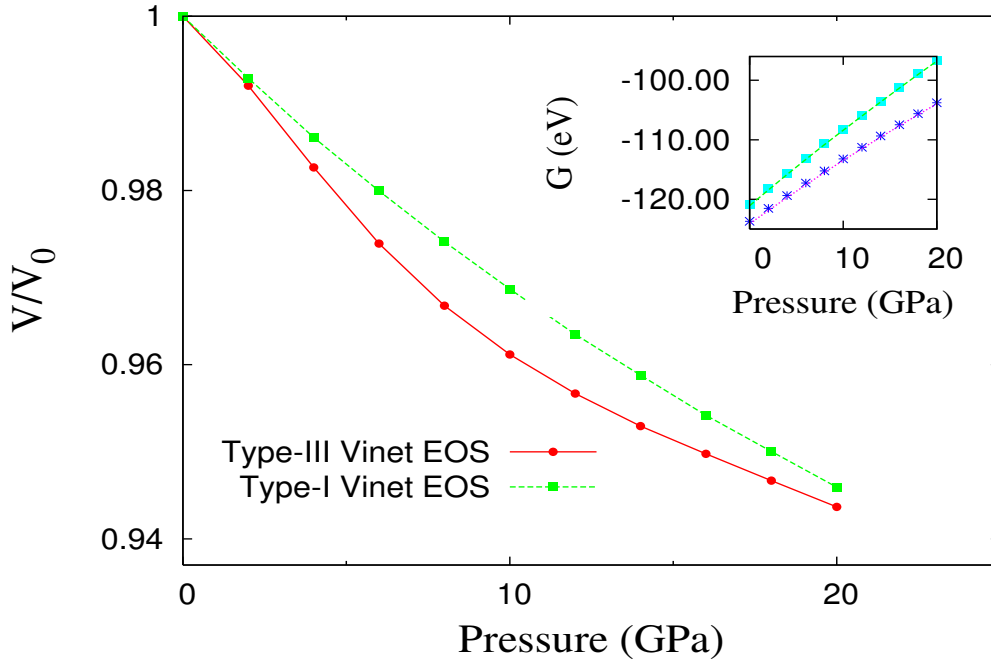


**Figure 5.9:** Vinet's equation of states plots for type I and type III bundles. The inset figure shows the calculated Gibbs energies at $0K$ and $300K$ for both type I and type III bundles.

The calculated results therefore find the modulus of compressibility for SWBNT crystalline bundles to be significantly higher than that of carbon nanotubes-based bundles having the bulk modulus of about 42 GPa[230]. In this case, a relatively higher modulus of compressibility of SWBNT bundles over SWCNT bundles can be attributed to the dissimilar strength of the inter-tubular interactions in BNTs and CNTs. For CNT bundles consisting of SWCNTs with radii $\sim$ 3.8 - 7.0 Å bundles. The previous studies predict that the pristine CNTs interact weakly at separation $\sim$ 3.1 Å, relative to that of graphite layers separated at 3.35 Å[225, 230]. On the other hand, the equilibrium configuration of small-diameter SWBNT bundles indicates the inter-tube distance, $R_{inter} \sim$ 1.7 - 2.0 Å, and the inter-tube interaction is dominated by a relatively stronger $2c$ and $3c$ bonds as mentioned in the Sec 5.4.2.

### 5.4.5 Thermodyanamical Properties

In this section, we analyze the thermodynamic properties of SWBNTs at finite temperature using a Debye-type model[228]. The input for this model is a set of $(E_{coh}, V)$ points which cover a volume range $\sim -30\%$ - $\sim +50\%$ of the static equilibrium volume at zero pressure, $V_0$. In this model, we take into account the vibrational motion of the lattice, follows a quasi-harmonic approximation, making the Debye temperature $\Theta_D$ dependent upon the the volume of the crystalline bundles. At every volume $V$, $\Theta(V)$ is rigorously defined in terms of the elastic constants through a spherical average of the three components of the sound velocity, which the latter may be obtained by solving the Christoffel equations of the crystal. Computationally, however

this procedure would imply the accurate calculations of all the independent elastic constants of the crystals at every pressure of interest. So this highly demanding task has been simplified through the isotropic approximation, which allows to evaluate $\Theta_D$ using the expression[228]

$$\Theta_D = \frac{\hbar}{k_B} \left[ 6\pi^2 V^{1/2} r \right]^{1/3} \sqrt{\frac{B_s}{M}} f(\nu) \tag{5.11}$$

where $\hbar$ is the reduced Planck constant, $k_B$ is the Boltzmann constant, $M$ is the molecular mass of the compound, $r$ the number of atoms per molecular unit, $B_s$ the adiabatic bulk modulus of the crystal, and the $\nu$ the Poisson ratio we obtained for the SWBNT. The details of the explicit expression for the $f(\nu)$ in the equation can be found elsewhere[228]. In order to evaluate the effect of the $\nu$-dependence of the $\Theta_D$ in the explored temperature region, the computed values of $V_0$ and $B_0$ found by less than 0.3% and 1.8%, respectively, from $\nu = 0.10$-$0.20$. In Eq. 10, $B_s$ depends on $V$ and $T$. In order to balance computational demand and accuracy, we use a further approximation that reduces $\Theta_B$ to a function of $V$:

$$B_s \simeq B_{static} = V \left( \frac{d^2 E_{coh}(V)}{dV^2} \right) \tag{5.12}$$

where $B_{static}$ is the static bulk modulus under hydrostatic conditions.

Therefore, this relevant feature of the model makes it fully independent of any particular crystalline structure, where a set of pairs $(E_{coh}, V)$ is sufficient to run the model

under these approximations. Hence, the main drawback of this model might be the fact the geometrical parameters are functions of the volume only, which equivalent to assuming that thermal dilatation changes the structural parameters of a crystal is in the same way as a hydrostatic expansion does. In order to obtain the equilibrium volume at constant $p$ and $T$, we minimize the Gibbs function with respect to $V$. The nonequilibrium $G$ is given by

$$G^*(V;T,p) \;=\; E_{latt}(V) + pV + F_{vib}(T,\Theta(V)) \tag{5.13}$$

where $F_{vib}$ is the vibrational Helmholtz function including zero-point contributions, as given by the Debye model. Then the $V(T,p)$ curve or equation of states (EOS) is implicitly defined by the relation:

$$\left( \frac{dG^*(V;T,p)}{dV} \right) \;=\; 0 \tag{5.14}$$

and the isothermal bulk modulus is given by

$$B_T(T,p) \;=\; V(T,p) \left( \frac{d^2G^*(V;T,p)}{dV^2} \right) \tag{5.15}$$

To analyse the $V(p)$ behavior of the two SWBNTs based bundles (i.e. Type-I and Type-III as shown in Fig. 5.4), we use the $V(T,p)/V_0(T) = V/V_0$ *versus* $p$ diagram. To derive their thermodynamic properties, the calculated energy surface for the both crystalline bundles structure (shown in Fig. 5.4) are fitted to the two different, and

161

well checked empirical EOS[228, 229, 231]: the Vinet EOS and Birch-Murnaghan EOS. We find that these two functional forms yield almost coincident values along the explored $V(p)/V_0$ range, with similar trend of pressure dependence for the $V/V_0$ ratio. So for the later discussion, only the results based on Vinet EOS will be given. The Gibbs function is now minimized with respect to $V$ to obtain the equilibrium volume of the crystalline bundles at constant $p$ and $T$. As shown in the subset of Fig 5.9, type III bundles become relatively stable with respect to type I bundles as the pressure is increased. The Gibbs free energy difference between type I and type III bundles increases from $\sim 270$ to 690 kJ/mol (i.e. $\sim 2.80$ to 7.15 eV) as we increase the pressure from zero to 20 GPa at 0 $K$. This trend persists even at $300K$. Overall, a close-packed condensed crystalline phase for the SWBNTs bundles is predicted to be thermodynamically stable in the present study.

Based on the Debye model[228], the Debye temperature ($\Theta_D$) was calculated using the second derivative of $E_{coh}$. It is predicted to be 957 and 731 $K$ at zero temperature, and 945 and 704 $K$ at room temperature for type I and type III bundles, respectively. For both crystalline bundles, the calculated $\Theta_D$ are found to be less than that of 1219 $K$ for $\beta$-boron solid[37], but higher than that of 402 $K$ for graphite[232, 233]. Interestingly, within the Debye's model, the temperature dependence of the heat capacity can be well-defined by Debye temperature $\Theta_D$ related to maximum phonon frequency, $\nu_D$ in the phonon spectrum. Since the vibrational frequency is always proportional to the square root of the stiffness within the harmonic approximation, $\Theta_D$ can be used to characterize the stiffness of a solid, referred to as 'Debye stiffness'[233]. The Debye

stiffness (which $\propto \Theta_D$) is then related to the hardness (in terms of resistance to plastic deformation) of a material expressed quantitatively by the bulk modulus $B_0$. Our results for the Debye temperature $\Theta_D$ are consistent with the order of the calculated values for the bulk modulus for both type I and type III BNT bundles ($B_0 = 84.9$ and 110.5 GPa respectively), graphite[225, 233] ($B_0 \sim 28$ - 39 GPa) and boron solids ( $B_0 \sim 185$ and 178 - 220 GPa for $\alpha$ and $\beta$ phases, respectively[36, 202]).

## 5.5  Summary

It is shown that the SWBNTs can be feasible and should be all metallic irrespective of their chiralities and diameters. SWBNTs could therefore be an ideal conducting nanowire, comparable to carbon nanotubes. The metallic crystalline bundles of small diameter single-walled boron nanotubes are predicted to be thermodynamically stable with novel properties. Similar to their corresponding $2D$ boron sheets with distinct variations in chemical bonding (Chapter 4), the dominance of inter-tubular interactions involving two-centered and three-centered bonding features in SWBNT bundles relative to the Van der Waals interactions yield different structural, mechanical, and electronic properties relative to those associated with isolated SWCNTs. Within the small radii regime, it is predicted that if isolated or sparse bundles of small diameter SWBNTs are grown, type I bundles based on the reconstructed {1221} boron sheet configuration will be energetically preferred. On the other hand, the close-packed type III bundles based on the idealized {1212} boron sheet configuration are preferred in the equilibrium configuration. Based on the current study on small diameter SWBNT bundles, together with the previous findings from Kunstmann $et$ $al.$[199], scenario of chiralities and diameters dependent in BNTs growth are found to be rather unique compared to other nanotubular systems. Finally, a subtle competition among the intra- and inter-tubular bonds (i.e. among type I and type III SWBNTs) appears to lead to polymorphism associated with the boron nanotubes suggesting that it may be one of the causes of the difficulty in synthesizing SWBNTs.

# Chapter 6

# Electron Transport of SWBNTs: A Preliminary Study With A "Toy-Model"

## 6.1 Introduction

An ever increasing need for smaller, denser, and faster processors has led to focused efforts toward developing and identifying novel one dimensional $(1 - D)$ systems as the basic building blocks for nanoscale electronic devices. Among others, the carbon nanotubes (CNTs) have emerged as prototypical $1 - D$ system and have been the subject of intense research in recent years for their applications in nanoelectronics. However, despite their excellent mechanical and electrical characteristics, the

CNTs suffer from serious limitations due to a lack of the availability of high-purity materials[234]. Therefore, attention is now turned to alternatives to CNTs that can be bulk produced in high purity and can be easily processed and integrated with existing Si-based processes. Toward that, elemental boron nanotubes (BNTs) are recognized as a potential candidate material due to their uniform electronic properties. A recent experiment[56] reporting the synthesis of single-wall boron nanotubes (SWBNTs) has further evoked the interest and expectations for their applications in nanoelectronics.

In this chapter, we report the results of our quantum mechanical study of electron transport in SWBNTs using the Landauer-Büttiker multichannel approach in conjunction with a tight-binding model. We note here that a number of theoretical studies[7, 10, 185, 197, 199, 206] were directed toward understanding the formation and structure of BNTs. Our calculated results find a higher conductivity associated with SWBNT relative to the conductivity of SWCNT of similar geometry. Furthermore, our calculations suggest that between 1-5.0 $nm$, the electron transport in a BNT is ballistic in nature.

Specifically, this chapter will be our very first step towards a detailed study of the electron transport properties of boron based nanostructures. The presentation of this chapter is organized as follows: A brief overview of ballistic electron transport will be given in Sec. 6.1.1, followed by the brief introduction of Landauer-Büttiker Formalism in Sec.6.1.1.1. In Sec. 6.1.1.2 the basic formalism of Non-Equilibrium Green's Functions, NEGF (which also known as: Keldysh method) will be addressed. In the following section (i.e. Sec. 6.1.2), we will discuss the basic notion of electronic

structures theory using the tight-binding method which we employed for the matrix elements in the calculations, before the computational details (Sec. 6.2) and discussion of the theoretical results (Sec. 6.3) in this work will be mentioned. Finally, the importance of this work will be concluded as a summary at Sec. 6.4.

### 6.1.1 Ballistic Electron Transport

The mechanism of electron conduction in a macroscopic system has been studied for years. In solids, such as metals and semiconductors, electrons in the vicinity of the Fermi level are accelerated by an applied electric field, and undergo inelastic scattering with energy dissipation caused by lattice vibrations (i.e. phonons) and collisons with impurities. If we repeat the process in which electrons are accelerated and inelastically scattered, electrons in general will proceed in the direction of the electric field via 'drift conduction' and reach drift speed, which is proportional to the magnitude of the electric field. As a result, for a conductor wire which is much longer than the '*mean free path*' of the electrons (i.e. which is the average distance that electrons proceed without subjected to scattering: typicaly $\sim$ 10 - 50 nm for metallic bulk at room temperature)[235], Ohm's law holds. In this case, electric conductance is inversely proportional to the length of the wire and proportional to its cross-sectional area.

In contrast, for nanostructures in which fine nanowires shorter than the '*mean free path*' are connected to electrodes, most of the electrons will proceed without inelastic

scattering, and entering the nanowires *'ballistically'* from one end to the other. This type of the conduction is called *'ballistic electron transport'*[218, 236, 237]. Hence in the case of the ballistic transport, the conductances are independent of the length of the nanowires, suggesting that the Ohm's law will not hold in this regime. Furthermore, when the diameter of the cross section of the nanowires becomes as small as the Fermi wavelength, $\lambda_F$ of electrons (e.g. the Fermi wavelength for gold is 0.52 nm), electrons can pass through the nanowires only via the quantized energy levels[237]. Therefore, a conduction phenomenon that is significantly different from that having the general macroscopic diffusive electron transport characteristic of solids, should be observed in this regime, namely conductance quantization, unusual current-voltage characteristics, Coulomb blockade effect, etc. Within this regime, theories developed by Landauer[238, 239] and Kubo[240] make up the basic theory of electronic transport which is widely used today. However, the former is physically more intuitive, and powerful for low dimensional problems, particularly one-dimensional problems (e.g. nanotubes). Hence in this chapter, we will mostly focus on the description of the Landauer formalism as the main tool in our study.

We will therefore restrict ourselves in considering the elastic scattering as the dominant mechanism that has, in fact, been studied in conventional nanodevice junctions. Thus, the electrons never actually localize on the molecules or nanowires. Instead, there is a coherent tunneling process from one electrode to another electrode through the molecule or nanowire, in which the switching, inelastic scattering and vibronic coupling are ignored. Therefore, one can say that the conventional Landauer formal-

ism only holds within the elastic scattering limit. In general, we expect the elastic scattering to be dominant for low temperatures, short junctions, and low bias voltages, as long as the Landauer's theory holds.

### 6.1.1.1   The Landauer-Büttiker Formalism

Figure 6.1 illustrates the Landauer's model which treats the current as a transmission function obtained from quantum mechanics. The general extension of the Landauer's model, which was proposed in 1957, is currently known as Landauer-Büttiker formalism[241], partly contributed by Fisher and Lee[242] in 1981. In fact, this formalism establishes the fundamental relation between the wave functions (i.e. scattering amplitudes) of a noninteracting quantum system and its conducting properties. It can be generally applied to find the current through a noninteracting quantum system or through an effectively noninteracting quantum system, as long as the conventional mean-field description is valid and inelastic scattering features are not essential. As a result, it is now widely accepted as a basic model of coherent transport within the quantum regime.

The Landauer's model consists of three parts (Figure 6.1): reservoirs (e.g. metal contacts), quantum leads, and the scattering region. Basically the set up of this model is close to the real situation. What drives the current is the difference of chemical potentials, $\mu_L$ and $\mu_R$, of the left and right electrodes, respectively. We assume that the electrodes are 'ideal' electron reservoirs having the following characteristics:
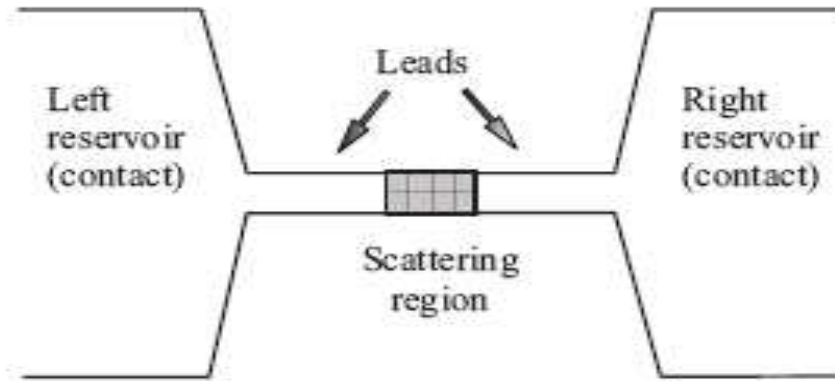
**Figure 6.1:** A scattering region is connected to the reservoirs through quantum leads

† Any electron with energy E < $\mu_L$ ($\mu_R$) is supplied to the left (right) lead from the left (right) electrode.

† All the electrons entering the electrodes from the leads are accepted by the electrodes.

† Inside the electrodes, inelastic scattering frequently occurs and thermal equilibrium is achieved rapidly. The capacity of the electron reservoir is so large that the chemical potentials of the electrodes are maintained at $\mu_L$ and $\mu_R$, independently of the input and output of electrons through the leads.

† The leads are ideal such that electrons are not scattered inside the leads, but merely pass through the leads. In the scattering region, only elastic scattering

170

can take place and hence electrons move coherently between the electrodes.

The main property of the quantum leads is that they have known mode structure, incoming, $\psi_+(r)$ (i.e. from contacts to scattering region), and outgoing modes, $\psi_-(r)$ which can be defined. Scattering region can be as simple as one tunneling barrier, or as complex as an interacting nonequilirium molecule/junction. The elastic scattering process of electrons in the scattering region considered, can be expressed by the transmission probability, $T$, and reflection probability, $R$, which $T + R = 1$. Accordingly, the transmitted electrical current is given by $I_T = I_{in}T$. Using the definition $I = qJ$, the incoming current $I_{in}$ can defined as $I_{in}$ = -$e\nu\rho$. To estimate the velocity, $\nu$ and the density, $\rho$ of the incoming electrons, the $\nu\rho$ can be given by the simple expression: $\nu\rho$ = $\frac{\Delta V}{\pi\hbar}$ = $-\frac{eU}{\pi\hbar}$, which $\Delta V$ is the potential drop. As a result, the transmitted current now is defined as: $I_T = \frac{e^2}{\pi\hbar}UT$. Hence, the conductance $G$ now can be defined as:

$$G \; = \; \frac{I_T}{U} \; = \; \frac{e^2}{\pi\hbar}T \tag{6.1}$$

which known as the single-channel Landauer formula[218], with the fundamental quantum conductance, $G_0 = \frac{e^2}{\pi\hbar} \approx 7.75 \times 10^{-5}\Omega^{-1}$. Similarly the fundamental quantum resistance, $R_0 = \frac{1}{G_0} \sim 12.9 \; k\Omega$. Subsequently, the Eq. 6.1 for the conductance of a single channel can be extended to the case of zero temperature multichannels[241, 242]. By postulating the transmission coefficient $t_{ij}$ to be the probability amplitude at which electrons are transmitted from an initial mode $i$ to a final mode $j$ inside the

conductor, one finds that the conductance is expressed by

$$G = \frac{2e^2}{h} Tr(\hat{t}\hat{t}^+) = \frac{2e^2}{h} \sum_{i,j} |t_{ij}|^2 = \frac{2e^2}{h} \sum_n T_n \tag{6.2}$$

which $\hat{t}$ is the transmission matrix, and $T_n$ are the eigenvalues of the matrix $\hat{t}\hat{t}^+$. Whereas in the multi-channel case at finite voltage and finite temperature, the following generalized Landauer's formula for current (i.e. the general two-terminal formula) will be

$$I(V) = \frac{e}{h} \int_{-\infty}^{+\infty} \bar{T}(E,V)[f_L(E+V) - f_R(E)]dE \tag{6.3}$$

where $\bar{T}(E,V) = Tr(\hat{t}\hat{t}^+)$ is the effective transmission function for the electrons with the energy $E$. Here, it is important to note that the most significant advantage of this formula is, that the transmission function can be calculated from the quantum scattering theory. Thus, the quantum kinetic problem can be reduced to the pure quantum mechanical problem of a single particle in a static potential. Similarly for the generalized multi-terminal Landauer's formula (extended by Büttiker)[241], the current from the $i$-th contact to the system will be:

$$I_i = \frac{e}{h} \int_{-\infty}^{+\infty} \sum_{i \neq j} \bar{T}_{ij}(E,V)[f_i(E+V_{ij}) - f_j(E)]dE \tag{6.4}$$

where $V_{ij}$ is the voltage between the contacts $i$ and $j$.

Here once we have Landauer's formula as mentioned, the way to represent the trans-

mission function needed to be addressed. In this respect, a large majority of the theoretical work in this field is centered around this coherent transport regime, to try to relate the transmission function with scattering matrix ($S$-matrix). In this case, the Green's function $G^R(r, r')$ can be viewed as a generalized $S$-matrix that allows us to describe the response at any point $r$ due to an excitation or perturbation at point $r'$ in general. It provides a convenient way for calculating the $S$-matrix of arbitrarily shaped conductors, especially when a device (e.g. a molecule or a nanotube) is connected to two contacts (reservoirs) with two different Fermi level $E_{f1}$, and $E_{f2}$, which consequently cause an electron flow under a nonequilibirium steady-state condition[218].

### 6.1.1.2  Non-Equilibrium Green's Functions, NEGF

The focus here is on the nonequilibrium Green's function (NEGF), which is one of the ways to deal with the complexities introduced by the coupling between the discrete states of the molecule and the continuous states of the electrodes within a two probe model. It is also the most common way in which this problem has been addressed by the community. *One fundamental understanding is that the conductance is not the conductance of a molecule, or a nanowire, but rather the conductance of a composite system containing the molecule, two interfaces, and two continuum electrodes.* The ways to calculate it will be shown briefly as following[218, 243].

Here, the Green's function of the device ($G_d$) can be calculated separately without calculating the whole Green's function ($G$). From the definition of the Green's func-

173

tion:

$$(E - H)G(E) = I \tag{6.5}$$

similarly we can define the Green's function of the device as following:

$$\begin{pmatrix} E - H_1 & -\tau_1 & 0 \\ -\tau_1^+ & E - H_d & -\tau_2^+ \\ 0 & -\tau_2 & E - H_2 \end{pmatrix} \begin{pmatrix} G_1 & G_{1d} & G_{12} \\ G_{d1} & G_d & G_{d2} \\ G_{21} & G_{2d} & G_2 \end{pmatrix} = \begin{pmatrix} I & 0 & 0 \\ 0 & I & 0 \\ 0 & 0 & I \end{pmatrix} \tag{6.6}$$

Selecting the three equations in the second column:

$$(E - H_1)G_{1d} - \tau_1 G_d = 0 \tag{6.7}$$

$$-\tau_1^+ G_{1d} + (E - H_d)G_d - \tau_2^+ G_{2d} = I \tag{6.8}$$

$$(E - H_2)G_{2d} - \tau_2 G_d = 0 \tag{6.9}$$

Here, we can solve Eq. 6.7 and 6.9 for $G_{1d}$ and $G_{2d}$:

$$G_{1d} = g_1 \tau_1 G_d \tag{6.10}$$

$$G_{2d} = g_2 \tau_2 G_d \tag{6.11}$$

Hence, if we substitute these $G_{1d}$ and $G_{2d}$ into the Eq. 6.8, it gives

$$-\tau_1^+ g_1 \tau_1 G_d + (E - H_d) G_d - \tau_2^+ g_2 \tau_2 G_d = I \tag{6.12}$$

from which we can define $G_d$ as:

$$G_d = (E - H_d - \Sigma_1 - \Sigma_2)^{-1} \tag{6.13}$$

where $\Sigma_1 = \tau_1^+ g_1 \tau_1$ and $\Sigma_2 = \tau_2^+ g_2 \tau_2$ are the so-called self-energies, which play an important role by including the effect of the infinite contacts (reservoirs) to the molecule or nanowires, which are coupled to it.

Here, in the nonequilibrium case we are often interested in another important quantity: the current which is given by Landauer's formula. To calculate it, we need an expression for the current from the wavefunction via probability current. In steady-state, the probability to find an electron on the device (i.e. $\sum_i |\psi_i|^2$ where the sum spans over the device subspace) is conserved, $\frac{\partial \sum_i |\psi_i|^2}{\partial t} = 0$. Therefore for an arbi-

175

trary contact $j$, the electric current (at one energy) will be the charge (-$e$) times the

probability current:

$$i_j = -\frac{ie}{\hbar}(\langle\psi_j|\tau_j|\psi_d\rangle - \langle\psi_d|\tau_j^+|\psi_j\rangle) \tag{6.14}$$

where $i_j$ is defined as a current from the contacts into the device. Thus the current

into the device from a incoming wave of one energy ($E$) in contact 1 ($|\psi_{1,n}\rangle$) through

the coupling defined by $\tau_2$ is:

$$
\begin{aligned}
i_{2from1} &= -\tfrac{ie}{\hbar}(\langle\psi_2|\tau_2|\psi_d\rangle - \langle\psi_d|\tau_2^+|\psi_2\rangle) \\
&= -\tfrac{ie}{\hbar}(\langle\psi_{1,n}|\tau_1 G_d^+ \tau_2^+ g_2^+ \tau_2 G_d \tau_1^+|\psi_{1,n}\rangle - \langle\psi_d|\tau_1 G_d^+ \tau_2^+ g_2 \tau_2 G_d \tau_1^+|\psi_{1,n}|\psi_2\rangle) \\
&= -\tfrac{ie}{\hbar}\langle\psi_{1,n}|\tau_1 G_d^+ \tau_2^+ (g_2^+ - g_2)\tau_2 G_d \tau_1^+|\psi_{1,n}\rangle \\
&= \tfrac{e}{\hbar}\langle\psi_{1,n}|\tau_1 G_d^+ \Gamma_2 G_d \tau_1^+|\psi_{1,n}\rangle
\end{aligned}
\tag{6.15}
$$

with $\Gamma_2 = \tau_2^+(g_2^+ - g_2)\tau_2 = i(\Sigma_2 - \Sigma_2^+)$, which describes the coupling at the contact

2. Similarly, $\Gamma_1 = \tau_1^+(g_1^+ - g_1)\tau_1 = i(\Sigma_1 - \Sigma_1^+)$, represents the coupling at the contact

1. If we sum over the modes $n$ and noting that the levels are filled from the reservoir

connected to contact 1 gives (2 for spin):

$$
\begin{aligned}
I_{2from1} \quad &= \quad \frac{2e}{\hbar} \int_{E=-\infty}^{\infty} dE f(E, E_{f1}) \sum_n \delta(E - E_n) \langle \psi_{1,n} | \tau_1 G_d^+ \Gamma_2 G_d \tau_1^+ | \psi_{1,n} \rangle \\
&= \quad \frac{2e}{\hbar} \int_{E=-\infty}^{\infty} dE f(E, E_{f1}) \sum_{m,n} \delta(E - E_n) \langle \psi_{1,n} | \tau_1 | m \rangle \langle m | G_d^+ \Gamma_2 G_d \tau_1^+ | \psi_{1,n} \rangle \\
&= \quad \frac{2e}{\hbar} \int_{E=-\infty}^{\infty} dE f(E, E_{f1}) \sum_{m} \langle m | G_d^+ \Gamma_2 G_d \tau_1^+ (\sum_n \delta(E - E_n) | \psi_{1,n} \rangle \langle \psi_{1,n} |) \tau_1 | m \rangle \\
&= \quad \frac{2e}{\hbar} \int_{E=-\infty}^{\infty} dE f(E, E_{f1}) \sum_{m} \langle m | G_d^+ \Gamma_2 G_d \tau_1^+ \frac{a_1}{2\pi} \tau_1 | m \rangle \\
&= \quad \frac{e}{\pi \hbar} \int_{E=-\infty}^{\infty} dE f(E, E_{f1}) Tr(G_d^+ \Gamma_2 G_d \Gamma_1)
\end{aligned}
$$

$$(6.16)$$

To get the total net electric current through the device, the current from contact two have to be substracted away:

$$
I = \frac{e}{\pi \hbar} \int_{E=-\infty}^{\infty} dE \{ f(E, E_{f1}) - f(E, E_{f2}) \} Tr(G_d^+ \Gamma_2 G_d \Gamma_1) \qquad (6.17)
$$

which is exactly the Landauer's formula for the current as we shown before. Hence, the next step will be we use the conventional quantum chemistry techniques to obtain the matrix elements needed for Eq. 6.13 and Eq. 6.17 to calculate the current.

## 6.1.2 Electronic Structures Theory: Tight-Binding Method

It is noteworthy to point out that the matrices appearing above depend on the basis functions that are used for the electronic structure calculation for the scattering region and contacts. In order to model this 'big' molecular device (i.e. number of atoms in

scattering region: $\sim 500$ - 1000 atom), we resort to use the localized atomic orbitals based on tight-binding method, insetad of the state-of-the-art all electron calculations, to reduce the computational cost. All of the tight-binding calculations we used are based on two-center tight-binding method using the nonorthogonal basis[125], and the parameters being used are obtained based on the fitting to the *first-principles* band structures at high symmetry points[244].

Hence, this 'semi-empirical' method is particular simple and fast, only the matrix elements of the overlap and the hamiltonian are needed to carry out the electron transport calculation. Basically, all the matrix equation mentioned within the NEGF method are still valid, except that the matrix elements in Eq. 6.13, which needed to be modified by $G_d = (ES - H_d - \Sigma_1 - \Sigma_2)^{-1}$, where the $S$ represent the overlap matrix of the basis functions $\phi_m(r)$:

$$ S_{mn} = \int d^3 r \phi_m^*(r) \phi_n(r) \tag{6.18} $$

For the orthogonal bases, $S_{mn} = \delta_{mn}$ so that $S$ is the identity matrix as stated earlier (Eq. 6.13). More details of the parameters and computational techniques which we used, will be given in the following section.

## 6.2 Computational Methodology

In the present study, all the geometry of the SWBNTs, namely the (6,0) zigzag type-I, (0,6) armchair type-II, and (0,6) armchair/zigzag type-III, were taken from our previous work[7, 9]. The geometrical arrangement used to calculate the electron transport properties of the SWBNT is shown in Figure 6.2. Based on a two-probe device architecture, the device scattering region consists of a SWBNT, with varying length which was sandwiched between two gold layered electrodes at each side as shown.
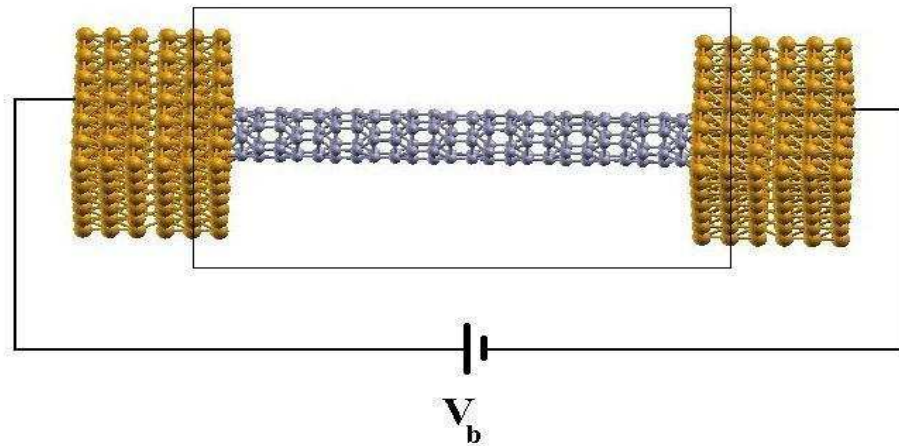


**Figure 6.2:** A schematic diagram of two probe device architecture with SWBNT sandwiched between two gold electrodes. The region with the rectangular box is taken to be the simulation cell for transport calculations.

In this work, the current-voltage $(I - V)$ characteristics of SWBNTs was calculated by nonequilibrium Green's function (NEGF) method[218] utilizing the Landauer-

Büttiker formalism[218, 239, 241, 245] as:

$$I = \frac{2e}{h} \int_{E_f-eV/2}^{E_f+eV/2} T(E,V)\{f(E,E_f - \frac{eV}{2}) - f(E,E_f + \frac{eV}{2})\}dE \qquad (6.19)$$

In Equation 6.19, $T(E,V)$ is the transmission function, $E$ is the injection energy, and $E_f$ represents the Fermi energy of Au-electrode. The transmission function, $T(E,V)$ is calculated as,

$$T(E,V) = Tr\{\Gamma_L G^R \Gamma_R G^A\} \qquad (6.20)$$

The Green's function, $G^R$ in the present study was obtained in the framework of nonorthogonal tight-binding model. Within this scheme, four valence $(s, p_x, p_y, p_z)$ orbitals for the boron atom, and only an $s$ orbital for the gold atom were included in the calculation.

Although the nanotube is attached to a layer of gold atoms at either side, however, it does not include the infinite gold contacts which effectively turn the 'isolated' scattering region (i.e. nanotube plus two gold layers at both side) into an open system, which is capable of electron transport. Therefore, we include the effect of the infinite contacts (reservoirs) through the self-energy functions $\Sigma_1$ and $\Sigma_2$ (shown as $\tau_1^+ g_1 \tau_1$ and $\tau_2^+ g_2 \tau_2$ in Eq. 6.13). Here, the $\tau_1$ and $\tau_2$ are the matrices which describe the coupling of the nanotube to the gold electrode, and $g_1$ and $g_2$ are the Green's functions for the isolated gold layer at each side. To adopt this procedure to real

calculations, a coupling factor 0.50 was used as a fitting parameter[246] in all the calculations reported here. This factor was adopted mainly on intuitive geometrical grounds by assuming a planar shape whose volume is about 50% of what it would be if the ideal continuum were able to hypothetically be connected to a nanotube. From surface physics studies, it is known that around the Fermi energy of gold the locl density of states (DOS) is $s$-band dominated and has a nearly constant local DOS of $\sim 0.07$/(eV-atom). Therefore for simplicity, we assume the Green's function to be a diagonal matrix with the diagonal elements equal to $(-\pi i)$ times the local DOS[246] as: $g_{1and2} = $ -0.072 $\pi i$/eV-atom. Consequently, from the Green's function, we can calculate the spectral function $A$ ($A = i(G - G^+)$), which later will be used to calculate the total density of states, $N(E)$ obtained from the trace of the spectra function.

## 6.3   Results & Discussion

In brief, a SWBNT, with varying length was sandwiched between gold electrodes represented by a single layer consisting of 49 gold (Au) atoms at each side. In order to test the convergence of calculated current with respect to the placement of the equilibrium Fermi level ($E_f$), the number of the Au layers was varied from one to six at each side, as shown in the Fig. 6.2. The Au layers were separated by 2.16 Å[202]. For a 35 Å long SWBNT, the calculated current ($I$) and $E_f$ of Au (1-layer)-SWBNT-Au (1-layer) converged within $\sim 7.5$ % and $\sim 1.3$ % with respect to Au (6-layer)-

SWBNT-Au (6-layer), when $E_f$ was placed in the middle of the highest occupied (HOMO) and the lowest unoccupied (LUMO) molecular orbitals of the nanotube-Au system. In the subsequent calculations, we therefore place the equilibrium Fermi level $E_f$ in the middle of the HOMO and the LUMO of the Au (1-layer)-SWNT-Au (1-layer) system. The Au-B separation at the electrode-tube interface was taken to be 1.7 Å, which is approximately the calculated equilibrium distance for diatomic Au-B.

The calculated I-V characteristics for (6,0) zigzag type-I SWBNT of different lengths between 16 and 47 Å are shown in Figure 6.3. Also shown in Fig. 6.3 is the transmission spectrum for a 35 Å (6,0) zigzag type-I SWBNT. The transmission spectra are found to mimic the shape of density of states (DOS). It should be mentioned that the qualitative features of density of states (DOS) of the metallic (6,0) zigzag type-I SWBNT calculated in the present study agree very well with those calculated from the *first principles* methods as mentioned in Chapter 5. It is clear from Figure 6.3 that the calculated current in SWBNT is independent of the length of the tube, indicative of the ballistic nature of electron transport, as we mentioned in Sec 6.1.1.

In order to verify the accuracy of the predicted results for SWBNTs, for which no experimental data exist for comparison, we performed similar calculations on metallic SWCNT, for which experimental and theoretical data exist[247, 248, 249, 250, 251, 252, 253]. Calculations were performed in the similar geometry as shown for the SWBNT in Figure 6.2. In the case of SWCNT, the configuration was taken to be that of armchair (6,6) SWCNT and the electrodes were represented by 81 Au atoms per layer on each side, due to larger in the diameter of SWCNT. The C-Au distance

**Figure 6.3:** I-V characteristics of (6,0) zigzag type-I SWBNT in a strong gold-nanotube-gold coupling regime, with the corresponding figures showing the transmission spectra of the system.

at the metal-molecule interface was taken to be 1.7 Å as approximately the calculated equilibrium geometry for Au-C dimer. As in the case of SWBNT, we take this distance as the strong coupling regime between electrode and nanotube. The calculated I-V characteristics of (6,6) SWCNT of varying lengths between 10 and 53 Å along with the transmission spectrum for one of the tubes (of 26 Å length) are shown in Figure 6.4.

As evident from the figure, the present calculations clearly show a length-independent I-V characteristic for SWCNT, as known from previous experimental and theoretical studies[247, 248, 249, 250, 251, 252, 253]. This gives confidence in our calculations and predicted results for SWBNT. The resistance of (6,0) zigzag type-I SWBNT is estimated to be 7 kilohms to be compared with the corresponding value of about 20 kilohmsïĄŮfor SWCNT. Here, it is noteworthy to point out that from our previous DFT based band structures, the corresponding intrinsic conductance of the SWBNT

183

is $\sim 2G_0$, where $G_0 = \frac{2e^2}{h}$ (with $G_0$ is one unit of quantum conductance defined in Sec. 6.1.1.1) at the Fermi level. Therefore, the calculated difference in total resistance between the gold-BNT-gold and gold-CNT-gold systems appears to be due to their respective contact resistances, assuming the total resistance of the system to be, $R_{total} \sim R_{NT} + R_{ml} + R_{mr}$, which the $R_{NT}$ are intrinsic resistance of a nanotube, $R_{ml}$ and $R_{mr}$ are the contact resistance attributed to left and right metal (Au) contact, respectively. An analysis of transmission spectra given in Fig. 6.3 and 6.4, respectively, suggests that both sub-bands of (6,0) type-I SWBNT carrying current couple well to the metal (Au) as compared to only one of the two sub-bands of (6,6) SWCNT due to the scattering at the interface. This difference, perhaps accounts for the calculated difference in the conductance of SWBNT and SWCNT.
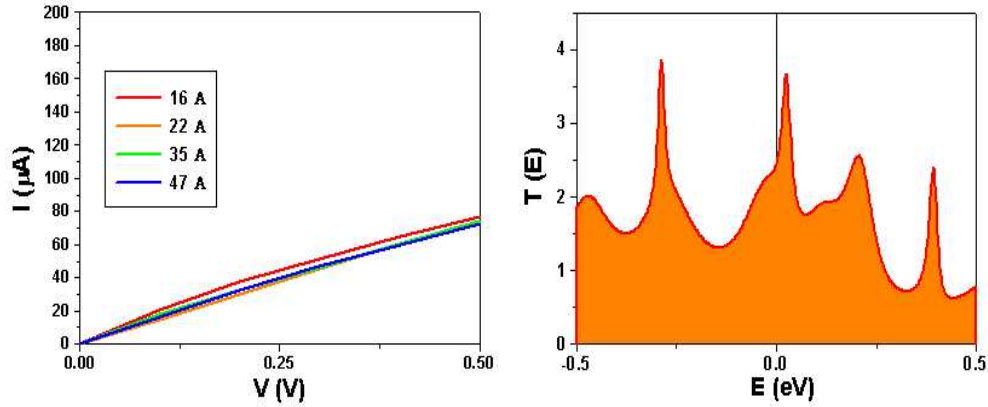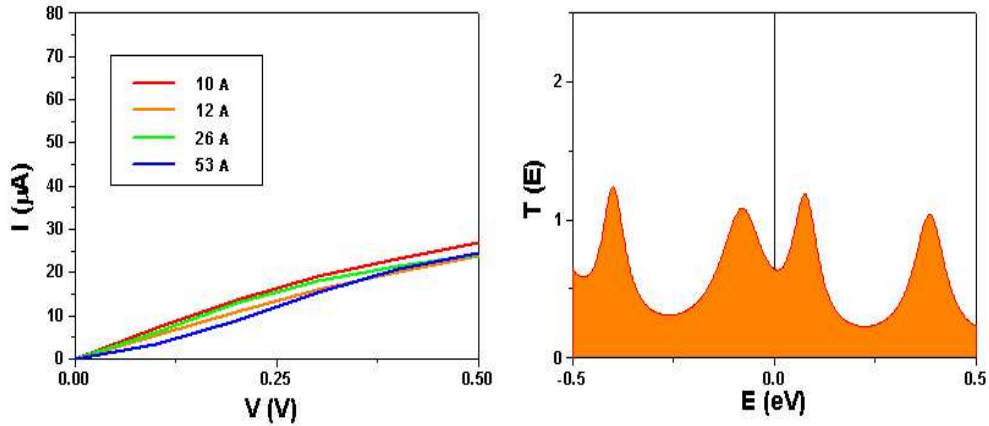


**Figure 6.4:** I-V characteristics of (6,6) armchair SWCNT in a strong gold-nanotube-gold coupling regime, with the corresponding figures showing the transmission spectra of the system.

Further understanding of the conductance in SWBNT can be obtained from an analysis of the nature of the chemical bonds. In our previous study[7, 9] (as mentioned in

Chapter 5), it was noted that the bonding in (6,0) zigzag type-I SWBNT can be described as mixed metallic-like and covalent-type, in contrast to pure $sp^2$-type covalent bonding in the (6,6) armchair SWCNT. Thus, we believe that a mixture of two-center, directional covalent ($\sigma$-type) bonds along the tubular axis and multicenter metallic-like ($\pi$-type) bonds along the circumference of the tube provides conduction channels for the electron transport in SWBNTs. Hence, to explore into depth of this issue, calculations using state-of-the-art real space, nonequilibrium Green's function (NEGF) formalism combined with density functional theory (DFT) based simulation[254] are in progress to confirm the role played by the bonding in the electron transport in SWBNTs relative to SWCNTs.

It is important to note that in addition to the bonding features and electronic structures of the nanotubes, the nature of the metal-tube contact can also influence the calculated/observed resistance of the system. Our calculations suggest that the contact resistance can also be altered by changing $R_{interface}$ (i.e. Au-NT separation at the gold electrode-tube interface) from 1.7 Å to 3.5 Å. In both Au-CNT-Au and Au-BNT-Au systems, a significant decrease in magnitude of current together with a nonlinear variation of current with applied bias is seen (Figure 6.5). In the strong coupling regime ($R_{interface}$ = 1.7 Å) at 0.5 V, a significantly higher current was predicted in both BNT and CNT-systems, as compared to that in the weak coupling regime ($R_{interface}$ = 3.5 Å) at 0.5 V. The decrease in current in the weak coupling regime may be attributed to a shift of the Fermi energy toward the valence band leading to a higher resistance relative to the case of the strong coupling regime where the Fermi

energy shifts toward the conduction band. Also, the discretized energy spectra in density of states of gold-nanotube-gold systems may be attributed to the predicted nonlinear I-V characteristics in the weak gold-nanotube-gold coupling regime.
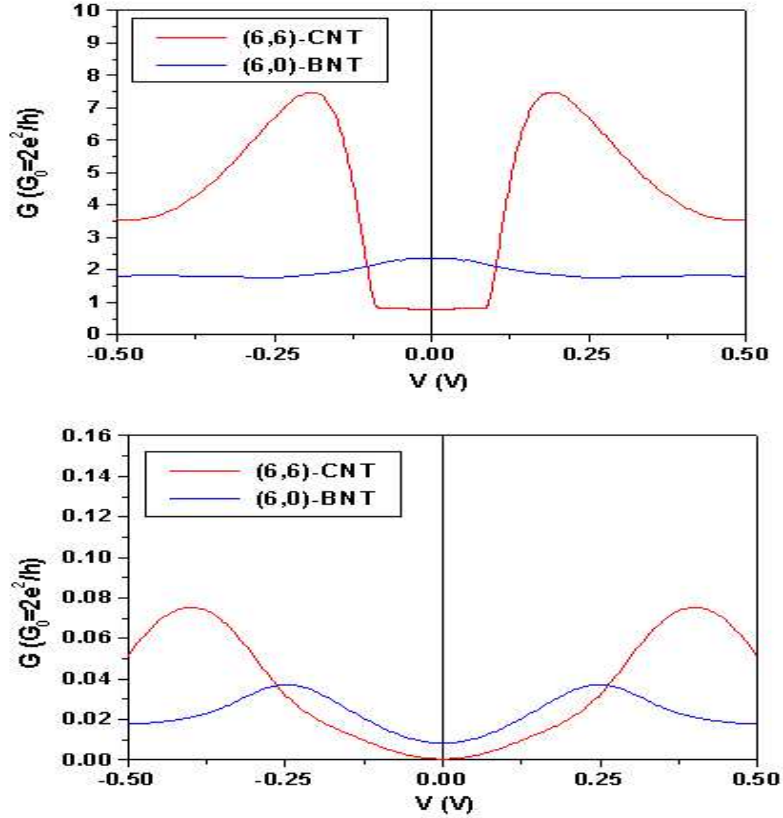


**Figure 6.5:** Conductance (G) of (6,6) SWCNT and (6,0) zigzag type-I SWBNT in strong (top) and weak (bottom) gold-nanotube-gold coupling regime.

In order to gain further insights into the electron transport in nanotubes, we have calculated the conductance $(G)$ in both the cases of strong and weak coupling regimes (Figure 6.6). In the strong coupling regime, a strong oscillation in conductance (i.e. $\frac{dI}{dV}$) is predicted for CNT as compared to a nearly constant slope in current for BNT indicating its ohmic-like I-V characteristics. A similar feature in conductance for

BNT relative to CNT is predicted in the weak coupling regime.

Finally, we consider metallic (0,6) armchair type-II SWBNT for electron transport calculations to explore the effect of chirality on the I-V characteristics. The calculated results suggest that chirality does not appear to play a significant role in determining the I-V characteristics of (0,6) armchair type-II SWBNT. It can be attributed to the similarity of bonding features in (6,0) and (0,6) SWBNTs as noted in our previous study, due to similar bonding features of their $2D$ reconstructed {1221} boron sheets.

## 6.4   Summary

In summary, we have calculated the I-V characteristics of small radii SWBNTs using tight-binding approach and the Landauer-Büttiker multichannel formalism. The calculations predict a ballistic nature of electron transport in SWBNT. Furthermore, the conductivity in SWBNT is calculated to be higher than that in SWCNT, which is attributed to a mixture of two-center, directional covalent ($\sigma$-type) bonds and multicenter metallic-like ($\pi$-type) electron-deficient nature of boron bonds in SWBNT. Metal-tube interface coupling appears to strongly influence the I-V characteristics of the nanotubes. The chirality of boron nanotubes does not appear to play a significant role on determining the I-V characteristics of a BNT. The present study is expected to stimulate further investigations of electronic properties in BNTs.

# Chapter 7

# The 'Grand' Summary

## 7.1  Concluding Remarks

This work has expanded the scope of the studies on boron nanostructures based on the well-established theoretical model: *first-principles* study. Strictly speaking, the studies in boron nanostructures remain elusive, and so far, only the studies (i.e. both experimental and theoretical studies) of boron nanoclusters are comparatively more established, while the rest remains in the infant stage. Following is the list of the accomplishments achieved in this study, when we started involved in this field since 2004.

1. The size-dependent structural transition of $B_n$ nanoclusters can be found as other elements (e.g. carbon). However, it is unique for each different elements. So far, the emergence of $2D$ planar to $3D$ tubular configuration is obvious

in $B_{24}$ regime, though this structural transition remains inconclusive in $B_{20}$ regime. In this context, the emergence of tubular structures in $B_n$ nanoclusters is particularly interesting, and can be comprehended as an important signal for the 'embryo' of boron nanotubes (BNTs). Specifically, analysis of the frequency and IR spectrum of these clusters (i.e. $B_n$ and $B_n^{\pm}$) was predicted. Consequently, for the first time, it is revealed that the characteristic vibrational modes which are associated with the boron clusters, are also typically observed in carbon nanotubes (CNTs). These metastable tubular cluster configurations can be considered as the building blocks of the boron nanotubes.

2. A series of new hypothetical $2D$ boron sheets have been explored from *first-principles* calculations. Above all, we found all the $2D$ boron sheets are metallic, except the sheet based on the $B_{12}$ icosahedral configuration associated with a finite band gap. On the other hand, the emergence of the icosahedral-based boron sheet as one of the low-lying configurations suggests the enhanced stability of inter-icosahedral and intra-icosahedral bonds, despite the fact that the discrete units of $B_{12}$ icosahedral unit are not stable on their own in the small cluster regime. It is suggested that there are only three possible competing planar configurations which can be considered as the candidates to form a nanotubes, namely: the idealized {1212}, reconstructed {1221} and buckled {1212}. The unique features in geometry and electronic properties of both {1212} and {1221} configurations suggest that a strong variation of electronic and mechanical properties is expected to occur when the plane is rolled into

different chirality of single-walled boron nanotubes.

3. The results suggested that the formation of the SWBNTs can be feasible energetically. The SWBNTs should be all metallic irrespective of their chiralities and diameters. This suggests that the SWBNTs could therefore be another unique 'homo-nuclear' nanotubes, besides carbon nanotubes (SWCNTs) and silicon nanotubes (SiNTs). Unlike carbon nanotubes, the crystalline bundles of boron nanotubes are found to be dominated by strong inter-tubular interactions involving two-centered and three-centered bonding features, relative to the Van der Waals interactions in SWCNTs. Hence, this yields a different structural, mechanical, and electronic properties relative to those associated with isolated SWCNTs. Based on the current study on small diameter SWBNT bundles, together with the recent findings from Kunstmann *et al.*[199], a scenario of chiralities and diameters dependent on BNTs growth are found to be rather unique among other nanotubular systems. Finally, a subtle competition among the intra- and inter-tubular bonds (i.e. among type I and type III SWBNTs) appears to lead to polymorphism associated with the boron nanotubes suggesting that it may be one of causes of the difficulty in synthesizing SWBNTs.

4. Following our results based on tight-binding calculations on electron transport studies of SWBNTs, we predict between 1-5.0 $nm$, the electron transport in a SWBNT is ballistic in nature. This important finding could therefore suggest that SWBNT can be an ideal conducting nanowire, comparable to SWCNT. Specifically, we found the chirality of boron nanotubes does not appear to play

a significant role on determining the I-V characteristics of a SWBNT. The preliminary results also found that SWBNT coupled better with an Au-electrode than SWCNT, therefore giving higher conductivity compared to carbon nanotube.

Up to this point, we still believe "There is plenty of room at the bottom in *boron research* ". Indeed, there is still alot of important problems can be explored at this stage, and these problems will be discussed into more details in next chapter. Similarly, the conclusions found in this chapter do not mark '*grand finale*' in this study, but rather another '*new begining*' in this field. So, let us carry on.

# Chapter 8

# The Outlook, but Not the End!

## 8.1   What we have learnt, and What is not yet ?

"The ability to reduce everything to simple fundamental laws

does not imply the ability to start from those laws and reconstruct the universe".

So, that's why we always stuck with more problems!

The theoretical study we performed here is a reconstruction of a solid state material[255] (i.e. boron nanostructures) from our knowledge based on the *first-principles* method. In fact, this work would be as difficult as, if not more so, as we come to understand those features from analysis of the experiments, when available.

Every theoretical method has its own limit. Similarly as a theorist, we have to make many approximations and assumptions in principle deductions, model reconstruc-

tions, theoretical formalism, calculation techniques, and numerical evaluations. Even if each of these approximations is reliable, it is of great difficulty to guarantee that all those accuracies persist through all conditions in which they are involved. Hence, cross-checking and estimation of the possible errors from the established theoretical methodologies, are always important to know their limitations, and to make further progress in understanding of the physics and chemistry of a system.

### 8.1.1 Limitations

Following our theory and methodology introduction in Chapter 2, and its applications in Chapter 3 onwards, we may conclude that *first-principles* calculations are many-faceted complex theoretical architectures. To simplify our problem, let us now just focus on the iterative minimization techniques for total-energy calculations we employed in this work. By following the factors which are involved in total energy calculations, several possible causes of the underlying errors in total energy ($E$) are expected.

#### 8.1.1.1 Hamiltonian ($\hat{H}$)

Hamiltonian ($\hat{H}$) is the key equation governing the dyanmics of a many-body system. Based on the logic of methodology dedeuction, usually the hamiltonian is approximated or idealized, in order to carry out calculations for the practical purposes. However, the main approximations being used in this study can roughly be sum-

marized into two parts: the Born-Oppenheimer (or adiabatic) approximation (Sec. 2.2.1), and the independent-electron approximation (Sec. 2.2.2.1). Strictly speaking, the first approximation is tougher and not well-established. The problems have been studied (e.g. multi-state system, multi-state quantization, molecular field, etc.)[256] so far are rather limited, and might not be relevant in our current study.

Therefore, we will mostly focus on the possible errors which might have arisen from the second approximation: the knowledge of the *exact* exchange-correlation (xc) energy functional $E_{xc}[n]$ in DFT (in Sec. 2.2.2.3). So far, the exchange-correlation ($xc$) energy functional forms which we employed are based on the standard LDA and GGA approximation (Chapter 4 and 5). Fortunately, these approximations are sufficient in determining the basic structural properties based on the ground-state total energy of the system. However, these approximations might not be appropriate for the '*electron-hole*' excitation energies, especially when we want to study how the nanostructures respond to some external probe, e.g. photoemission experiments. Regarding to these excited states study, the use of many-body perturbation theory is necessary. Hence, one of the most practical technique will be Hedin's GW approximation[257, 258]. Interestingly, this technique can also be applied in improving our theoretical prediction on the band gap of $\alpha$-$B_{12}$ bulk and its corresponding $2D$ boron sheet (Chapter 4 and 5), based on both LDA and GGA approximation, or the other possible option: $B3LYP$ exchange-correlation functional in quantum chemistry (Chapter 3, and Appendix A).

### 8.1.1.2   Basis Functions ($\psi$)

The wave function ($\Psi$) is the key for every possible information to physical observables, within the quantum regime. Usually, all the underlying approximation of the wave function, which are based upon the mathematical representation of basis functions ($\psi$) (Sec. 2.4.1), can be systematically analysed. The many-body wave function is often expanded in the Slater determinants constructed from a set of single-particle orbitals, i.e. from a finite and hence incomplete basis set (Sec. 2.4.1). Therefore, the errors or limitations due to the basis functions we employed should be a systematic error in our calculation.

Basically, these 'basis sets errors' can be categorized into three parts: (*first*) type or form of the basis function, (*second*) basis set truncation errors, and (*third*) environment effects. As we mentioned before, the selection of GTOs (Chapter 3 and 5) is due to the reason of ease and efficiency in computation, not due to the physical 'correctness' of its basis functions, compared to STOs. Even among the different forms of GTOs, the basis set errors can be rather substantial (Appendix A). As a trade-off between the accuracy and computational cost, usually for a large system (e.g. $B_{60}$ clusters), we used the smaller basis sets, e.g. STO-3G and 3-21G[6], instead of the standard 6-31G(d,p) which has more primitive gaussians in the valence shell. Secondly, efforts to reduce the errors due to truncation of the basis set can be a major cost of a calculation because of the basis set enlargement. In the planewave basis set (Sec. 2.4.1.3 and Chapter 4, it is attributed to energy cutoff, $\frac{\hbar^2}{2m}|k + G|^2$ (Appendix B). In particular for the LCAO (or LCGTO in CRYSTAL03/06 at Sec. 2.4.1.2 and

Chapter 5) approach with GTOs, the truncation of the infinite series in CRYSTAL code is effective for relatively sharp Gaussian functions. Typically for a covalent-like compounds like boron, the exponents of the most diffuse Gaussians in a double-zeta type basis set (e.g. 6-31G(d,p) in Chapter 3 and 5) are relatively high ($\sim$ 0.13-0.16 $bohr^{-2}$), and the corresponding computational cost is not too large, compared to to a metal (i.e. $\sim \leq 0.1 \ bohr^{-2}$). Similarly for the third part of the basis set errors, the effects cannot be negligible. As shown in Appendix A, there is substantial difference among 6-31G and 6-31G(d,p) plus the diffuse functions, which practically are adopted for an extra flexibility in different chemical environments.

Strictly speaking, all these three parts of the basis set errors cannot be corrected absolutely. However, some of the errors can be narrowed by the basis set optimization procedure, which utilizes the variational principle with respect to the total energy (Sec. 5.3). This procedure is decided by the quality and the applicability of the selected basis set. As long as the changes in basis sets (or the energy gain) are negligible compared to energy gain from geometry optimization procedure, the electronic structures can be considered as 'reasonable'.

### 8.1.1.3  Numerical Techniques

The numerical approximation is inevitable and crucial, as we go from a theoretical model to an actual simultion of real materials. Therefore, the possible errors which arise from the numerical approximation must be a factor in the discussion of the limitations of methodology. In fact, developments of the numerical techniques can be as

complicated as the work spent in buiding up the Hamiltonian, $\hat{H}$ and basis functions, $\psi$, from the integration of motion algorithm to the energy minimization[61]. Also, the errors involved in the reciprocal space integration and in the $k$-point sampling within the Brillouin zone is particularly common (either in planewaves (Chapter 4) or periodic GTOs (Chapter 5)), since it is involved at each stage of the self-consistent procedure, in determining the Fermi energy ($E_f$), and in reconstructing the one-electron density matrix. Usually, this error can be minimized, and the limitation required is therefore determined by a balance among the computational cost and accuracy. In this case, as long as the error ($\Delta E_{kpoint}$) from the $k$-point sampling is negligible, compared to the energy gain ($\Delta E$) in structural relaxation, we can claim that our results are reliable. For example in $\alpha$-$B_{12}$ boron solids, the size of the $k$-point sampling for this system is converged within a precision of $\sim 1$ meV/atom (Appendix B) within a reasonable computational cost.

One of the common numerical inefficiencies found in the conventional study on the structural determination of the ground state configuration, is due to limitation upon the global energy minimization algorithms we employed, namely the conjugated gradient method[123, 157, 207]. Although accurate forces on the ions can be calculated relatively fast when the conjugated gradient method is applied, this technique is basically a zero-temperature quench because the ions do not acquire any kinetic energy during the relaxation procedure. At the end of this process, the system will be in a local energy minimum. Therefore, using this technique to acquire a global energy minimum structure is not a guarantee, and it can be very onerous to find it. Hence,

it is important to point out that all the nanostructures we proposed so far can only be true as a local minima, not an 'absolute' ground state in the global energy surface. To improve the prediction, one has to consider more powerful numerical techniques: e.g. molecular dynamics, simulated annealing, metadynamics, basin hopping, genetic algorithm, or evolutionary algorithm.

## 8.1.2   Suggestions For Future Study

In this work, we have tried to cover much of the topics in our study of boron nanostructures for the past three years. However, new problems always come along with new discovery, if we insist on not to stop questioning. To name a few, future studies can be extended or expanded as follows:

1. Boron nanoclusters: Study on the thermodynamical properties of these clusters can be done using *first-principles* or *ab initio* molecular dynamics.

2. $2D$ Boron Sheets: Study on the vibrational properties (i.e. IR and Raman spectra) using *first-principles* method.

3. Single-Walled Boron Nanotubes: Study on the vibrational properties (i.e. IR and Raman spectra) using *first-principles* method. Since all the metastable structure will have imginary frequencies, therefore the vibrational study will help us to locate a stable configuration of a nanotube and its corresponding boron sheet.

4. All electron density functional theory approximation for the electron transport calculation in the boron nanostructures

5. Phases stability of boron polymorphms: crystalline bulk and ensembles of nanostructures

## 8.2 Epistemology

First of all, we would like the reader to retain just one idea. This is that the funadamental ideas of *ab initio* or *first-principles* methods is almost as old as quantum mechanics. Although it is not yet an century old knowledge, their impact covers a wide range of scientific disciplines. Nowadays it is more like an espistemology in science, in physics to be more specific. Hence, our study in boron nanostructure is merely a very little, tiny test example of this methodology. Since the methodology itself is always evolving, we can expect that all the underlying understanding (e.g. boron nanostructures) and the physical picture dependent upon it will do the same thing, just like our understanding about atoms. Whenever we know better about it, we will at the same time, encounter more problems. Consequently, the problems can be tougher, more complicated, and grander. Hence, this is how the conventional science evolved, and progress is made.

In this conjunction, it is always to be very interesting for us to ask ourselves what we are doing, and to ask about the fundamental questions about what have we learnt, besides the results and credits of what we obtained. As a matter of fact, if we

look back from the direction which we are always heading, we can always find some new things. For example, several generations of efforts and endeavors have been devoted in solving the Schrödinger equation in electronic structure theories. However, the inverse problem towards these techniques seemed might not be as obvious as it expected to be, although both problems seemed to be reversible. Hence, no matter in "top-down" or "bottom-up" model in the efforts to reconstructing our knowledge, 'dilemma' in this epistemology remains ! Therefore as the sentence quoted in the beginning of this section suggests, building up the reality from the fundamental motif of our understanding might be more complex than analyze things the other way around. Similarly, it also holds in reverse. So as a scientist, it is not totally hopeless, but rather it is a pleasure to continue to find it out. The important thing is not to stop questioning.

# Appendix A

# A Comparison of Total Energy Calculation of Single Boron Atoms

As we mentioned in Chapter 2, there are two main factors: $\hat{H}$ and $\Psi$ affecting the accuracy of total energy calculation of a system within a 'standard model' of electronic structure theory. As shown in the Table I and II below, the total energy for the ground state $\left({}^2P^0_{\frac{1}{2}}\right)$ of a single boron atom $(B)$ will be given based on the J.A. Pople's ansatz in quantum chemistry, compared to the usage of approximate exchange-correlation energy functionals employed in density functional theory (DFT).

**Table 1.1:** The total energy comparison of a single atom within the Hartree-Fock framework. As a reference, all calculations are based on 6-31G(d,p) basis set (except the DF* and RCI**), as we used in the calculation which mentioned in Chapter 3. All the calculations here are based on Gaussian03 program suite, except DF* (i.e. single-configuration using Desclaux's code) and RCI** which obtained under a courtesy by Lin Pan. All the values are in Hartree.

| Total Energy (Hartree) | The Hamiltonian, $\hat{H}$ under *ab initio* method |
|---|---|
| -24.5220371858 | HF |
| -24.5587185906 | MP2 |
| -24.570965520 | MP3 |
| -24.575944275 | MP4 |
| -24.580135297 | CI(SD) |
| -24.5351092531 | DF* |
| -24.6533704240 | RCI** |
| -24.65379151 | Non-relativistic[259] |
| -24.6591448 | Relativistic[259] |

**Table 1.2:** The total energy comparison of a single atom within the Density Functional Theory (DFT) framework. As a reference, all calculations are based on 6-31G(d,p) basis set. All the values are in Hartree. The *Slater* here is with exchange functional $\rho^{\frac{4}{3}}$ with theoretical coefficient of $\frac{2}{3}$, and is also referred to as Local Spin Density exchange[123]. The $X - \alpha$ is with exchange functional $\rho^{\frac{4}{3}}$ with the empirical coefficient of 0.7[123]. In particular, the details of all the approximate exchange-correlation energy functionals: $E_x[\rho]$, $E_{xc}[\rho]$ and $E_{xc-hybrid}[\rho]$, can be obtained at the following. Some of the explicit forms of $LSDA$ and $GGA$ functionals are given in Appendix B, page 479-481 from Ref. 69. The rest can be obtained from the corresponding cited references mentioned in the Gaussian03 manual at page 73-78.

| Total Energy (Hartree) | $\hat{H}$ (DFT) | | |
|---|---|---|---|
| | $E_x[\rho]$ | $E_{xc}[\rho]$ | $E_{xc-hybrid}[\rho]$ |
| -24.0532437512 | Slater | - | - |
| -24.2174900675 | $X - \alpha$ | - | - |
| -24.5145415379 | $Becke - 88$ | - | - |
| -24.4372346060 | - | $SVWN$ (LSDA) | - |
| -24.6296663151 | - | $BPBE$ (GGA) | - |
| -24.6412989906 | - | $BPW91$ (GGA) | - |
| -24.6412762220 | - | $BLYP$ | - |
| -24.6364932777 | - | - | $B3PW91$ |
| -24.6543548367 | - | - | $B3LYP$ |

**Table 1.3:** The total energy comparison of a single atom using B3LYP (i.e. Becke Three Parameter Hybrid Functionals with correlation functional of Lee-Yang-Parr)[123, 175, 176] as the Hamiltonian by varying the basis set using Gaussian program suite.

| Basis Sets | Total Energy (Hartree) ($\hat{H}$ using B3LYP) |
|---|---|
| STO-3G | -24.2815406518 |
| 3-21G | -24.5186296772 |
| 4-31G | -24.6204644595 |
| 6-21G | -24.6485907028 |
| 6-31G | -24.6528150232 |
| 6-31G(d,p) | -24.6543548367 |
| 6-311G(df) | -24.6624412522 |
| 6-331+G(df) | -24.6630075694 |
| 6-311++G(3df,3pd) | -24.6634830812 |

# Appendix B

# Benchmark Calculations

All the calculation results shown here are performed on RAMA (a Linux Beowulf Cluster) with one CPU using Dual Intel Xeon 2.8G, and 2GB RAM in each slave nodes. Since we are using different codes with different basis functions and hamiltonian on diferent chapters in this work, therefore some benchmark calculations as a comparison for different codes are necessary.

## 2.1   Compatibility Among GTOs and Planewaves
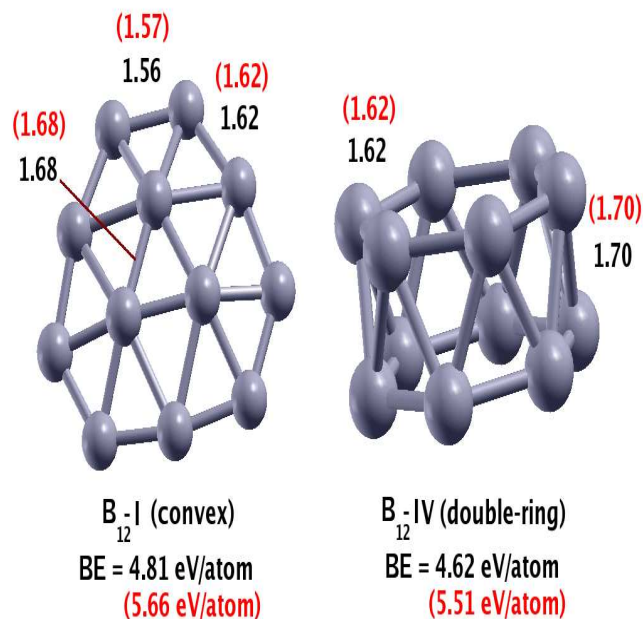
**Figure 2.1:** The comparative study among the Gaussian-type orbitals (i.e. 6-31G(d,p) basis set) with B3LYP exchange-correlation functional (using Gaussian98 program) and ultrasoft-pseudopotential planewave using PW91 exchange-correlation functional (using VASP code) on $B_{12}$ cluster: $B_{12}$-I (2$D$ convex structure) and $B_{12}$-IV (3$D$ double-ring structure). The values in black color is the Gaussian98 result, while the values in red color is the VASP result. All the bond length values are in Å.

## 2.2 Performance of Different *k-point* Mesh: A Case Study

**Table 2.1:** $3D$ $\alpha$-$B_{12}$ crystalline solid: benchmark calculation on the convergence test of total energy Vs. $k$-point mesh in Monkhorst-Pack (MP) grid for the total energy comparison within the Generalized Gradient Approximation (GGA-PW91) within ultrasoft pseudopotential planewave with $E_{cutoff}$ $\sim 260$ eV. For the actual total energy of a system, $E_{tot}$, it is defined as: $E_{tot}$ = $E$ - 846.64370562. All the energy values are in eV.

| Total Energy, $E$ (eV) | MP-grid | CPU time (s) |
|---|---|---|
| -83.071658 | $1 \times 1 \times 1$ | 68.906 |
| -80.354098 | $2 \times 2 \times 2$ | 86.927 |
| -80.404850 | $3 \times 3 \times 3$ | 191.360 |
| -80.345372 | $4 \times 4 \times 4$ | 295.924 |
| -80.351949 | $5 \times 5 \times 5$ | 545.774 |
| -80.353570 | $6 \times 6 \times 6$ | 768.305 |
| -80.353439 | $8 \times 8 \times 8$ | 1607.321 |
| -80.353325 | $10 \times 10 \times 10$ | 3116.994 |
| -80.353320 | $12 \times 12 \times 12$ | 5026.041 |
| -80.353329 | $14 \times 14 \times 14$ | 7698.080 |

**Table 2.2:** Benchmark calculation on the convergence test of total energy Vs. $k$-point mesh in Monkhorst-Pack (MP) grid for the total energy comparison of $2D$ {1221} boron sheet within the Generalized Gradient Approximation (GGA-PW91) within ultrasoft pseudopotential planewave with $E_{cutoff}$ $\sim$ 260 eV. For the actual total energy of a system, $E_{tot}$, it is defined as: $E_{tot}$ = $E$ - 564.43853960. All the energy values are in eV.

| Total Energy, $E$ (eV) | MP-grid | CPU time (s) |
|---|---|---|
| -51.712479 | $1 \times 1 \times 1$ | 140.612 |
| -48.429251 | $2 \times 2 \times 1$ | 130.314 |
| -47.534449 | $3 \times 3 \times 1$ | 301.906 |
| -48.100854 | $4 \times 4 \times 1$ | 295.163 |
| -48.530145 | $6 \times 6 \times 1$ | 525.748 |
| -48.650650 | $8 \times 8 \times 1$ | 835.761 |
| -48.533601 | $10 \times 10 \times 1$ | 1310.896 |
| -48.541092 | $12 \times 12 \times 1$ | 1830.863 |
| -48.569862 | $14 \times 14 \times 1$ | 2396.165 |
| -48.579754 | $16 \times 16 \times 1$ | 2973.431 |

# Appendix C

# The List of The Selected Publications

1. K.C. Lau, M.D. Deshpande and R. Pandey

   *Int. J. Quantum Chem. (Special Issue: Dedicated to the Memory of John A. Pople), 102, 656 (2005)*

2. K.C. Lau, M.D. Deshpande, R. Pati and R. Pandey

   *Int. J. Quantum Chem., 103, 866 (2005)*

3. K.C. Lau and R. Pandey

   *Computing Letters. (Special Issue: Clusters: From a few atoms to nanoparticles), 1, 259-270 (2005).*

4. K.C. Lau, R. Pati, R. Pandey and A.C. Pineda

*Chem. Phys. Lett., 418*, 549 (2006)

5. K.C. Lau, R. Pandey, R. Pati and S.P. Karna

   *Appl. Phys. Lett. 88*, 212111 (2006).

   *(Selected for Virtual Journal of Nanoscale Science & Technology Vol. 13, Issue 23 (2006)).*

6. K.C. Lau and R. Pandey

   *J. Phys. Chem.* **C**, *111*, 2906 (2007).

7. K.C. Lau, R. Orlando and R. Pandey

   *Phys. Rev.* **B**, *(In Review)*.

# References

[1] *http://www.foresight.org/.*

[2] A. Mookerjee and D.D. Sarma (Eds.). *Electronic Structure of Alloys, Surfaces, Advances In Condensed Matter Science Vol. 4.* Taylor and Francis, London, 2003.

[3] U. Landman and W.D. Luedtke. *Faraday Discussions of the Chemical Society, The Royal Society of Chemistry*, 125:1, 2004.

[4] K.C. Lau, M.D. Deshpande, and R. Pandey. *Int. J. Quantum Chem. (Special Issue: Dedicated to the Memory of John A. Pople)*, 102:656, 2005.

[5] K.C. Lau, M.D. Deshpande, R. Pati, and R. Pandey. *Int. J. Quantum Chem.*, 103:866, 2005.

[6] K.C. Lau and R. Pandey. *Computing Letters. (Special Issue: Clusters: From a few atoms to nanoparticles)*, 1:259, 2005.

[7] K.C. Lau, R. Pati, A.C. Pineda, and R. Pandey. *Chem. Phys. Lett.*, 418:549, 2006.

[8] K.C. Lau, R. Pandey, R. Pati, and S.P. Karna. *Appl. Phys. Lett.*, 88:212111, 2006.

[9] K.C. Lau and R. Pandey. *J. Phys. Chem. C.*, 111:2906, 2007.

[10] K.C. Lau, R. Orlando, and R. Pandey. *Phys. Rev. B (In Review)*.

[11] K.C. Lau, R. Orlando, and R. Pandey. *NanoLetters (In Preparation)*.

[12] K.C. Lau, R. Orlando, and R. Pandey. *Phys. Rev. B. (In Preparation)*.

[13] K.C. Lau, R. Pandey, and Y.K. Yap. *(In Preparation)*.

[14] E.L. Muetterties (Ed). *The Chemistry Of Boron and Its Compounds*. John Wiley, New York, 1967.

[15] E.L. Muetterties (Ed). *Boron Hydride Chemistry*. Academic, New York, 1975.

[16] L. Pauling. *Nature of Chemical Bond and the Structure of Molecules and Crystals, 3rd Edition*. Cornell University Press, Itacha, 1960.

[17] A. Quandt and I. Boustani. *ChemPhysChem*, 6:2001, 2005.

[18] W.N. Lipscomb. *Boron Hydrides*. Benjamin, New York, 1963.

[19] W.N. Lipscomb. *J. Less-Common Met.*, 82:1, 1981.

[20] K. Wade. *Chem. Commun.*, 792:100, 1971.

[21] K. Wade. *Asv. Inorg. Chem. Radiochem.*, 18:1, 1976.

[22] E.D. Jemmis, M.M. Balakrishnarajan, and P.D. Pancharatna. *J. Am. Chem. Soc.*, 123:4313, 2001.

[23] E.D. Jemmis, M.M. Balakrishnarajan, and P.D. Pancharatna. *Chem. Rev.*, 102:93, 2002.

[24] E.D. Jemmis and E.G. Jayasree. *Acc. Che. Res.*, 36:816, 2003.

[25] H.W. Kroto, J.R. Heath, S.C.O'brien, R.F. Curl, and R.E. Smalley. *Nature*, 318:162, 1985.

[26] S. Iijima. *Nature*, 354:56, 1991.

[27] K.C. Buschbeck. *Boron Compounds, Elemental Boron and Boron Carbides (Gmelin Handbook of Inorganic Chemistry XIII, Supplement 2).* Springer, Berlin, 1981.

[28] D.W. Bullett. *J. Phys. C: Solid State Phys.*, 15:415, 1982.

[29] C. Mailhiot, J.B. Grant, and A.K. McMahan. *Phys. Rev. B*, 42:9033, 1990.

[30] D. Li, Y. Xu, and W.Y. Ching. *Phys. Rev. B*, 45:5895, 1992.

[31] N. Vast, S. Baroni, G. Zerah, J.M. Besson, A. Polian, J.C. Chervin, and T. Grimsditch. *Phys. Rev. Lett.*, 78:693, 1997.

[32] M. Fujimori, T. Tanaka, T. Nakayama, E. Nishibori, K. Kimura, M. Takata, and M. Sakata. *Phys. Rev. Lett.*, 82:4452, 1999.

[33] J. Zhao and J.P. Lu. *Phys. Rev. B*, 66:092101, 2002.

[34] U. Haussermann, S.I. Simak, R. Ahuja, and B. Johansson. *Phys. Rev. Lett.*, 90:065701, 2003.

[35] A. Masago, K. Shirai, and H. Katayama-Yoshida. *Phys. Rev. B*, 73:104102, 2006.

[36] R.J. Nelmes, J.S. Loveday, D.R. Allan, J.M. Besson, G. Hamel, P. Grima, and S. Hull. *Phys. Rev. B*, 47:7668, 1993.

[37] J.C. Thompson and W.J. McDonald. *Phys. Rev.*, 132:82, 1963.

[38] D.N. Sanz, P. Loubeyre, and M. Mezouar. *Phys. Rev. Lett.*, 89:245501, 2002.

[39] M.I. Eremets, V.V. Struzhkin, H.K. Mao, and R.J. Hemley. *Science*, 293:272, 2001.

[40] T.H. Geballe. *Science*, 293:223, 2001.

[41] D.A. Papaconstantopoulos and M.J. Mehl. *Phys. Rev. B*, 65:172510, 2002.

[42] W. de Heer. *Rev. Mod. Phys.*, 65:611, 1993.

[43] M. Brack. *Rev. Mod. Phys.*, 65:677, 1993.

[44] M. S. Dresselhaus, G. Dresselhaus, and P.C. Ecklund. *Science of Fullerenes and Carbon Nanotubes*. Academic Press, San Diego, 1996.

[45] L. Hanley and S.L. Anderson. *J. Phys. Chem.*, 91:5161, 1987.

[46] L. Hanley, J.L. Whittena, and S.L. Anderson. *J. Phys. Chem.*, 92:5803, 1988.

[47] S.J. La Placa, P.A. Roland, and J.J. Wynne. *Chem. Phys. Lett.*, 190:163, 1992.

[48] P.A. Hintz, M.B. Sowa, S.A. Ruatta, and S.L. Anderson. *J. Chem. Phys.*, 94:6446, 1991.

[49] R. Kawai and J.H. Weare. *J. Chem. Phys.*, 95:1151, 1991.

[50] R. Kawai and J.H. Weare. *Chem. Phys. Lett.*, 191:311, 1992.

[51] M.B. Sowa, A.L. Snolanoff, A. Lapicki, and S.L. Anderson. *J. Chem. Phys.*, 106:9511, 1997.

[52] H.J. Zhai, B. Kiran, J. Li, and L.S. Wang. *Nature Materials*, 2:827, 2003.

[53] B. Kiran, S. Bulusu, H. Zhai, S. Yoo, X.C. Zeng, and L.S. Wang. *PNAS*, 102:961, 2005.

[54] C.J. Otten, O.R. Lourie, M. Yu, J.M. Cowley, M.J. Dyer, R.S. Ruoff, and W.E. Buhro. *J. Am. Chem. Soc.*, 124:4564, 2002.

[55] T.T. Xu, J. Zheng, N. Wu, A.W. Nichollas, J.R. Roth, D.A. Dikin, and R.S. Ruoff. *Nano Lett.*, 4:963, 2004.

[56] D. Ciuparu, R.F. Klie, Y. Zhu, and L. Pfefferle. *J. Phys. Chem. B*, 108:3967, 2004.

[57] I. Boustani. *Phys. Rev. B*, 55:16426, 1997.

[58] H.P. Breuer and F. Petruccione. *The Theory of Open Quantum Systems*. Oxford University Press, New York, 2003.

[59] R. Penrose. *The Road To Reality: A Complete Guide To The Laws of The Universe.* A.A. Knopf, New York, 2005.

[60] J.A. Pople. *Angew. Chem. Int. Ed.*, 38:1894, 1999.

[61] M.C. Payne, M.P. Teter, D.C. Allan, T.A. Arias, and J.D. Joannopoulos. *Reviews Of Modern Physics*, 64:1045, 1992.

[62] R. McWeeny. *Methods of Molecular Quantum Mechanics.* Academic Press, San Diego, 1989.

[63] V. Bonacheckcic-Koutecky and R. Mitric. *Chem. Rev.*, 105:11, 2005.

[64] W.H. Zurek. *Physics Today*, 44:36, 1991.

[65] R.G. Parr and W. Yang. *Density Functional Theory of Atoms and Molecules.* Oxford University Press, New York, 1989.

[66] M. Springborg. *Methods of Electronic-Structure Calculations.* Wiley, England, 2000.

[67] P. Fulde. *Electron Correlations In Molecules and Solids.* Springer-Verlag, Berlin, 1991.

[68] G.F. Giuliani and G. Vignale. *Quantum Theory of the Electron Liquid.* Cambridge University Press, United Kingdom, 2005.

[69] R.M. Martin. *Electronic Structure.* Cambridge University Press, United Kingdom, 2004.

[70] N.F. Mott and R. Pierls. *Proc. Phys. Soc. London, Ser. A*, 49:72, 1937.

[71] N.F. Mott. *Proc. Phys. Soc. London, Ser. A*, 62:416, 1949.

[72] N.F. Mott. *Metal-Insulator Transitions*. Taylor and Francis, London, 1990.

[73] J. Bardeen, L.N. Cooper, and J.R. Schrieffer. *Phys. Rev.*, 106:162, 1957.

[74] E.P. Wigner. *Phys. Rev.*, 46:1002, 1934.

[75] P.W. Anderson. *Basic Notions of Condensed Matter Physics*. Addison-Wesley, Massachusetts, 1977.

[76] D.R. Hartree. *Proc. Cambridge Philos. Soc.*, 24:89, 1928.

[77] V. Fock. *Z. Phys.*, 61:126, 1930.

[78] J.C. Slater. *Phys. Rev.*, 35:210, 1930.

[79] C.C.J. Roothaan. *Rev. Mod. Phys.*, 23:69, 1951.

[80] A. Szabo and N.S. Ostlund. *Modern Quantum Chemistry*. Dover, New York, 1989.

[81] J.K.L. MacDonald. *Phys. Rev.*, 43:830, 1933.

[82] L.H. Thomas. *Proc. Camb. Phil. Soc.*, 23:542, 1927.

[83] E. Fermi. *Rend. Accad.*, 6:602, 1927.

[84] E. Fermi. *Z. Phys.*, 48:73, 1928.

[85] P.A.M. Dirac. *Proc. Camb. Phil. Soc.*, 26:376, 1930.

[86] E.H. Lieb. *Rev. Mod. Phys.*, 53:603, 1981.

[87] D.A. McQuarrie. *Statistical Mechanics*. Harper and Row, New York, 1976.

[88] P.K. Archarya. *J. Chem. Phys.*, 78:2101, 1983.

[89] C.F. von Weizsacker. *Zur theorie dier kernmassen, Z. Physik*, 96:431, 1935.

[90] E. Teller. *Rev. Mod. Phys.*, 34:627, 1962.

[91] P. Hohenberg and W. Kohn. *Phys. Rev.*, 136, 1964.

[92] W. Kohn and L.J. Sham. *Phys. Rev.*, 140, 1965.

[93] M. Levy. *Proc. Natl. Acad. Sci.*, 76:6062, 1979.

[94] M. Levy. *Phys. Rev. A*, 26:1200, 1982.

[95] A. Shimony and H. Feshbach (Ed.). *Physics as Natural Philosophy*. Plenum, New York, 1982.

[96] E. Lieb. *Int. J. Quant. Chem.*, 24:243, 1983.

[97] C. Fiolhais, F. Nogueira, and M. Marques (Eds.). *A Primer In Density Functional Theory*. Springer-Verlag, Berlin, 2003.

[98] T.L. Beck. *Rev. Mod. Phys*, 72:1041, 2000.

[99] W. Heitler and F. London. *Z. Phys.*, 44:455, 1927.

[100] L. Pauling and E.B. Wilson. *Introduction To Quantum Mechanics*. McGraw-Hill Book Company Inc., New York, 1935.

[101] F. Hund. *Z. Phys.*, 51:759, 1928.

[102] R.S. Mulliken. *Phys. Rev.*, 32:186, 1928.

[103] J.C. Slater. *Phys. Rev.*, 36:57, 1930.

[104] E. Huckel. *Z. Phys.*, 70:204, 1931.

[105] E. Huckel. *Z. Phys.*, 72:310, 1931.

[106] E. Huckel. *Z. Phys.*, 76:628, 1932.

[107] W. Koch and M.C. Holthausen. *A Chemist's Guide to Density Functional Theory*. Wiley-VCH Verlag, Weinheim, 2001.

[108] S.F. Boys. *Proc. R. Soc. London A*, 200:542, 1950.

[109] B.I. Dunlap. *Phys. Rev. A*, 66:032502, 2002.

[110] W.J. Hehre, R.F. Stewart, and J.A. Pople. *J. Chem. Phys.*, 51:2657, 1969.

[111] W.J. Hehre J.S. Binkley, J.A. Pople. *J. Amer. Chem. Soc.*, 102:939, 1980.

[112] M.S. Gordon, J.S. Binkley, J.A. Pople, W.J. Pietro, and W.J. Hehre. *J. Amer. Chem. Soc.*, 104:2797, 1982.

[113] W.J. Pietro, M.M. Francl, W.J. Hehre, D.J. Defrees, J.A. Pople, and J.S. Binkley. *J. Amer. Chem. Soc.*, 104:5039, 1982.

[114] K.D. Dobbs and W.J. Hehre. *J. Comp. Chem.*, 7:359, 1986.

[115] K.D. Dobbs and W.J. Hehre. *J. Comp. Chem.*, 8:861, 1987.

[116] K.D. Dobbs and W.J. Hehre. *J. Comp. Chem.*, 8:880, 1987.

[117] R. Ditchfield, W.J. Hehre, and J.A. Pople. *J. Chem. Phys.*, 54:724, 1971.

[118] W.J. Hehre, R. Ditchfield, and J.A. Pople. *J. Chem. Phys.*, 56:2257, 1972.

[119] P.C. Hariharan and J.A. Pople. *J.A. Mol. Phys.*, 27:209, 1974.

[120] M.S. Gordon. *Chem. Phys. Lett.*, 76:163, 1980.

[121] P.C. Hariharan and J.A. Pople. *Theo. Chem. Acta.*, 28:213, 1973.

[122] L.A. Curtiss R.C.B. Jr. *J. Comp. Chem.*, 11:1206, 1990.

[123] M. Gaussian 98. Frisch, G.W. Trucks, H.B. Schlegel, G.E. Scuseria, M.A. Robb, J.R. Cheeseman, V.G. Zakrzewski, J.A. Montgomery, R.E. Stratmann, J.C. Burant, S. Dapprich, J.M. Millam, A.D. Daniels, K.N. Kudin, M.C. Strain, O. Farkas, J. Tomasi, V. Barone, M. Cossi, R. Cammi, B. Mennucci, C. Pomelli, C. Adamo, J. Clifford, S.and Ochterski, G.A. Petersson, P.Y. Ayala, Q. Cui, K. Morokuma, D.K. Malick, A.D. Rabuck, K. Raghavachari, J.B. Foresman, J. Cioslowski, J.V. Ortiz, B.B. Stefanov, G. Liu, A. Liashenko, P. Piskorz, I. Komaromi, R. Gomperts, R.L. Martin, D.J. Fox, T. Keith, M.A. Al-Laham, C.Y. Peng, A. Nanayakkara, C. Gonzalez, M. Challacombe, P. M.W. Gill, B.G. Johnson, W. Chen, M.W. Wong, J.L. Andres, M. Head-Gordon, E.S. Replogle, and J.A. Pople. *Gaussian, Inc., Pittsburgh PA*.

[124] J.C. Slater. *The Calculation of Molecular Orbitals*. Wiley, New York, 1979.

[125] D.A. Papaconstantopoulos and M.J. Mehl. *J. Phys. Condens. Matter*, 15, 2003.

[126] D.R. Hamann. *Phys. Rev. Lett.*, 42:662, 1979.

[127] D.R. Hamann, M. Schluter, and C. Chiang. *Phys. Rev. Lett.*, 43:1494, 1979.

[128] J. Korringa. *Physica*, 13:392, 1947.

[129] W. Kohn and N. Rostoker. *Phys. Rev.*, 94:1111, 1954.

[130] C. Herring. *Phys. Rev.*, 57:1169, 1940.

[131] J.C. Slater. *Phys. Rev.*, 92:603, 1953.

[132] M.M. Saffren and J.C. Slater. *Phys. Rev.*, 92:1126, 1953.

[133] O.K. Andersen. *Phys. Rev. B*, 12:3060, 1975.

[134] C. Pisani and R. Dovesi. *Int. J. Quantum Chem.*, 17:501, 1980.

[135] C. Pisani (Ed.). *Quantum mechanical Ab Initio Calculation of the Properties of Crystalline Materials.* Springer-Verlag, Berlin, 1996.

[136] C. Pisani, R. Dovesi, and C. Roetti. *Hartree-Fock Ab Initio Treatment of Crystalline Systems.* Springer-Verlag, Berlin, 1988.

[137] H. Monkhorst and J. Pack. *Phys. Rev.*, 13:5188, 1976.

[138] N.W. Ashcroft and N.D. Mermin. *Solid State Physics.* Holt Saunders, Philadelphia, 1976.

[139] D.J. Chadi and M.L. Cohen. *Phys. Rev. B*, 8:5747, 1973.

[140] J.D. Joannopoulos and M.L. Cohen. *J. Phys. C*, 6:1572, 1973.

[141] V.P. Smirnov R.A. Evarestov. *Phys. Status Solidi*, 119:9, 1983.

[142] J.C. Philips. *Phys. Rev.*, 112:3, 1958.

[143] M.L. Cohen and V. Heine. *Sold State Phys.*, 24:37, 1970.

[144] J.D. Joannopoulos, Th. Starkloff, and M. Kastner. *Phys. Rev. Lett.*, 38:12, 1977.

[145] A. Redondo, W.A. Goddard, and T.C. McGill. *Phys. Rev. B*, 15:5038, 1977.

[146] Th. Starkloff and J.D. Joannopoulos. *Phys. Rev. B*, 16:5212, 1977.

[147] A. Zunger and M.L. Cohen. *Phys. Rev. B*, 20:4082, 1979.

[148] G.P. Kerker. *J. Phys. C*, 13:189, 1980.

[149] G.B. Bachelet D.R. Hamann M. Schluter. *Phys. Rev. B*, 26:4199, 1982.

[150] M.T. Yin and M.L. Cohen. *Phys. Rev. B*, 25:7403, 1982.

[151] D.R. Hamann. *Phys. Rev. B*, 40:2980, 1989.

[152] E.L. Shirley, D.C. Allan, R.M. Martin, and J.D. Joannopoulos. *Phys. Rev. B*, 40:3652, 1989.

[153] D. Vanderbilt. *Phys. Rev. B*, 41:7892, 1990.

[154] N. Troullier and J.L. Martins. *Phys. Rev. B*, 43:1993, 1991.

[155] G. Kresse and J. Hafner. *Phys. Rev. B*, 47:558, 1993.

[156] G. Kresse and J. Furthmuller. *Phys. Rev. B*, 54:11169, 1996.

[157] http://cms.mpi.univie.ac.at/vasp/.

[158] P.E. Blochl. *Phys. Rev. B*, 50:17953, 1994.

[159] H. Haberland (Ed.). *Clusters of Atoms and Molecules I*. Springer-Verlag, Berlin, 1994.

[160] I. Boustani. *Int. J. Quantum Chem.*, 52:1081, 1994.

[161] I. Boustani. *Chem. Phys. Lett.*, 240:135, 1995.

[162] A. Ricca and C.W. Bauschlicher. *Chem. Phys.*, 208:233, 1996.

[163] F.L. Gu, X. Yang, A.C. Tang, H. Jiao, and P.V.R. Schleyer. *J. Comput. Chem.*, 19:203, 1998.

[164] H.J. Zhai, L.S. Wang, A.N. Alexandrova, A.I. Boldyrev, and V.G. Zakrzewski. *J. Phys. Chem. A*, 107:9313, 2003.

[165] H.J. Zhai, L.S. Wang, A.N. Alexandrova, and A.I. Boldyrev. *J. Chem. Phys.*, 117:7917, 2002.

[166] A.N. Alexandrova, A.I. Boldyrev, H.J. Zhai, L.S. Wang, E. Steiner, and P.W. Fowler. *J. Phys. Chem. A*, 107:1359, 2003.

[167] A.N. Alexandrova, A.I. Boldyrev, H.J. Zhai, and L.S. Wang. *J. Phys. Chem. A*, 108:3509, 2004.

[168] H.J. Zhai, A.N. Alexandrova, K.A. Birch, A.I. Boldyrev, and L.S.Wang. *Angew. Chem. Int. Ed.*, 42:6004, 2003.

[169] R.O. Jones and G. Seifert. *Phys. Rev. Lett.*, 79:443, 1997.

[170] R.O. Jones. *J. Chem. Phys.*, 110:5189, 1999.

[171] H. Prinzbach, A. Weiler, P. Landenberger, F. Wahl, J. Worth, L.T. Scott, M. Gelmont, D. Olevano, and B. Issendorff. *Nature*, 407:60, 2000.

[172] J.E. Fowler and J.M. Ugalde. *J. Phys. Chem. A*, 104:397, 2000.

[173] J. Aihara. *J. Phys. Chem. A*, 105:5486, 2001.

[174] A. Costales, A. Kandalam, and R. Pandey. *J. Phys. Chem. A*, 107:4508, 2003.

[175] A.D. Becke. *J. Chem. Phys.*, 98:5648, 1993.

[176] C. Lee, W. Yang, and R.G. Parr. *Phys. Rev. B*, 37:789, 1988.

[177] H. Reis and M.G. Papadopoulos. *J. Comp. Chem*, 20:679, 1999.

[178] H. Reis, M.G. Papadopoulos, and I. Boustani. *Int. J. Quantum Chem.*, 78:131, 2000.

[179] A. Abdurahman, A. Shukla, and G. Seifert. *Phys. Rev. B*, 66:155423, 2002.

[180] J. Ma, Z. Li, K. Fan, and M. Zhou. *Chem. Phys. Lett.*, 372:708, 2003.

[181] W.N. Lipscomb. *Acc. Chem. Rec.*, 6:257, 1973.

[182] R.B. King. *Chem. Rev.*, 101:1119, 2001.

[183] M.A.L. Marques and S. Botti. *J. Chem. Phys.*, 123:014310, 2005.

[184] S. Chacko, D.G. Kanhere, and I. Boustani. *Phys. Rev. B*, 68:035414, 2003.

[185] I. Boustani, A. Rubio, and J.A. Alonso. *Chem. Phys. Lett.*, 311:21, 1999.

[186] I. Boustani, A. Quandt, and A. Rubio. *J. of Solid State Chem.*, 154:269, 2000.

[187] J.C. Grossman, M.E. Colvin, N.L. Tran, S.G. Louie, and M.L. Cohen. *Chem. Phys. Lett.*, 356:247, 2002.

[188] L.S. Wang and H. Wu. *Z. Phys. Chem. (Munich)*, 203:45, 1998.

[189] D.R. Lide. *CRC Handbook of Chemistry and Physics*. CRC Press, Boca Raton, 1995.

[190] J.C. Rienstra-Kiracofe, G.S. Tschumper, and H.F. III Schaefer. *Chem. Rev.*, 102:231, 2002.

[191] R.G. Pearson. *Chemical Hardness*. Wiley-VCH Verlag, Germany, 1997.

[192] J.E. Carpenter and F.J. Weinhold. *J. Mol. Struc. (Theochem)*, 169:41, 1988.

[193] Jr. E. Bright Wilson, J.C. Decius, and P.C. Cross. *Molecular Vibrations*. Dover, New York, 1955.

[194] D. Ciuparu, Y. Chen, S. Lim, G.L. Haller, and L.J. Pfefferle. *J. Phys. Chem. B*, 108:503, 2004.

[195] L. Wirtz and A. Rubio. *IEEE Transactions On Nanotechnology*, 2:341, 2003.

[196] R. Saito, G. Dresselhaus, and M.S. Dresselhaus. *Physical Properties of Carbon Nanotubes*. Imperial College Press, London, 2003.

[197] M.H. Evans, J.D. Joannopoulos, and S.T. Pantelides. *Phys. Rev. B*, 72:045434, 2005.

[198] I. Cabria, M.J. Lopez, and J.A. Alonso. *Nanotechnology*, 17:778, 2006.

[199] J. Kunstmann and A. Quandt. *Phys. Rev. B*, 74:035413, 2006.

[200] J.P. Perdew and Y. Wang. *Phys. Rev. B*, 45:13244, 1992.

[201] M. Methfessel and A.T. Paxton. *Phys. Rev. B*, 40:3616, 1989.

[202] C. Kittel. *Introduction to Solid State Physics, 7-th Edition*. Wiley, New York, 1996.

[203] J. Donohue. *The Structure of The Elements*. Wiley, New York, 1974.

[204] J. Aihara, H. Kanno, and T. Ishida. *J. Am. Chem. Soc.*, 127:13324, 2005.

[205] H.S. Nalwa (Ed.). *Encyclopedia of Nanoscience and Nanotechnology*. American Scientific Publishers, California, USA, 2004.

[206] A. Gindulytu, W.N. Lipscomb, and L. Massa. *Inorg. Chem.*, 37:6544, 1998.

[207] V.R. Saunders, R. Dovesi, C. Roetti, R. Orlando, C.M. Zicovich-Wilson, N.M. Harrison, K. Doll, B. Civalleri, I.J. Bush, P. D'Arco, and M. Llunell. *CRYSTAL03 User's Manual, Universita di Torino, Torino, 2003*.

[208] S. Lee, D.M. Bylander, and L. Kleinman. *Phys. Rev. B*, 42:131, 1990.

[209] F.H. Horn. *J. Appl. Phys.*, 30:1611, 1959.

[210] J. Tersoff and R.S. Ruoff. *Phys. Rev. Lett.*, 73:676, 1994.

[211] J.P. Salvetat, G.A.D. Briggs, J.M. Bonard, R.R. Bacsa, A.J. Kulik, T. Stockli, N.A. Burnham, and L. Forro. *Phys. Rev. Lett.*, 82:944, 1999.

[212] M.S. Dresselhaus, G. Dresselhaus, and P. Avouris (Eds.). *Carbon Nanotubes: Synthesis, Structure, Properties, and Applications.* Springer, Berlin, 2001.

[213] J. Bai, X.C. Zeng, H. Tanaka, and J.Y. Zeng. *PNAS*, 101:2664, 2004.

[214] B. Yan, G. Zhou, W. Duan J. Wu, and B. Gu. *Phys. Rev. B*, 73:155432, 2006.

[215] D.F. Perepichka and F. Rosei. *Small*, 2:22, 2006.

[216] S.B. Fagan, R.J. Baierle, R. Mota, A.J.R. da Silva, and A. Fazzio. *Phys. Rev. B*, 61:9994, 2000.

[217] A.S. Barnard and S.P. Russo. *J. Phys. Chem. B*, 107:7577, 2003.

[218] S. Datta. *Electronic Transport in Mesoscopic Systems.* Cambridge University Press, UK, 2003.

[219] M. H. Sadd. *Elasticity: Theory, Applications, and Numerics, 1-st Ed.* Elsevier Butterworth-Heinemann, 2005.

[220] E. Hernandez, C. Goze, P. Bernier, and A. Rubio. *Phys. Rev. Lett.*, 80:4052, 1998.

[221] J.P. Lu. *Phys. Rev. Lett.*, 79:1297, 1997.

[222] D. Sanchez-Portal, E. Artacho, J.M. Soler, A. Rubio, and P. Ordejon. *Phys. Rev. B*, 59:12678, 1999.

[223] M.F. Yu, B.S. Files, S. Arepalli, and R.S. Ruoff. *Phys. Rev. Lett.*, 84:5552, 2000.

[224] U.D. Venkateswaran, A.M. Rao, E. Richter, M. Menon, A. Rinzler, R.E. Smalley, and P.C. Eklund.

[225] S. Reich, C. Thomsen, and P. Ordejon. *Phys. Rev. B*, 65:153407, 2002.

[226] J.P. Lu. *J. Phys. Chem. Solids*, 58:1649, 1997.

[227] C. Thomsen, S. Reich, H. Jantoljak, I. Loa, K. Syassen, M. Burghard, G.S. Duesberg, and S. Roth. *Appl. Phys. A*, 69:309, 1999.

[228] M.A. Blanco, E. Francisco, and V. Luana. *Comput. Phys. Commun.*, 158:57, 2004.

[229] P. Vinet, J.H. Rose, J. Ferrante, and J.R. Smith. *J. Phys.: Condens. Matter*, 1:1941, 1989.

[230] J. Tang, L. Qin, T. Sasaki, M. Yudasaka, A. Matsushita, and S. Iijima. *Phys. Rev. Lett.*, 85:1887, 2000.

[231] J.P. Poirier. *Introduction to the Physics of the Earth's Interior*. Cambridge University Press, UK, 1991.

[232] F. Seitz and D. Turnbull (Eds.). *Solid State Physics Vol. 16*. Academic Press, New York, 1964.

[233] T. Tohei, A. Kuwabara, F. Oba, and I. Tanaka. *Phys. Rev. B*, 73:064304, 2006.

[234] Y. Xu, H. Peng, R.H. Hauge, and R.E. Smalley. *Nano Lett.*, 5:163, 2005.

[235] K. Hirose, T. Ono, Y. Fujimoto, and S. Tsukamoto. *First-Principles In Real-Space Formalism*. Imperial College Press, London, 2005.

[236] D.K. Ferry and S.M. Goodnick. *Transport In Nanostructures*. Cambridge University Press, London, 2001.

[237] M.A. Reed and T. Lee. *Molecular Nanoelectronics*. American Scientific Publishers, California, USA, 2003.

[238] R. Landauer. *IBM J. Res. Dev.*, 1:223, 1957.

[239] R. Landauer. *J. Phys.: Condens. Matter.*, 1:8099, 1989.

[240] R. Kubo. *J. Phys. Soc. Jpn*, 12:570, 1957.

[241] M. Buttiker. *Phys. Rev. Lett.*, 57:1761, 1985.

[242] D.S. Fisher and P.A. Lee. *Phys. Rev. B*, 23:6851, 1981.

[243] M. Paulsson. *arXiv:cond-mat/0210519 v2*.

[244] D.A. Papaconstantopoulos. *Handbook of Electronic Structure of Elemental Solids*. Plenum, New York, 1986.

[245] R.Pati, Y. Zhang, S. K. Nayak, and P. M. Ajayan. *Appl. Phys. Lett.*, 81:2638, 2002.

[246] W. Tian, S. Datta, S. Hong, R. Reifenberger, J.I. Henderson, and C.P. Kubiak. *J. Chem. Phys.*, 109:2874, 1998.

[247] S. J. Tans, M. H. Devoret, H. Dai, A. Thess, R. E. Smalley, L. J. Geerligs, and C. Dekker. *Nature*, 386:474, 1997.

[248] A. Bachtold, M. S. Fuhrer, S. Plyasunov, M. Forero, E. H. Anderson, A. Zettl, and P. L. McEuen. *Phys. Rev. Lett*, 84:6082, 2000.

[249] V. Krstic, S. Roth, and M. Burghard. *Phys. Rev. B*, 62, 2000.

[250] W. Liang, M. Bockrath, D. Bozovic, J. Hafner, M. Tinkham, and H. Park. *Nature*, 411:665, 2001.

[251] J. Kong, E. Yenilmez, T. W. Tombler, W. Kim, H. Dai, R. B. Laughlin, L. Liu, C. S. Jayanthi, and S. Y. Wu. *Phys. Rev. Lett.*, 87:106801, 2001.

[252] C. T. White and T. N. Todorov. *Nature*, 393:240, 1998.

[253] M.P. Anantram and T.R. Govindan. *Phys. Rev. B*, 58:4882, 1998.

[254] A. R. Rocha, V. Garcia-Suarez, S.W. Bailey, C.J. Lambert, J. Ferrer, and S. Sanvito. *Nature Materials*, 4:335, 2005.

[255] P.W. Anderson. *Science*, 177:393, 1972.

[256] M. Baer. *Beyond Born-Oppenheimer: Electronic Nonadiabatic Coupling Terms and Conical Intersections*. John Wiley, New York, 2005.

[257] L. Hedin. *Phys. Rev.*, 139, 1965.

[258] H. Ehrenreich, F. Seitz, and D. Turnbull (Eds.). *Solid State Physics Vol. 23*. Academic Press, New York, 1969.

[259] C.W. Scherr, J.N. Silverman, and F.A. Matsen. *Phys. Rev.*, 12:830, 1962.